Rydberg-Atom Interferometry

James E. Palmer

A thesis presented for the degree of
Doctor of Philosophy

Department of Physics and Astronomy
University College London

05.03.2020

Declaration

I, James E. Palmer confirm that the work presented in this thesis is my own. Where information has been derived from other sources, I confirm that this has been indicated in the thesis.

Signed:

Date:

I leave Sisyphus at the foot of the mountain. One always finds one's burden again. But Sisyphus teaches the higher fidelity that negates the gods and raises rocks. He too concludes that all is well. This universe henceforth without a master seems to him neither sterile nor futile. Each atom of that stone, each mineral flake of that night-filled mountain, in itself, forms a world. The struggle itself toward the heights is enough to fill a man's heart. One must imagine Sisyphus happy.

—Albert Camus, *The Myth of Sisyphus*

Abstract

Matter-wave interferometry has many possible uses, ranging from tests of fundamental physics to applications in sensing. In order to achieve this interferometry, quantum superpositions of spatially-separated components need to be generated. There are several possible methods to accomplish this using Rydberg atoms; this thesis presents the experimental investigation of two of these. Both of these methods use inhomogeneous electric fields to spatially split beams of Rydberg atoms.

In the first method, field distributions were generated above two-dimensional electrode structures and used to transversely split beams of helium Rydberg atoms into pairs of components spatially separated by up to 15.6 mm. Effects of amplitude modulation of the electric fields of this beam splitter were shown to cause particle losses through transitions into unconfined Rydberg-Stark states. This led to further studies of the depolarisation of Rydberg-Stark states in radio-frequency electric fields. Through this work it is shown that both 'resonant' and 'non-resonant' broadband modulation with amplitudes on the order of 10 $\mathrm{mV{\cdot}cm^{-1}}$ are sufficient to cause significant depolarisation of initially prepared quantum states on a timescale of 5 μs in a static offset electric field of 0.43 $\mathrm{V{\cdot}cm^{-1}}$.

In a second class of experiments, matter-wave interferometry has been performed with helium atoms in high Rydberg states. In this work a series of microwave and electric field gradient pulses were used to create a spatial separation between two components of a coherent superposition of states, while ensuring that

the momenta of these components were equal at the end of the process to enable matter-wave interference to be observed. For the Rydberg states used, the spatial extent of the Rydberg electron wavefunction was ~ 320 nm and displacements of up to 150 pm were observed between the pairs of matter-wave components at the end of the interferometry sequences.

Impact statement

In this thesis the experimental demonstration of a chip-based beam splitter, a study of radio-frequency depolarisation and a scheme for matter-wave interferometry with atoms in highly excited Rydberg states are presented. The beam splitter was designed to integrate with the type of architectures used in hybrid cavity quantum electrodynamics experiments and can be used to distribute samples of atoms to spatially-separated interaction regions. In addition, it is foreseen to exploit it in collision studies including atoms and molecules in high Rydberg states to allow reference intensity measurements. It is also a valuable addition to the set of tools available for Rydberg-atom optics experiments.

The results of the studies of radio-frequency depolarisation of Rydberg-Stark states are of importance not only in the operation of Rydberg-atom beam splitters, but Rydberg-Stark deceleration and trapping experiments in general. State changing and particle losses that arise from these depolarisation processes are generally undesirable in all experiments with electrostatically trapped Rydberg atoms and molecules. As such, the results presented are of interest in the development of hybrid approaches to quantum optics and quantum information processing with cold trapped Rydberg atoms; studies of ion-molecule reactions at low temperatures with Rydberg molecules; and precision tests of fundamental physics with positronium atoms.

Because of the short de Broglie wavelengths of massive particles, e.g., electrons,

atoms and molecules, matter-wave interferometry involving these samples is ideally suited for applications in quantum sensing. The Rydberg-atom interferometry scheme presented in this thesis is of particular relevance in situations where light-pulse interferometry cannot be applied. With an appropriate selection of states, this scheme could be developed to create new types of electrometers and gravimeters.

Acknowledgements

I first thank my supervisor, Professor Stephen Hogan, for giving me the opportunity to undertake the PhD studies described in this thesis. Throughout this work, his support has been forthcoming, enthusiastic and invaluable. The experimental skills and attitudes towards scientific research that he has imparted to me during my studies will constitute the cornerstone of all my further endeavours. His impact upon my academic career has been monumental and cannot be overstated. I would also like to thank the various members of the research group, who over the years have created an enjoyable and stimulating environment in which to work.

I take the opportunity here to express my gratitude to Tali and Ryan for their constant friendship and for providing respite in the times when it was most needed in these past four years.

Finally, I must thank my parents for their support in every conceivable aspect, without which this undertaking may have proved to be insurmountable, and my brother, Edward, for provoking me over the course of innumerate phone calls to consider my work from a wider perspective, and to situate it in the context of a larger body of knowledge, but primarily for being an unwavering friend.

Contents

Chapter 1

Rydberg states and their applications

A Rydberg state of an atom or molecule is one in which an electron has been excited to an orbital with a very high principal quantum number, n. For each quantum state of an ion core there is an associated infinite series of Rydberg states which converge on the corresponding ionisation limit. For hydrogenic systems the energy levels in this series are given by the Rydberg formula [1]

$$E_{n\ell} = E_{\text{ion}} - \frac{hcR_M}{(n-\delta_\ell)^2}, \tag{1.1}$$

where E_{ion} is the ground state ionisation energy, R_M is the Rydberg constant corrected for the reduced mass of the atom or molecule, h is the Planck constant, c is the speed of light in vacuum and δ_ℓ is a quantum defect, where ℓ is the electron orbital angular momentum quantum number. Figure 1.1 shows these Rydberg energy levels for typical atoms and molecules.

Atoms and molecules in Rydberg states can possess extreme properties. Firstly, the classical orbits of the Rydberg electrons can be very large as their radius is proportional to n^2, e.g., the classical orbit radius for an electron in an orbital with

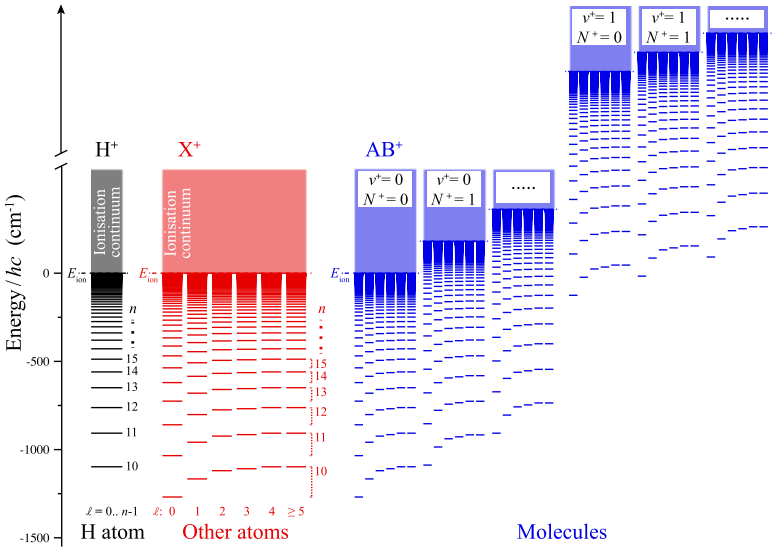

Figure 1.1: Rydberg series in hydrogen, other atoms and molecules. From Reference [2].

$n = 50$ is $n^2 a_0 \simeq 130$ nm, where a_0 is the Bohr radius. This leads to large static electric dipole moments, e.g., the maximum induced electric dipole moment for $n = 50$ is approximately $(3/2)n^2 e a_0 \simeq 9531$ D, where e is the electron charge. Secondly, they can be long lived with fluorescence lifetimes proportional to n^3, e.g., the lifetime of the 1s50p ^{3}P levels in helium (He) are $\simeq 150$ μs while the lifetime of the $|50c\rangle$ circular state (the state for which, for any value of n, the values of ℓ and m_ℓ, the azimuthal quantum number, are maximal, i.e., $|nc\rangle = |n, \ell = n-1, m_\ell = n-1\rangle$) in He is 28.6 ms [2]. These properties make atoms in high Rydberg states well suited for applications in experiments in many different areas of physics and in many of these the preparation and manipulation of superpositions of Rydberg states has proved to be extremely fruitful.

1.1 Quantum information processing

The large electric dipole moments associated with atoms in Rydberg states allow them to strongly interact with other atoms via two mechanisms. The first mechanism arises from the van der Waals interaction and leads to what is known as the Rydberg blockade. When an atom is excited to a Rydberg state the diffuse electron charge distribution associated with the Rydberg electron wavefunction can be polarised easily as a result of the presence of another nearby atom. This polarisation causes the energy levels to shift. If this shift is greater than $\hbar\Omega$, where Ω is the Rabi frequency associated with the ground-state to Rydberg-state transition, a second atom cannot be excited by the same pulse that excited the first. This effect was first observed in large clouds of atoms. It was then later demonstrated for a pair of single atoms in two experiments in 2009. In one of these Urban et al. [3] showed that the excitation of one rubidium atom to a Rydberg state with $n = 79$ suppressed the excitation of a second atom located 10 μm away by over 80%. In the second experiment by Gaetan et al. [4] an enhancement in the single atom excitation rate was observed when two atoms (separated by 3.6 μm) were probed demonstrating the preparation of an entangled state of the two atoms. The collective increase in the observed Rabi frequency in these experiments can be seen in Figure 1.2.

The second interaction mechanism between atoms in Rydberg states is the resonant electric dipole-dipole interaction which allows for entanglement and manipulation of pairs or ensembles of Rydberg atoms over much larger distances. Together, this and the shorter range van der Waals interaction make Rydberg atoms an attractive choice for quantum simulation [5] and in the implementation of quantum gates for information processing.

Aside from their strong interactions with other atoms and molecules, Rydberg atoms can also interact with and couple strongly to electromagnetic fields. This has caused Rydberg atoms to become invaluable tools in the investigation and ex-

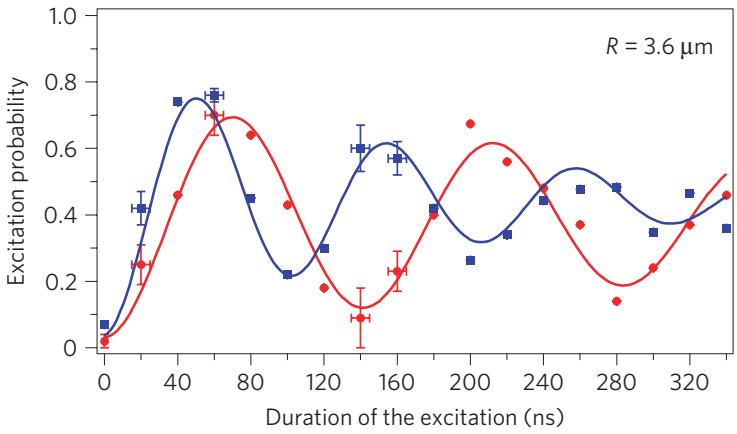

Figure 1.2: Collective excitation of two single atoms. The red circles show the probability of finding an atom in an excited Rydberg state as a function of excitation pulse length if there are no other atoms located nearby. The blue squares show the probability of finding one atom in the excited Rydberg state when two ground state atoms are initially present. The observed enhancement of the excitation rate corresponds to the entanglement of the atoms. From Reference [4].

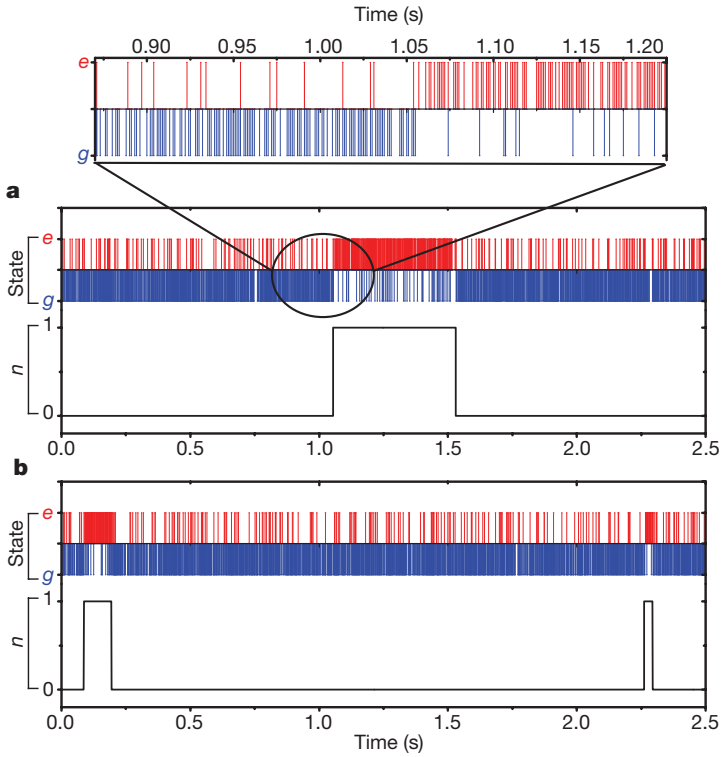

Figure 1.3: "Birth, life and death of a photon". (a) A time sequence of quantum non-demolition measurements of an initially empty cavity, indicated by the repeated detection of atoms in the Rydberg state $|g\rangle$, into which a photon enters after ~1 s. This is indicated by the detection of atoms in state $|e\rangle$. (b) Observation of two successive photons in the cavity. From Reference [6].

ploitation of the interaction between matter and light, particularly in the microwave region of the electromagnetic spectrum.

In work for which Serge Haroche (along with David Wineland) would later be awarded a Nobel prize, Rydberg atoms were employed to allow non-destructive observation of “the birth, life and death of a photon" in a cavity. In this experiment [6] a high quality factor microwave cavity was tuned to be near resonant with the transition between two circular Rydberg states of rubidium, i.e., states with

principal quantum numbers $n = 50$ and $n = 51$ labelled g and e, respectively, and probed using a Ramsey interferometry scheme. At a rate of 900 Hz, a series of single rubidium atoms were each prepared in a superposition of e and g using a combination of laser and microwave fields and travelled through the cavity before being interrogated by another microwave field and, subsequently, their final state measured. As the atoms travelled through the cavity the superposition state accumulated a phase shift that was dependent on the number of photons present and the detuning of the cavity. The detuning, and hence the phase shift, were adjusted such that the atoms were found in g when probed if no photons were present in the cavity, and e if a photon was present. This technique allowed a single photon to be measured multiple times since its state was not changed by the atoms passing through the cavity. Figure 1.3 shows the results of this experiment demonstrating the observation of the entire lifetimes of single photons in the cavity.

For Rydberg states with $n \gtrsim 20$, the transitions for which $\Delta n = \pm 1$ fall in the range of millimetre and microwave radiation; this, along with their strong dipole-dipole interactions that allow for the production of entangled states and their long lifetimes, makes Rydberg atoms excellent candidates for hybrid approaches to quantum information processing. In one such approach, atoms in Rydberg states would be coupled to solid-state qubits via microwave resonators [7].

With such applications in hybrid quantum information processing in mind, Hogan et al. [8] demonstrated coherent coupling of ensembles of He atoms in Rydberg states to microwave fields propagating in coplanar microwave waveguides. The atoms in these experiments were initially excited to np Rydberg states with $n = 31 - 35$ and travelled over the waveguide within 1 mm of the surface. Microwave pulses were then applied to the waveguide with frequencies appropriate to drive $n\text{p} \rightarrow n\text{s}$ transitions for a range of powers and pulse durations before state-selective electric-field ionisation allowed the final states of the atoms to be de-

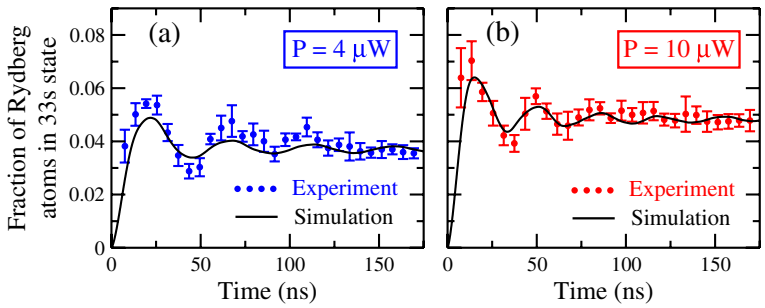

Figure 1.4: Rabi oscillations in the population of the 33*s* state demonstrating coupling between Rydberg atoms and the microwave field propagating in a coplanar waveguide for source powers of (a) 4 μW and, (b) 10 μW . From Reference [8].

termined. The corresponding results of these measurements for states with $n = 33$ can be seen in Figure 1.4. In this figure Rabi oscillations in the 33s state population are observed as the atoms couple to, and are driven by, the microwave field at two different powers.

It is with the aim of integrating Rydberg atoms with quantum electrodynamics (QED) architectures based on microwave circuits of this type that many of the techniques and devices described in Chapter 2 for manipulating the motion of atoms and molecules in Rydberg states, along with the beam splitter presented in Chapter 4, have been developed.

1.2 Quantum sensing

The extreme sensitivity of Rydberg state to static electric and magnetic fields and electromagnetic radiation at microwave/millimetre wave frequencies make them natural candidates when designing experiments and devising experimental schemes to measure these fields. Many such experiments have been performed utilising Rydberg states in different ways. One early example of this is the work carried out by Osterwalder and Merkt [9] that employed krypton atoms in high

Rydberg states and allowed both homogeneous and inhomogeneous weak electric field to be measured by exploiting the Stark effect (see Chapter 2). In 2016 Anderson et al. [10] used an electromagnetically induced transparency scheme involving Rydberg states in rubidium to perform direct optical readout of the time-varying electric fields in high-power microwaves.

More recently, Ramsey interferometry of circular Rydberg states has been utilised to realise high-sensitivity magnetometers [11]. Whereas previous related atomic magnetometers were limited by the magnetic moments of the ground states of the atoms used, which never exceed 10 μ_B [12], circular Rydberg states allowed for significantly greater magnetic moments of $\pm(n-1)\mu_B$. In this work Dietsche et al. [11] employed a series of laser, microwave and radio-frequency pulses to first create an equal superposition of the $|n = 52, m_\ell = 0\rangle$ and $|n = 52, m_\ell = +2\rangle$ states in rubidium. Then, from these, they prepared the two $n = 52$ circular Rydberg states with maximum and opposite magnetic moments, i.e., $|52c^+\rangle \equiv |n = 52, m_\ell = +51\rangle$ and $|52c^-\rangle \equiv |n = 52, m_\ell = -51\rangle$, while maintaining the superposition. The large difference in magnetic moments between these states make the superposition extremely sensitive to magnetic fields which cause a particular phase accumulation. After returning the circular states to the initially prepared $|n = 52, m_\ell = 0\rangle$ and $|n = 52, m = +2\rangle$ basis states the atoms were probed to complete a Ramsey interferometry sequence. Scanning the phase of the Ramsey interferometry pulses and applying state-selective detection allowed the phase shift of the superposition to be measured and subsequently the magnetic field to be determined. Figure 1.5 shows the phase shift resulting from exposure to magnetic fields and measurements of weak magnetic fields with strengths of between 16 and 100 nT. The methods of matter-wave interferometry presented in Chapters 6 and 7 of this thesis represent a new approach to quantum sensing. They add to the existing methods for the precise determination of electric field distributions, and are particularly suited to

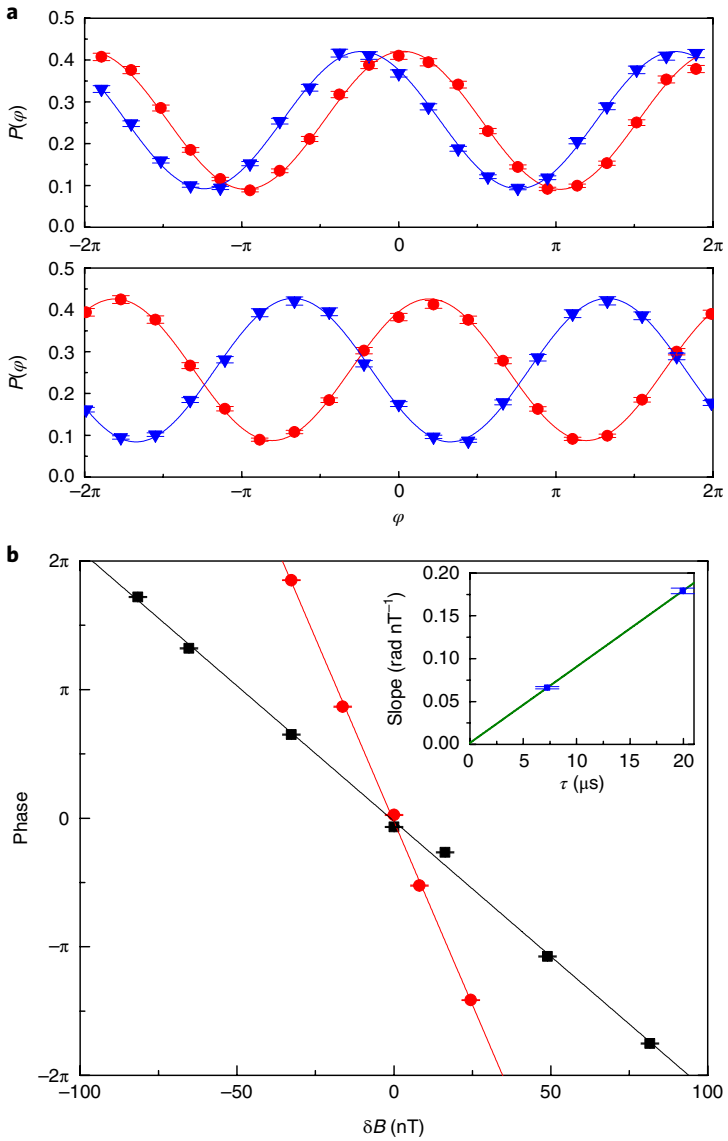

Figure 1.5: High sensitivity magnetometry with circular Rydberg states. (a) Phase shifts observed due to weak magnetic fields for interrogation times of 7.2 (top panel) and 19.9 μs (bottom panel). In both plots the red and blue traces differ in magnetic field by the same increment of 16 nT showing larger phase accumulation for longer exposure times. (b) Measured phase shift of interference signal as a function of magnetic field for interrogation times of 7.2 (black squares) and 19.9 μs (red circles). Taken from Reference [11].

the measurement of electric field gradients.

1.3 Precision tests of fundamental physics

Aside from the application of atoms in Rydberg states discussed above, they may also be utilised for precision tests of fundamental physics. For example, experiments carried out by Liu et al. [13] in 2010 employed high precision measurements of frequency intervals between Rydberg states of the hydrogen molecule to determine its ionisation and dissociation energies, achieving an improvement in the determination of these quantities over previous experimental results by more than one order of magnitude. These measurements allow stringent tests of calculations of molecular structure and bound state QED in molecules. Further developments in this work may allow a new approach to the determination of the proton charge radius and aid in the resolution of the 'proton radius' puzzle [14].

Following the recent developments in the production of cold, neutral antimatter, new experiments to test the weak equivalence principle are being proposed and undertaken [16]. Two main candidates for these types of tests are antihydrogen and positronium (Ps), an atom comprised of an electron and its anti-particle, the positron. Since antihydrogen is synthesised in Rydberg states and the lifetime of Ps is only 142 ns unless it is excited to Rydberg states [15], techniques developed to manipulate atoms in Rydberg states, such as those described here, may be of particular importance in these experiments. Figure 1.6 shows the enhancement of the lifetime of Ps through excitation to Rydberg states. It can be seen from these measurements that the Ps lifetime can be increased by two orders of magnitude by exciting to the $n = 15$ Rydberg state.

Ps also allows an alternative approach to addressing the 'proton radius' puzzle and measuring the Rydberg constant. As the energy levels in 'ordinary' matter are dependent on both the Rydberg constant and the charge radius of the proton,

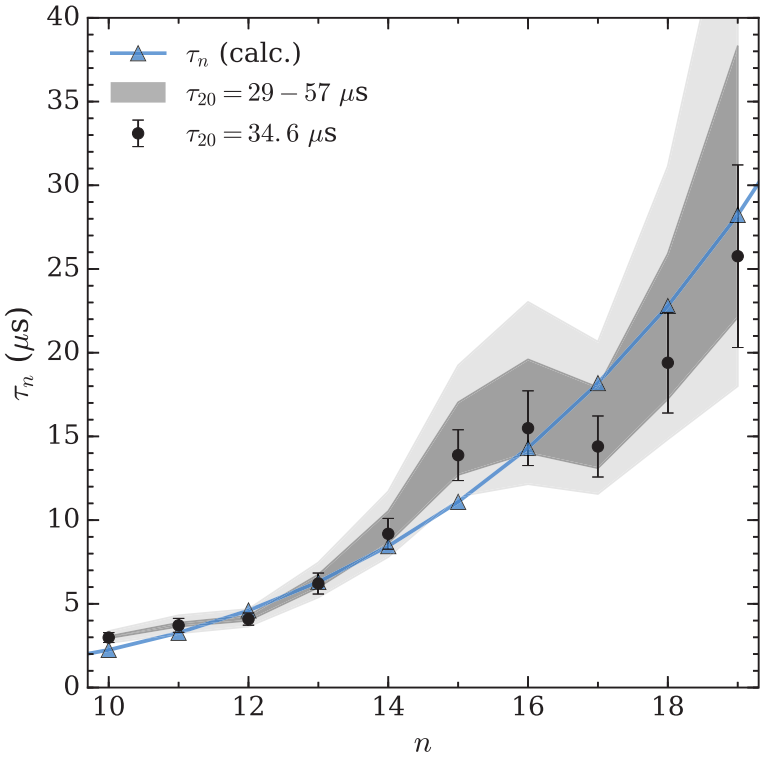

Figure 1.6: Measured and calculated lifetimes of Rydberg states of Ps with values of n between 10 and 19. From Reference [15].

through the Lamb shift, any spectroscopic attempt to determine either of these values is inextricably limited by the known precision of the other. Since Ps contains no protons, this problem could be avoided and spectroscopy could allow for a new precision measurement of the Rydberg constant which could then in turn be applied in proton charge radius measurement experiments. Rydberg Ps atoms are also of interest in measurements of antimatter gravity and tests of the weak equivalence principle for particles containing antimatter. The methods of Rydberg atom interferometry presented in Chapters 6 and 7 of this thesis are particularly suited to gravity measurements with Ps atoms, providing an alternative to already proposed free-fall studies that could be performed over shorter distances and time scales.

Chapter 2

Theoretical background

2.1 Rydberg atoms and molecules in electric fields

The Hamiltonian for a single electron atom under the influence of an external electric field $\vec{F} = (0, 0, F_z)$, directed along the z-axis can be expressed as

$$H_0 = -\frac{\hbar^2}{2m_e}\nabla^2 - \frac{e^2}{4\pi\epsilon_0 r} + eF_z z, \tag{2.1}$$

where $\hbar = h/2\pi$, m_e is the electron mass, ϵ_0 is the permittivity of free space and r is the distance of the electron from the proton. The operator associated with the interaction with the electric field in this expression couples states for which $\Delta\ell = \pm 1$ and $\Delta m_\ell = 0$. The result of this is that a manifold of ℓ-mixed Stark states can be associated with each value of the principle quantum number, n. In hydrogenic systems these states are characterised by the index $k = n_1 - n_2$, where n_1 and n_2 are the parabolic quantum numbers obtained by solving the Schrödinger equation for a Coulomb potential in parabolic coordinates. For each value of n, the values of k range from $-(n - |m_\ell| - 1)$ to $+(n - |m_\ell| - 1)$ in steps of two. Each of the resulting Stark states possesses a static electric dipole moment of

$$\vec{\mu}_{\text{elec}} = -(3/2)nkea_0. \tag{2.2}$$

In the presence of an electric field the energy shift of each of these states is

$$E_{\text{Stark}} = -\vec{\mu}_{\text{elec}} \cdot \vec{F} \tag{2.3}$$

where $\vec{F}$ is the electric field vector.

The electric dipole moments associated with these states arise as a result of the localisation of the electron charge with respect to the ion core. The mixed-ℓ character of the wavefunctions of the Stark states gives rise to interferences that result in the corresponding charge localisation and electric dipole moments.

In an inhomogeneous electric field, atoms in these states with non-zero electric dipole moments will experience a force

$$\begin{aligned} \vec{f} &= -\nabla E_{\text{Stark}} \\ &= \nabla(\vec{\mu}_{\text{elec}} \cdot \vec{F}). \end{aligned} \tag{2.4}$$

If the state's electric dipole moment is aligned parallel to the electric field, the force will be directed towards regions of high field. Because of this, these states are called high-field-seeking (HFS) Rydberg-Stark states. Conversely, if the state's electric dipole moment is aligned anti-parallel to the electric field the atoms will experience a force towards regions of low field strength and are therefore called low-field-seeking (LFS) Rydberg-Stark states. Figure 2.1(a) is a Stark map which shows the dependence of the energies of hydrogenic Rydberg-Stark states on electric field strength for values of n between 7 and 14. Electron probability density distributions corresponding to four of the Rydberg-Stark states with $n = 8$ can be seen in Figure 2.1(b). The forces experienced by atoms in these states in inhomogeneous electric fields are central to the operation of Rydberg-Stark decelerators and traps for atoms and molecules in high Rydberg states, and for the beam splitters and interferometers described here.

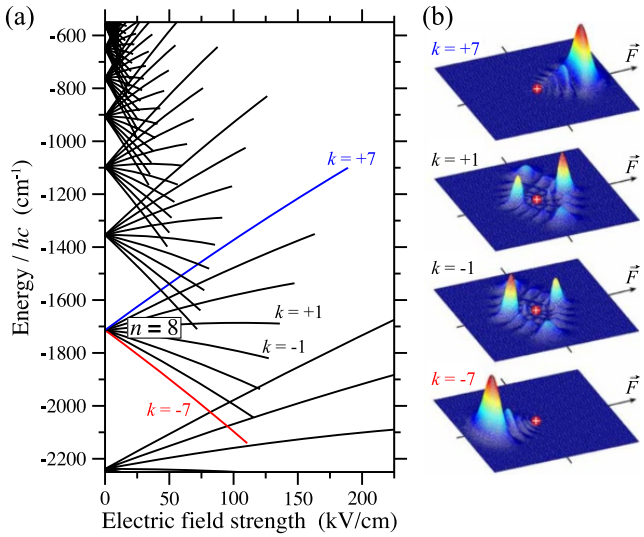

Figure 2.1: (a) Stark map with an extreme HFS state shown in red and an extreme LFS state shown in blue. (b) Electron probability densities corresponding to the four values of k with $n = 8$ indicated. From Reference [2].

2.2 Rydberg-Stark deceleration

2.2.1 Time-independent electric fields

The forces experienced by atoms in LFS and HFS Rydberg states in inhomogeneous electric fields can be exploited to control their motion. The first experimental demonstration of this was reported by Townsend et al. in 2000 [17]. This experiment was analogous to the classic Stern-Gerlach experiment in which the quantisation of angular momentum was first demonstrated [18]. A diagram of the apparatus used by Townsend et al. can be seen in Figure 2.2(a). It consisted of two cylindrical electrodes arranged parallel to each other with a potential of +500 V applied to one and -500 V to the other. This configuration resulted in the generation of a time-independent inhomogeneous electric field with a region of high field between the two electrodes that decreased in strength with increasing vertical position. A

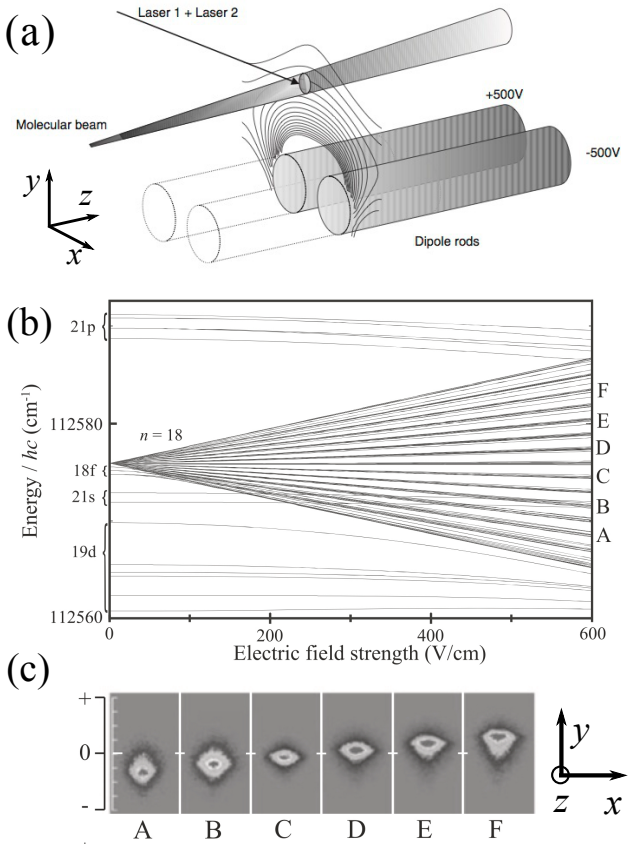

Figure 2.2: (a) Rydberg Stern-Gerlach experiment. (b) Stark map showing selected Rydberg-Stark states in krypton, and (c) final vertical position of atoms in the states labelled in (b) after deflection. States A, B and C are HFS states, whilst states D, E and F are LFS states. From Reference [17].

beam of krypton travelled parallel to, and above, the electrodes and the atoms were photoexcited to a specific Rydberg-Stark state by intersecting the atomic beam with two laser beams in the electric field. The excited atoms then experienced a force due to the inhomogeneous electric field. The magnitude and direction of this force depended on the electric dipole moment of the Stark state excited. The effect of this force on the beam of atoms was monitored by imaging the signal from the excited atoms recorded when they impinged upon a microchannel plate (MCP) detector. Experiments were performed for a number of Rydberg-Stark states with both positive and negative Stark shifts and the results can be seen in Figure 2.2(b) and (c). Figure 2.2(b) shows the range of Rydberg-Stark states used in the experiments and Figure 2.2(c) displays the final vertical position of the atoms in those states at the detector. It can be seen that atoms in the HFS states A and B were deflected downwards towards the electrodes where the field strength was highest. Atoms in the LFS states E and F were deflected upwards away from the electrodes and towards the area of low field strength. The centre Stark states C and D have small electric dipole moments and thus atoms prepared in these states experienced little force and their positions remained relatively unchanged.

Following this, experiments performed by Procter et al. in 2003 [19] and Yamakita et al. in 2004 [20] using hydrogen molecules utilised time-independent inhomogeneous electric fields to demonstrate the first longitudinal acceleration and deceleration of Rydberg molecules. Figure 2.3 shows the results of the latter experiment in which H_2 molecules in HFS Rydberg-Stark states were accelerated resulting in a shorter time of flight compared to LFS states which were decelerated and experienced a longer time of flight to a detector at a fixed distance from the Rydberg state photoexcitation position.

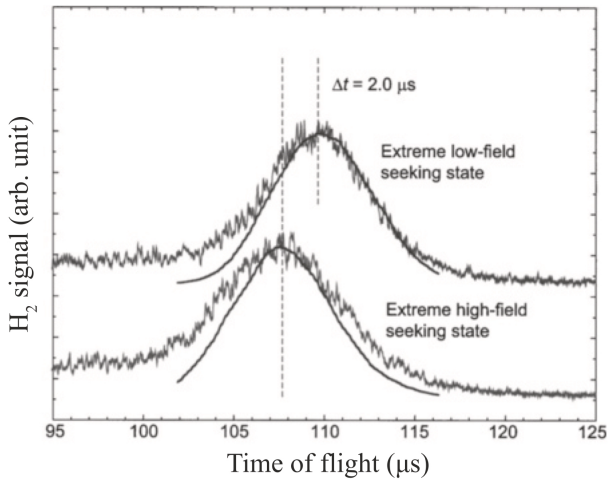

Figure 2.3: Time-of-flight distributions showing acceleration/deceleration of H_2 molecules in HFS (bottom curve) and LFS (top curve) Rydberg-Stark states. From Reference [20].

2.2.2 Time-dependent electric fields

The use of time-dependent electric fields enabled Vliegen et al. to exert greater control over the motion of atoms in Rydberg-Stark states in order to focus [21] and reflect [22] beams of argon and hydrogen atoms, respectively, before Hogan and Merkt demonstrated the first three-dimensional electrostatic trap [23] for samples in such states. The apparatus used in this experiment consisted of a three-dimensional configuration of six electrodes to which time-dependent voltages were applied. A schematic diagram of the electrode structure can be seen in Figure 2.4(a). Depending on the potentials applied to the electrodes, fields that controlled the motion of Rydberg-Stark states in three different ways could be generated. In the first phase of the experiment, exponentially decaying potentials applied to electrodes 1 and 2 decelerated samples of hydrogen atoms in LFS states while ensuring they never entered a field large enough to ionise them. Once the atoms were decelerated to zero mean velocity in the laboratory-fixed frame of reference they were trapped

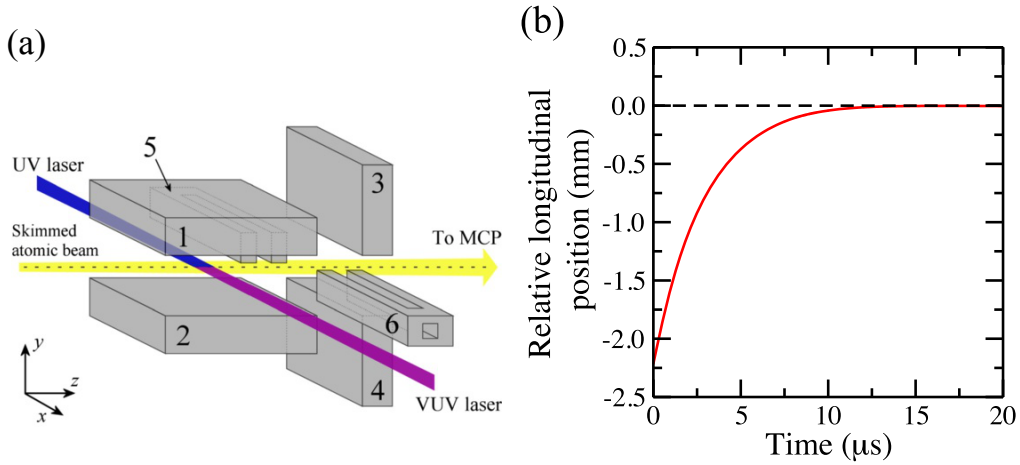

Figure 2.4: Deceleration and trapping of hydrogen atoms using time-dependent electric fields. (a) Electrode structure, and (b) calculated mean longitudinal position of the decelerated atoms, relative to the position of the trap minimum in the z dimension, as a function of time. From Reference [23].

by applying potentials to all six electrodes to create a three-dimensional trap. The velocity spread of the atoms was ± 50 m·s^{-1}. Finally the trapped atoms were ionised upon the application of large positive potentials to electrodes 1 and 2. The resulting ions were then detected at an MCP detector. The calculated mean longitudinal position of the decelerated atoms in these experiments can be seen in Figure 2.4(b).

Seiler et al. extended this work on three-dimensional trapping of hydrogen atoms by demonstrating trapping of atoms in Rydberg states [24] off the atomic beam axis in order to reduce losses due to collisions with the carrier gasses in the supersonic beams used in these types of experiments. Figure 2.5 shows the location of eight electrodes used for decelerating and trapping in this work and the electric fields generated at each stage of the deceleration process implemented to load the atoms into the off-axis trap. Figure 2.5(a) indicates the initial and final electric field distribution, an incoming ensemble of atoms and a trapped one. The atoms were

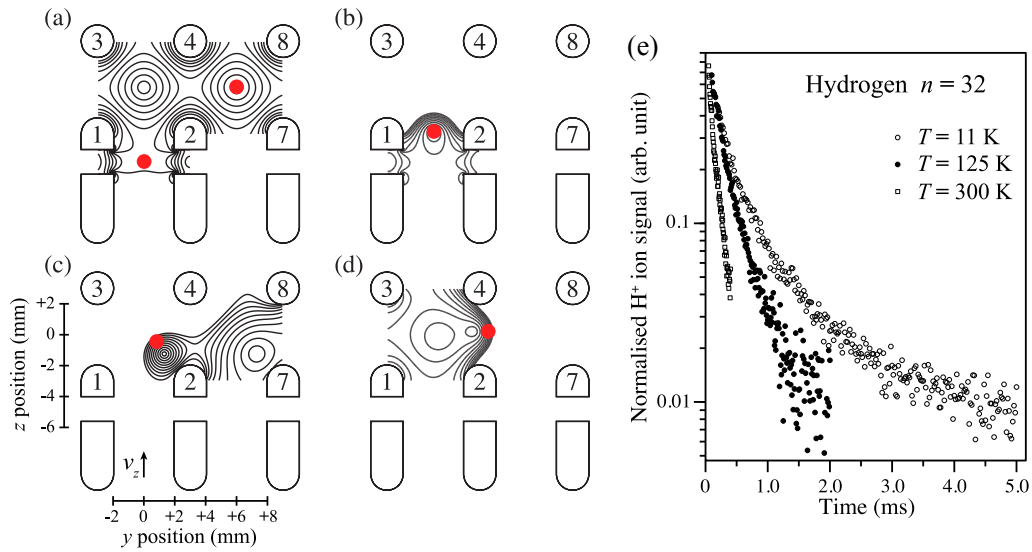

Figure 2.5: (a-d) Electrode structure and time dependent electric field distributions for deceleration and off-axis trapping of hydrogen atoms. (e) Signal from the trapped atoms recorded for increasing trapping times at three different temperatures, as indicated. From Reference [24].

decelerated [Figure 2.5(b)], deflected by 90° [Figure 2.5(c)] and decelerated again [Figure 2.5(d)] before ending up trapped as shown in Figure 2.5(a). These trapping experiments allowed the possibility of investigating effects of collisions and excited state decay processes on timescales that were previously inaccessible. Figure 2.5(e) shows the decay of the population of trapped atoms in trap environments at three different temperatures: 300 K, 125 K and 11 K. The longer trapping times at lower temperature are a consequence of the reduced effects of blackbody transitions, in particular, blackbody photoionisation.

2.3 Chip-based devices for manipulating atoms and molecules with electric fields

The next development in manipulating the motion of atoms and molecules in high Rydberg-Stark states was to extend what had been done with three-dimensional electrode configurations to two-dimensional ones, i.e., chip-based devices. Chip-based devices have numerous advantages over three-dimensional structures. The first is that they are generally easier to scale to include more deceleration stages to decelerate heavier samples. This is an advantage in itself but it also leads to another advantage: the smaller the devices, the larger the field gradients that can be produced with a given set of low potentials, allowing for greater forces to be exerted during deceleration and trapping.

The first demonstration of a chip-based Stark decelerator was reported by Meek et al. [25] in 2009. Instead of using samples in Rydberg states, these experiments used ground state polar molecules, which also possess LFS states and can be decelerated by exploiting the Stark effect. The electric dipole moments of these ground state molecules are, however, only on the order of 1 D so $\sim 1/1000$ of those of Rydberg states. This decelerator relied on the superposition of electric fields created by time-varying voltages applied to sets of electrodes on the chip to generate moving electric field minima. When two dipolar fields with different length scales and opposite directions are superimposed, a minimum of electric field strength is created. This forms a trap for samples in LFS states. An array of electric field minima is generated using a set of voltages with each electrode connected to others which are multiples of seven away. This results in an electric field distribution that repeats every seven electrodes.

Figure 2.6 shows the calculated electric field distribution in this type of chip decelerator for polar ground state molecules for three different sets of potentials

applied to the electrodes. In panels (a)-(c), times are chosen to represent times t_a, t_b and t_c such that $\omega(t_b - t_a) = \omega(t_c - t_b) = \pi/6$. If the electrodes are numbered 1-6, the voltage at the nth electrode, for odd n, in panel (a), is given by $-V_0[1+\cos(\omega t_a + \phi n)]$ where $V_0 = 60V$, and $(\omega t_a + \phi n) = 120°, 240°$ and $0°$ for n=1, 3 and 5, respectively. For even n the voltage on each electrode is given by $V_0[1 + cos(\omega t_a + \phi n)]$ where $(\omega t_a + \phi n) = 0°, 120°$ and $240°$ for n=2, 4 and 6, respectively. The potential on any given electrode is equal in magnitude but opposite in sign to the potential on the electrode three positions away.

The calculated fields in Figure 2.6 show that the resulting minima, or traps, can be positioned exactly between two electrodes (a), three quarters of the distance between one electrode and the next (b), or directly above an electrode (c). By applying appropriate potentials, the minima can be generated at any z-position whilst keeping the y-position constant. This allows the traps to move smoothly above the chip surface if appropriate time-dependent potentials are applied. The speed at which the traps move above the surface is governed by the frequency, ω, at which the potentials applied to the electrodes oscillate in time. Once an ensemble of atoms are confined in the moving traps in this device, they can be accelerated by increasing ω, or decelerated by decreasing it.

Figure 2.7(a) shows the chip decelerator structure used in these experiments. It consisted of an array of 1254 10-μm-wide, 100-nm-high gold electrodes on a glass substrate with a centre-to-centre separation of 40 μm. They were connected, via nickel wires, to square pads by which the six different time-dependent potentials were applied. The length of the electrode array was 50.16 mm. The experimental setup is show in Figure 2.7(b). The chip decelerator was mounted on a manipulator that allowed for adjustment of the height of the front and back of the chip with a precision of better than 10 μm and allowed the structure to be tilted with a precision of better than 0.01°.

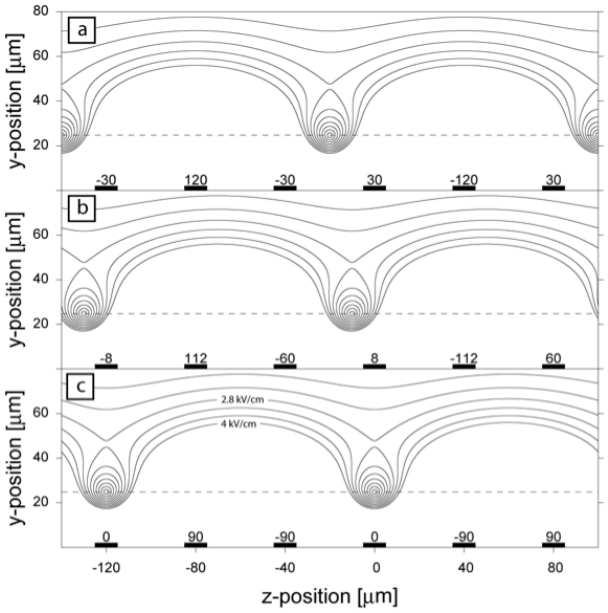

Figure 2.6: Calculated electric field distributions for three different sets of potentials applied to the electrodes of a chip-based Stark decelerator for polar molecules showing how traps can be generated at any z position above the chip. See text for details. From Reference [25].

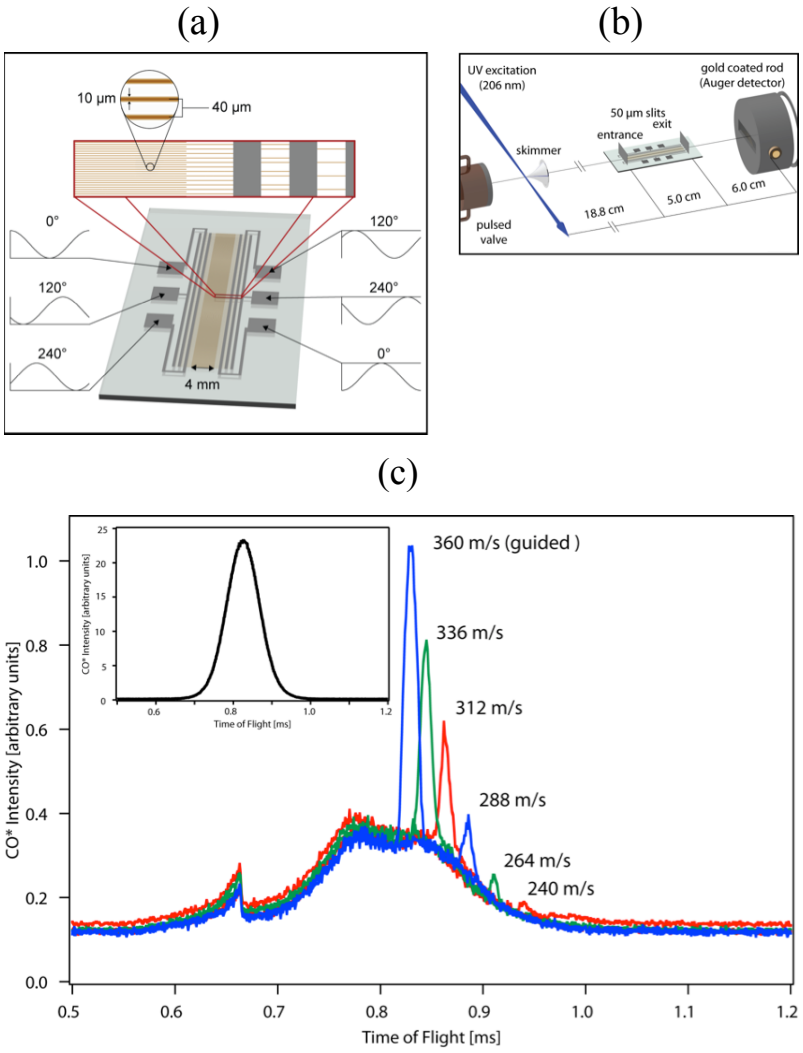

Figure 2.7: (a) and (b) chip design and experimental setup used by Meek et al. [25] to demonstrate deceleration of CO in a chip-based Stark decelerator. (c) Results of experiments showing guiding and deceleration to five different final speeds. From Reference [25]

To demonstrate the operation of this device, a pulsed beam of ground state CO molecules was produced by expanding a mixture of CO and argon through a solenoid valve to a vacuum. The valve body was cooled to 102 K to set the mean velocity of the CO molecules to 360±20 $m{\cdot}s^{-1}$. Before passing through a skimmer, the CO molecules, which have no ground state electric dipole moment, were prepared in an LFS metastable state by direct laser excitation from the $N'' = 1$ rotational level in ground state. At a distance ~19 cm downstream from the laser excitation point, the molecules passed through a slit and then travelled closely above the microstructured electrode array over its full 5 cm length. When the molecules arrived above the electrode array, the potentials were switched on. This occurred 530 μs after laser excitation. The position of the excitation laser was 188 mm from the first electrode of the decelerator so the molecules, travelling at the mean velocity of 360 $m{\cdot}s^{-1}$, had already passed over 3mm of the decelerator before it was activated. Molecules travelling at 355 $m{\cdot}s^{-1}$ had just reached the first electrode. A small fraction of the molecules found themselves in the electric field minima while the majority were deflected by the strong electric field gradient that was present everywhere else. When the electric field minima were moved at the appropriate initial velocity, by allowing the decelerator potentials to oscillate in time, the CO molecules were confined in the moving traps for the entire time the potentials were applied. When the molecules approached the end of the electrode array, the potentials were switched off again. The exact period of time for which the potentials were kept on depended on the amount of acceleration imposed but it was always chosen such that it corresponded to a total travel distance of the molecules guided or decelerated above the chip of 46 mm. The molecules that had been stably transported over this distance could pass through an exit slit and then fly freely to a gold surface 6 cm downstream. As the metastable CO molecules had 6 eV of internal energy, they generated free electrons upon impacting the gold surface.

These electrons were subsequently detected using an MCP detector.

Figure 2.7(c) shows the measured arrival time distributions of the metastable CO molecules at this detection region for six different values of applied acceleration. The inset shows the measured arrival time distribution when no potentials were applied to the electrodes. It shows that the velocity distribution of the CO molecules in the beam was centred on 360 m·s^{-1}. Once the molecules reached the decelerator and the waveforms were switched on, those that were not initially trapped in one of the moving traps were deflected away from the surface. Even molecules that were initially in a trap but had too large a velocity soon found their way out and then were pushed away from the surface. In the guiding case, when the waveforms remained at 3.0 MHz for the entire time that the molecules were above the chip, the molecules in the wells were transported to the end of the chip without their velocities changing significantly. The resulting time of flight spectrum exhibits a broad background, on top of which can be seen an intense, narrow peak centred at 0.83 ms, i.e., the time that it takes molecules travelling at 360 m·s^{-1} to travel the 29.8 cm distance from the excitation zone to the detector. The broad background was caused by metastable CO molecules with trajectories that were not influenced by the electric fields of the decelerator.

The other five arrival time distributions shown in the main panel of Figure 2.7(c) were recorded when the frequency of the decelerator waveforms was reduced linearly from 3.0 MHz to a final value of 2.8 MHz (336 m·s^{-1}), 2.6 MHz (312 m·s^{-1}), 2.4 MHz (288 m·s^{-1}), 2.2 MHz (264 m·s^{-1}) and 2.0 MHz (240 m·s^{-1}). The last of these measurements corresponds to a deceleration with a magnitude of $a = 0.78\ \mu\text{m}\cdot\mu\text{s}^{-2}$. It is seen that the narrow peak in arrival times that results from the CO molecules that are captured in the potential wells comes at even later times, in agreement with the expected arrival times. The broad background, however, remains constant regardless of the applied potential, showing that it represents molecules that do not

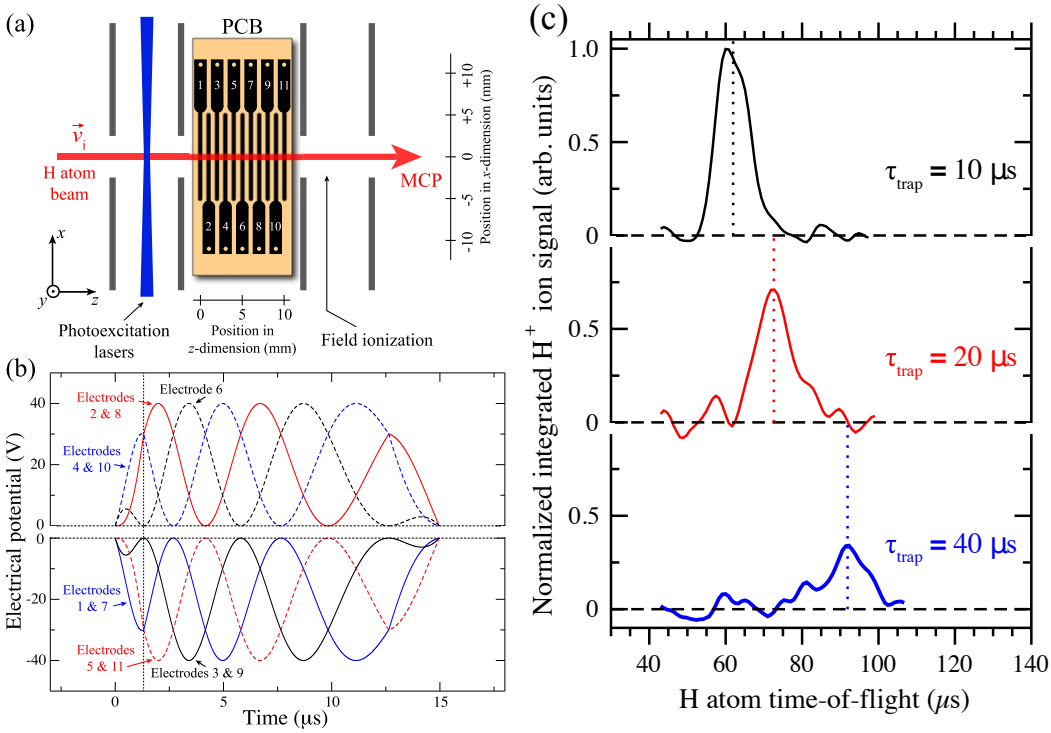

Figure 2.8: (a) Experimental setup, and (b) time dependent potentials used for deceleration and trapping of hydrogen Rydberg atoms in a chip-based Rydberg-Stark decelerator.(c) Time-of-flight distributions recorded after electrostatic trapping times of 10, 20 and 40 μs. From Reference [8].

interact with the electric fields. It is seen that the number of molecules trapped in the potential wells decreases for increasing acceleration. This is to be expected as the volume and the depth of the potential wells effectively reduce with increasing accelerations.

Building on this work, Hogan et al. [8] demonstrated the first deceleration of atoms in Rydberg states, in this case H atoms, using two-dimensional chip-based electrode structures. Owing to the much larger electric dipole moments of the Rydberg-Stark states used in this work compared to those of polar CO molecules,

combined with the lower mass of the atoms used, the chip dimensions could be scaled up and the device could be operated using lower electric potentials allowing much larger samples of atoms to be trapped and decelerated. A diagram of the chip structure used for these experiments can be seen in Figure 2.8(a). It consisted of 11 0.5-mm-wide electrodes with a centre-to-centre separation of 1 mm. The chip was operated in the same way as the decelerator for polar molecules; by applying six different oscillating potentials to electrodes 1-6 and repeating the sequence from electrode 7 onwards they created a series of travelling traps above the chip, with each pair separated along the axis of the atomic beam by 3 mm. The speed that the traps moved at was proportional to the frequency of the oscillating potentials applied. Figure 2.8(b) shows the potentials that were applied to the 11 electrodes in order to decelerate hydrogen atoms in LFS states from 760 $m{\cdot}s^{-1}$ to 300 $m{\cdot}s^{-1}$. These states were prepared by photoexcitation using a resonance-enhanced two-colour two-photon excitation scheme from the $1\,^2S$ ground state via the $2\,^2P$ state in a homogenous electric field of 33 $V{\cdot}cm^{-1}$. After travelling over the length of the decelerator the atoms were detected by pulsed electric field ionisation with the resulting ions collected on an MCP detector. This chip-based Rydberg-Stark decelerator was used to accelerate and decelerate samples of Rydberg atoms to velocities between 1200 $m{\cdot}s^{-1}$ and 200 $m{\cdot}s^{-1}$ before demonstrating electrostatic trapping. In the trapping experiments, the samples were fully decelerated to zero velocity and trapped above the surface of the chip by holding the potentials applied to the electrodes at a constant value. After trapping times of 10, 20 and 40 μs the samples were re-accelerated and detected. Results of these experiments are shown in Figure 2.8(c). It can be seen that the difference in arrival times of the three samples exactly matches the difference in trapping times. These data also show a reduction in signal intensity with increasing trapping time. This was identified to be a result of collisions with the trailing parts of the pulsed supersonic beam.

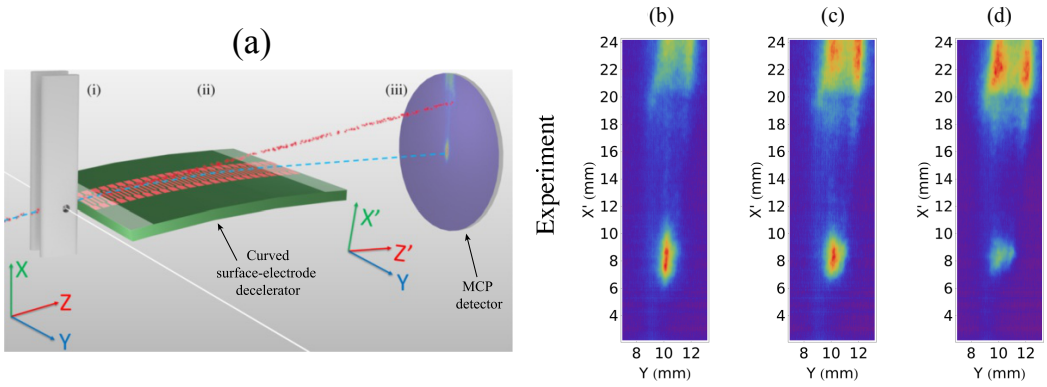

Figure 2.9: (a) Experimental setup, and (b-d) results of experiments to demonstrate off-axis deflection and guiding of H_2 Rydberg molecules by Allmendinger et al. From Reference [26].

To avoid collisional losses Allmendinger et al. [26] subsequently used a curved chip to achieve off-axis deceleration and deflection of hydrogen Rydberg molecules. As can be seen in Figure 2.9(a), the chip consisted of a 50-mm array of 50 electrodes, the first 4 mm and last 3.5 mm of which were planar while the middle 42.5 mm section formed the arc of a circle in the xz plane with radius 244 mm. This corresponds to a deflection of 10° from the initial axis of propagation of the molecular beam. In these experiments a pulsed beam of molecular hydrogen was collimated and then passed between two electrodes where the molecules were photoexcited to LFS states in a homogeneous electric field of 75 V·cm^{-1}. After passing over the chip, the molecules were imaged directly using an MCP detector to determine their position in the xy plane. Figure 2.9(b) shows images recorded following deflection/guiding at a constant longitudinal speed of 1290 m·s^{-1} for waveform amplitudes of 80, 60 and 40 V applied to the chip electrodes. The sharp regions of signal in the bottom portion of the images correspond to the guided and deflected ensemble of atoms and show that for higher voltages, a higher proportion of molecules are guided

because of the stronger forces exerted on them. Using trajectory simulations, it was calculated that the deflection efficiency of the device was 20% when operated at 80 V and 10% when operated at 40 V. This effect is mirrored by the signal arising from the unguided portion of the beam at the top of each image; fewer guided molecules results in more signal in the undeflected beam. The double peak structure in the y dimension in the undeflected component can be attributed to the finite transverse phase-space acceptance of the deflector. Molecules that are initially close to the centre of the chip had a higher chance of being trapped by the guide and deflected downwards, which decreased the signal in the middle of the unguided portion of the beam. In these experiments, simultaneous deflection and deceleration of H_2 was also demonstrated.

2.4 Transmission-line guides, decelerators and traps

All of the chip-based Rydberg-Stark deceleration devices described so far exhibit strong particle confinement in two dimensions, the vertical (deflection) and longitudinal (acceleration and deceleration) directions, but the samples were more weakly confined in the horizontal direction. To manipulate atoms and molecules in Rydberg-Stark states in these types of decelerators with improved efficiency, devices were developed that were capable of generating strong traps in all three dimensions. To this end, in 2013 Lancuba and Hogan began a series of experiments using chip-based devices for Rydberg-Stark deceleration based on the geometry of coplanar electrical transmission-lines [27, 28, 29]. This geometry also allows integration with chip-based microwave circuits.

The first experiment performed as part of this work involved the demonstration of an electrostatic transmission-line guide for He atoms in Rydberg-Stark states [27]. This guide was used to generate two-dimensional traps in the horizontal and vertical directions to control the transverse motion of atoms in LFS states. A schematic

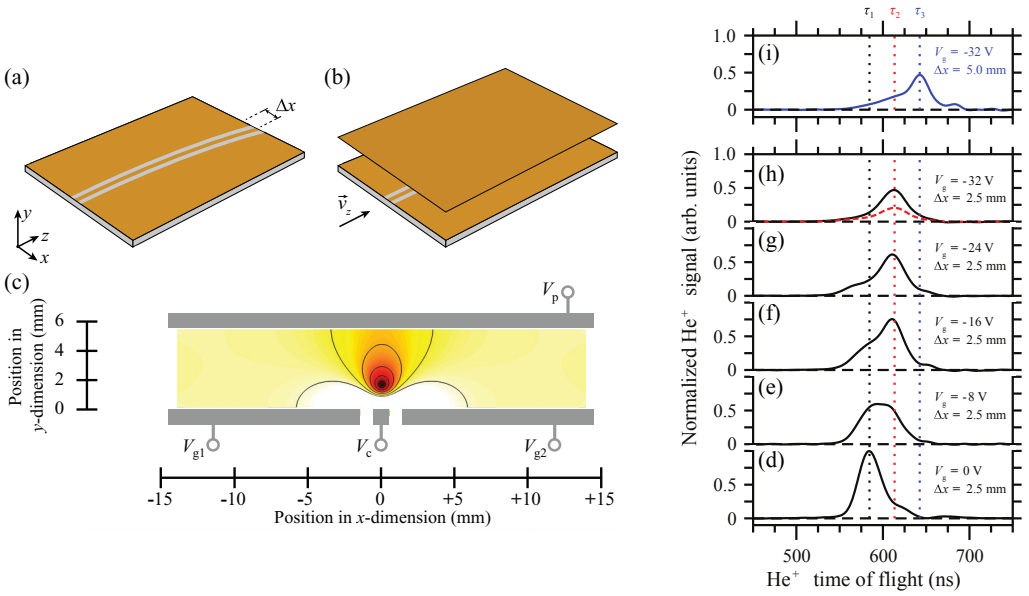

Figure 2.10: (a) and (b) transmission-line guide design, (c) electric field distribution and (d-i) experimental data demonstrating the operation of the guide with Rydberg He atoms. From Reference [27].

diagram of the chip structure used in these experiments is displayed in Figure 2.10. It consisted of a curved 1 mm wide centre conductor electrode separated from ground planes on either side by 1 mm [Figure 2.10(a)] with a plane metal plate electrode situated parallel to, and 5.6mm above, the surface of the chip [Figure 2.10(b)]. Equal electric potentials were applied to the centre conductor electrode and the upper metal plate and with the ground planes set to 0 V, the four electrodes created a quadrupole trap in the x (transverse) and y (vertical) dimensions as can be seen in Figure 2.10(c).

In these experiments a pulsed supersonic beam of metastable He atoms was generated in a dc electric discharge at the exit of a pulsed valve. After passing through a skimmer, the atoms were photoexcited from the metastable 1s2s $^3S_1$ level to Rydberg states with $n = 52$ via the 1s3p $^3P_2$ intermediate state in a homogeneous

electric field of 0.6 V·cm^{-1}. In this excitation process selected LFS Rydberg-Stark states were prepared. The atoms then travelled through the device, to which a range of deflection potentials were applied, before detection by pulsed electric field ionisation. After being ionised, the resulting He^+ ions were accelerated in the x direction to an MCP detector. By measuring the time between the application of the ionisation pulse and the subsequent arrival of the ions at the detector, time-of-flight distributions could be obtained that revealed changes in the relative position of the guided atoms in the x dimension at the time of ionisation. These time-of-flight distributions can be seen in Figure 2.10(d-i) for a range of guiding potentials, V_g, using two guides with different radii of curvature, and hence end point displacements, Δx. It can be seen from the data that increasing the guiding potential from $V_g = 0$ to -32 V [Figure 2.10(d-h)] resulted in longer mean flight times of the He^+ ions to the MCP directly reflecting an increased displacement in the x dimension of the atoms at the time of ionisation. This mean time-of-flight increased further when the experiment was repeated using a guide with a greater end point displacement of 5.0 mm [Figure 2.10(i)].

To generate fully three-dimensional traps using this transmission-line electrode geometry, Lancuba and Hogan subsequently divided the centre conductor into discrete, individually addressable, segments to realise a transmission-line decelerator [28], the design of which can be seen in Figure 2.11(a). A series of 1 mm × 1 mm centre conductor electrodes in this device were again separated from two ground planes by 1 mm with an upper plate electrode 4.5 mm above. By applying potentials to each electrode, labelled with the index $i = 1, 2, ...$, according to the expression

$$V_i = V_0 \cos[-(i-1)\phi], \tag{2.5}$$

where V_0 is the potential applied to electrode 1 and $\phi = 5/2$ is the phase shift from one electrode to the next, and with a fixed potential of $-V_0/2$ applied to the

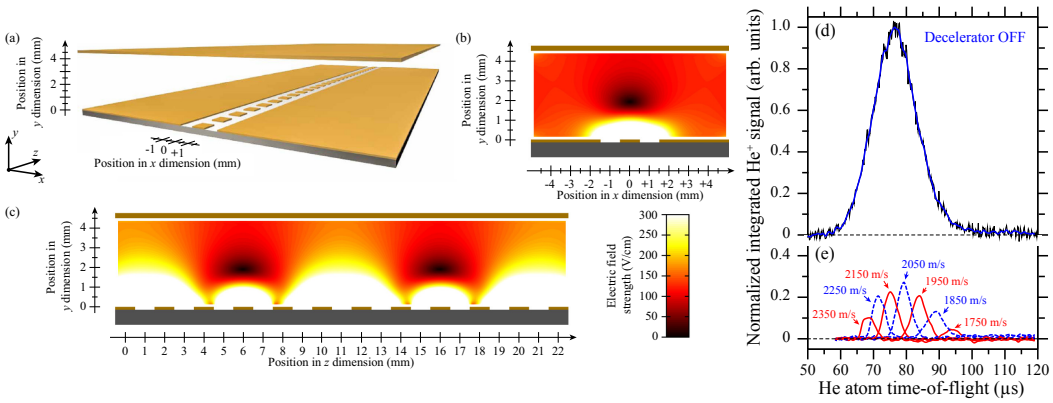

Figure 2.11: Transmission-line decelerator (a) design, (b) and (c) electric field distributions in the xy and yz planes, and time-of -flight distributions for (d) unguided atoms and (e) atoms accelerated and decelerated to seven different speeds. From Reference [28].

upper plate electrode, the electric field distributions seen in Figure 2.11(b) and (c) were generated. As can be seen, electric field minima formed in both the xy and yz planes, resulting in fully three dimensional traps capable of confining atoms in LFS Rydberg-Stark states in the transverse, longitudinal and vertical directions. By introducing a time dependence to the electric potentials of the form

$$V_i(t) = V_0 \cos[\omega t - (i-1)\phi], \tag{2.6}$$

where ω is the frequency of the oscillation of the potential applied to each electrode, the traps could be caused to travel smoothly above the surface of the chip. The speed with which the traps moved was given by

$$v_{\text{trap}} = 5 d_{\text{cc}} \omega / (2\pi), \tag{2.7}$$

where d_{cc} is the centre-to-centre separation of the conductor electrodes. The dependence of the speed of the traps on the frequency of the oscillating potentials was exploited to accelerate and decelerate He atoms.

He atoms in LFS Rydberg-Stark states were loaded into the travelling traps of this device by switching on the electric potentials when the atoms were at the appropriate position above the electrode structure. The frequency at which these potentials then oscillated was calculated to initially match the speed of the trap with the speed of the incoming atoms, 1950 $\mathrm{m{\cdot}s^{-1}}$. Once trapped, the atoms were either guided, by keeping the oscillation frequency constant, accelerated, by chirping the frequency up over time, or decelerated, by chirping the frequency down over time, before detection by pulsed electric field ionisation and collection of the resulting ions on an MCP detector, as before. By measuring the total time of flight of the atoms through the device between photoexcitation and detection, the speeds to which the atoms were accelerated or decelerated could be calculated. The time-of-flight distributions for several different accelerations and decelerations are seen in Figure 2.11(d). These results show accelerations of $a_t = +2.0 \times 10^7$ and -1.15×10^7 $\mathrm{m{\cdot}s^{-2}}$ to speeds of 2700 $\mathrm{m{\cdot}s^{-1}}$ and 1350 $\mathrm{m{\cdot}s^{-1}}$, respectively.

The last test for these transmission-line Rydberg-Stark deceleration devices was to demonstrate full deceleration to zero velocity in the laboratory-fixed frame of reference. This was achieved by Lancuba and Hogan in 2016 [29]. In the corresponding experiments, a similar setup to the previous two was used but *in situ* detection of the Rydberg atoms was implemented. In this scheme, He atoms were prepared in the same way and decelerated above the segmented centre conductor of the transmission-line, however, once the atoms were above a preselected centre conductor electrode, a large pulsed potential was applied to the ground planes, to ionise the atoms and accelerate the resulting ions through an aperture in the upper plate electrode to an MCP detector. A diagram depicting this scheme can be seen in Figure 2.12.

By applying a constant acceleration of $a_t = -1.279 \times 10^7$ $\mathrm{m{\cdot}s^{-2}}$, atoms were fully decelerated to zero mean velocity in the laboratory-fixed frame of reference and

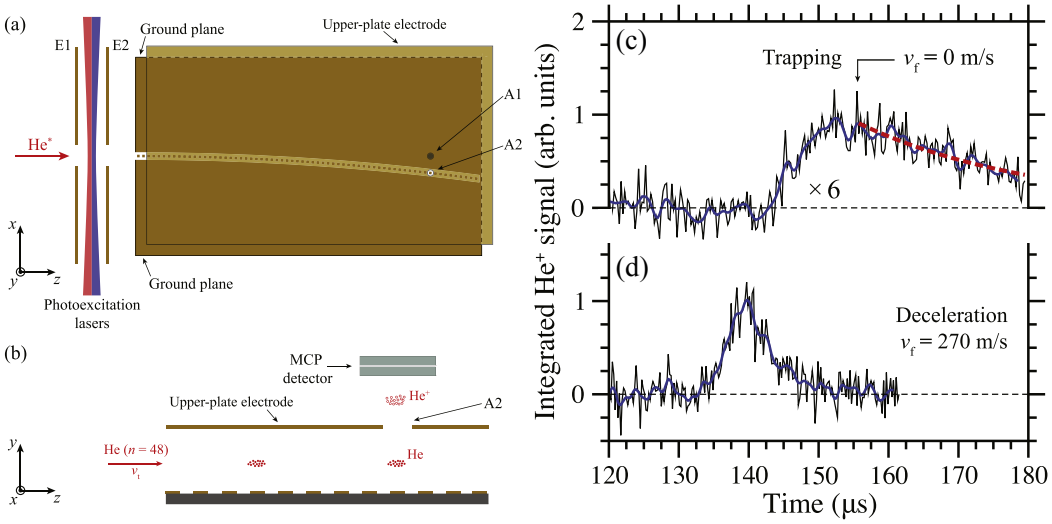

Figure 2.12: (a) and (b) experimental setup for trapping and *in situ* detection of He atoms in a transmission-line Rydberg-Stark decelerator. Time-of-flight distributions showing (c) the decay of trapped atoms, and (d) deceleration of atoms to 270 m·s^{-1}. From Reference [29].

trapped directly beneath the detection aperture. Figure 2.12(a) shows the signal measured when the ionising pulse was applied over a range of times. At early times, no atoms reached the ionisation region and no signal was detected. As the front of the ensemble of decelerated atoms approached the detection position the signal increased up to a time of 156 μs, after which all of the trapped atoms were detected. The measurements after 156 μs represent the *in situ* detection of the decay of the trapped atoms. From this data, a decay time constant of 25 μs was determined, which can be seen as a red dashed curve in Figure 2.12(c). This comparatively short decay time was attributed to effects of blackbody radiation and collisions between the background gas and the trapped atoms. For comparison, a time-of-flight spectrum corresponding to a deceleration to 270 m·s^{-1} can be seen in Figure 2.12(d).

2.5 Beam splitters

In recent years, devices have been developed that use inhomogeneous electric fields to split beams of electrons [31] and ground state polar molecules [30, 32]; their designs can be seen in Figure 2.13. The molecular beam splitter demonstrated by Gordon and Osterwalder [Figure 2.13(a)] was a three-dimensional configuration of electrodes made by 3D printing and electroplating, while the beam splitters for electrons [Figure 2.13(b)] and molecules [Figure 2.13(c)] developed by Hammer et al. [31] and Deng et al. [32], respectively, were both chip-based and composed of two-dimensional electrode structures. The electron beam splitter consisted of three long electrodes that gradually changed shape along with position and were surrounded by ground planes, whereas the molecular beam splitter was made by embedding a Y-shaped wire in an insulating substrate. Both of these designs generated electric fields in a distribution that transformed from a quadrupole to a hexapole with increasing longitudinal position thus splitting the particle beams

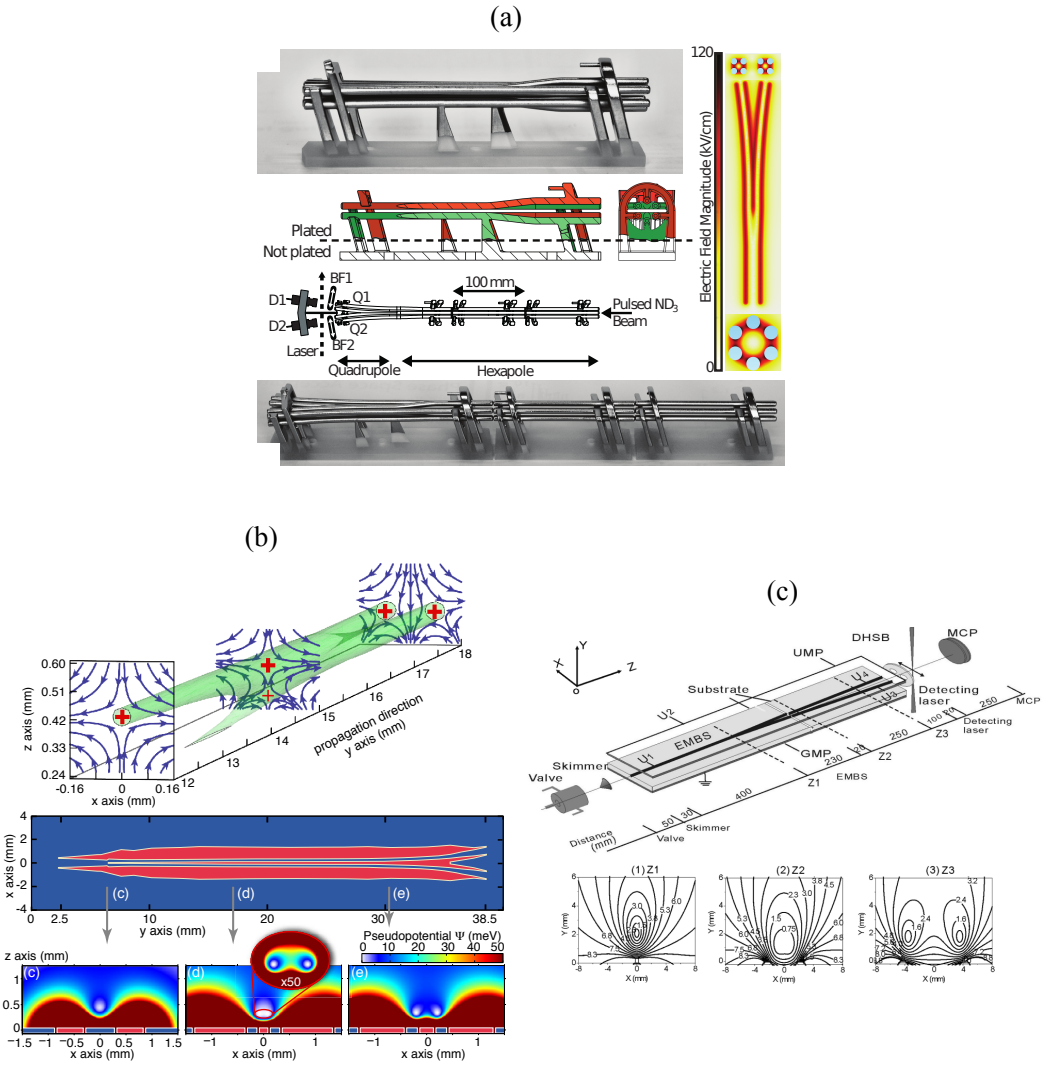

Figure 2.13: (a) 3D printed molecular beam splitter. Chip-based beam splitters for (b) electrons and (c) polar ground state molecules. From References [30, 31, 32].

transversally into two spatially separated components. The Rydberg atom beam splitter described in Chapter 4 of this thesis complements these other electric beam splitter for electrons and polar ground-state molecules.

Chapter 3

Experimental methods

The experiments presented in the following chapters, while each slightly different in nature, have much of their experimental setup and methods in common, namely the production of pulsed supersonic beams of metastable He, the photoexcitation of these atoms to Rydberg states and the detection of the Rydberg states by pulsed electric field ionisation. For the sake of brevity, these common elements are described in this chapter while the specific elements unique to each individual experiment are then presented in the relevant chapters.

As can be seen in Figure 3.1, all of the experiments reported here were performed in an apparatus composed of two connected vacuum chambers: the source chamber and the experiment chamber, operated at pressures of approximately 10^{-7} and 10^{-8} mbar, respectively.

3.1 Pulsed supersonic beams of metastable helium atoms

Pulsed supersonic beams of helium atoms in the metastable 1s2s $^3S_1$ level (lifetime $\sim$ 7870 s [34]) were generated at the exit of a valve connected to a reservoir of He gas, maintained at a pressure of 5 bar. Upon pulsing the opening of the valve,

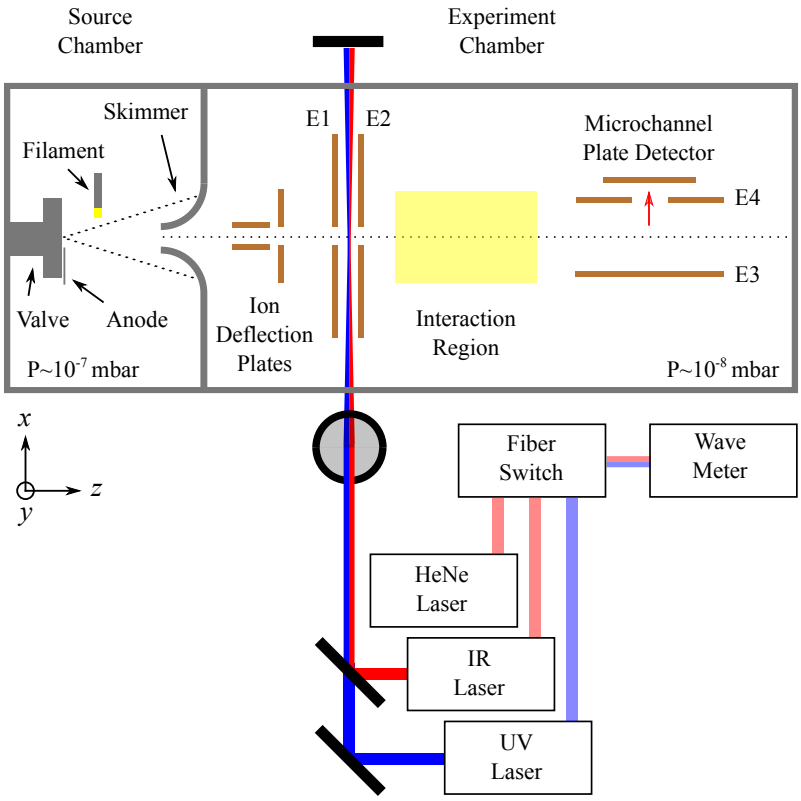

Figure 3.1: Schematic diagram (not to scale) of the general apparatus used in the experiments presented here showing the source chamber where the pulsed supersonic beam of metastable He was generated, the experiment chamber where the atoms were photoexcited, manipulated and detected and the laser system used for photoexcitation. The typical distance between the exit of the pulsed valve and the location of ionisation of the atoms in the experiments described here was ~0.5 m. The y dimension is the vertical dimension in the laboratory frame-of-reference.

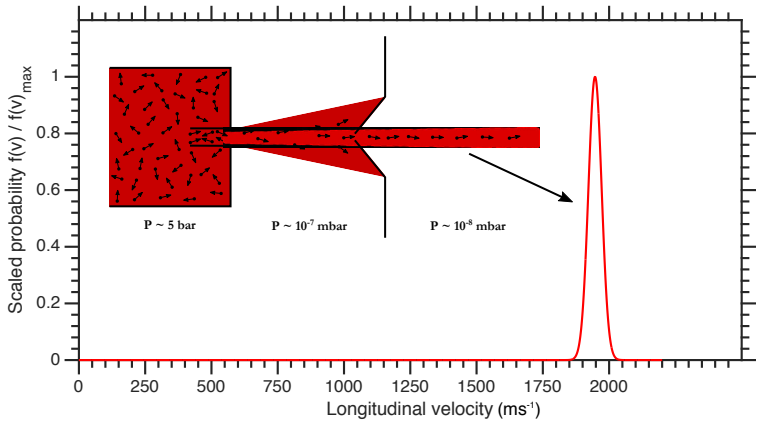

Figure 3.2: Schematic diagram of the production of a supersonic beam and a typical longitudinal velocity distribution of a supersonic He beam emanating from a source operated at 365 K. From Reference [33]

adiabatic expansion of the high pressure He gas into the vacuum chamber led to the creation of a high velocity (typically 1900-2000 $\mathrm{m{\cdot}s^{-1}}$ depending on the operating temperature of the valve) supersonic beam with low velocity spread ($\sim \pm 100\ \mathrm{m{\cdot}s^{-1}}$).

To populate the metastable $1s2s\,{}^3S_1$ level used as the ground state in these experiments a discharge was struck at the exit of the pulsed valve between an anode situated $\sim$ 1 mm from the grounded baseplate of the valve, which acted as a cathode. A voltage of +255 V was applied to the anode and the discharge was seeded by electrons produced by a heated tungsten filament $\sim$ 15 mm downstream from the exit of the valve. Collisions and the recombination of the plasma caused by the discharge populated the metastable $1s2s\,{}^3S_1$ level.

This beam then passed through a skimmer to select the densest, coldest portion of the beam. A schematic diagram of this process can be seen in Figure 3.2. After travelling through the skimmer, a pair of metal plates were used to generate a strong static electric field ($\sim 200\ \mathrm{V{\cdot}cm^{-1}}$) transverse to the direction of propagation of the beam to deflect ions that remained from the discharge.

3.2 Photoexcitation to Rydberg states

After passing through the skimmer and ion deflection plates, the atoms entered the excitation region of the apparatus. This region contained two focussed co-propagating continuous-wave laser beams that passed between two metal electrodes, labelled E1 and E2 in Figure 3.1. These electrodes could be used to cancel stray electric fields at the position where the atoms were excited. They could also be used to generate electric fields to lift the level degeneracy and allow the excitation of individual Rydberg-Stark states. Both lasers used were tunable diode lasers that emitted light in the infrared region of the electromagnetic spectrum. To implement the excitation scheme one of these lasers was frequency doubled to produce light in the ultraviolet region. Tuning this ultraviolet radiation to a wavelength of 388.9751 nm and the second, infrared, laser over the range of wavelengths from 787.902 – 786.433 nm allowed Rydberg-Stark individual states with $45 \leq n \leq 60$ to be prepared using the $1s2s\,^3S_1 \rightarrow 1s3p\,^3P_2 \rightarrow 1sns/1snd$ two-colour two-photon excitation scheme as shown in Figure 3.3. The wavelengths of these lasers were stabilised using a wavemeter that was calibrated to a HeNe laser, both shown in Figure 3.1. Since these lasers operated continuously, electric field pulses were generally used in the experiments to bring the transition to a selected Rydberg-Stark state into resonance and excite only selected portions of the supersonic beams. The phase-space properties of the excited cloud of Rydberg atoms were defined by the full-width-at-half-maximum waists of the laser beams and the duration of the excitation electric field pulses and typically resulted in a cylindrically shaped ensemble of Rydberg atoms with sizes of 0.1, 0.1 and 5 mm and relative translational temperatures on the order of 1, 1 and 500 mK in the x, y and z dimensions, respectively.

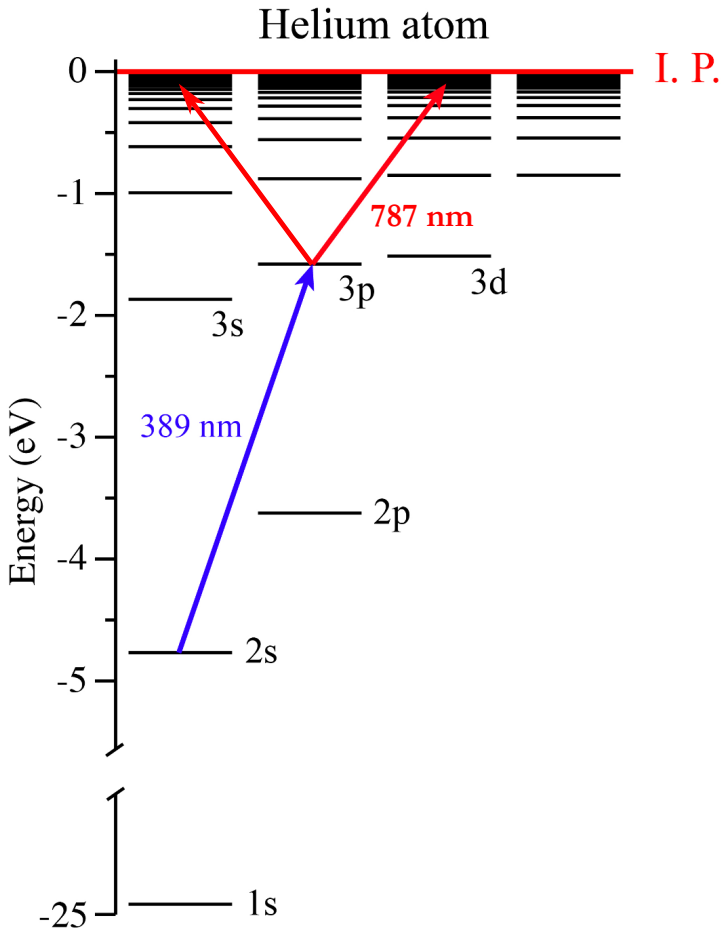

Figure 3.3: Energy level structure of the triplet states in He showing the excitation scheme used to populate high-n Rydberg states. From Reference [33]

3.3 Circular state preparation

Although several of the experiments reported here required the direct laser photoexcitation of low angular momentum Rydberg states, the Rydberg-atom interferometry studies necessitated the preparation of circular Rydberg states for which $|n\mathrm{c}\rangle = |n, \ell = n-1, m_\ell = n-1\rangle$. These states possess large electric dipole transition moments for $|\Delta n| = 1$ transitions and allow for strong transitions between them. They also have a low sensitivity to weak stray electric fields and electric field noise which minimises decoherence when prepared in superpositions with each other. The population of these states directly by laser photoexcitation from the $1s3p\,^3P_2$ level is limited by the selection rule that $|\Delta m_\ell| = 1$ and therefore they cannot be directly photoexcited. Presently, two methods exist for the preparation of circular Rydberg states: the adiabatic microwave transfer method, in which a chirped microwave field incrementally increases the value of $|m_\ell|$ until the maximum value is reached [35]; and the crossed fields method [36], in which a combination of magnetic and time-dependent electric fields is used to transform states with low-ℓ character at the time of excitation into circular states.

In this crossed fields method, employed in the work described here, a weak magnetic field is used to lift the degeneracy of the Rydberg states and a perpendicular electric field then provides the selected circular state, $|\mathrm{c}\rangle$, with low-$|m_\ell|$ character due to the mixing it induces. These fields cause $|\mathrm{c}\rangle$ to evolve into the outermost stark state, $|\mathrm{c'}\rangle$, in a strong electric field, as shown in Figure 3.4(a) for the $n = 55$ circular state in He. From Figure 3.4(b) it can be seen that near the Inglis-Teller limit, the electric field for which the energy levels of an atom with principle quantum number n first cross those of an atom with principle quantum number $n + 1$, where $|\mathrm{c'}\rangle$ undergoes an avoided crossing with the $|56\mathrm{s'}\rangle$ state it gains enough $|m_\ell| = 0$ character to be directly photoexcited using the scheme presented in Section 3.1. Following excitation at this position in the Stark map, the pure circular state, $|\mathrm{c}\rangle$, is populated

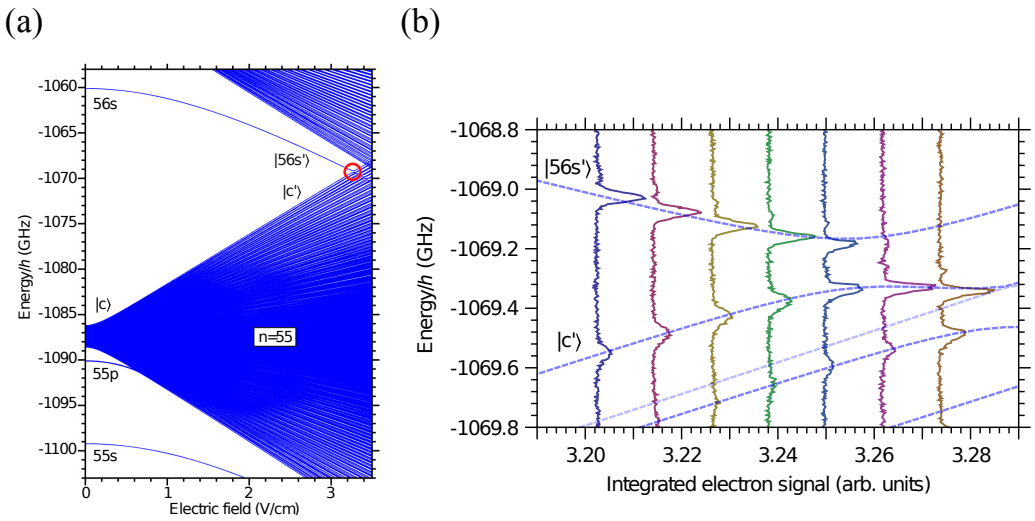

Figure 3.4: (a) Energy level structure of the $n = 55$ and surrounding triplet Rydberg states in He in a weak magnetic field (B_z = 15.776 G) and a perpendicular electric fields showing the evolution of the circular state |c⟩ in the pure magnetic field into |c′⟩. (b) Energy level structure of the |c′⟩ and |56s⟩ states near the -Teller limit where they undergo an avoided crossing. Experimentally recorded photoexcitation spectra are overlaid with the calculated energy level structure in (b) showing an enhancement in the strength of the transition to the |c′⟩ state in fields just beyond the avoided crossing. Adapted from Reference [36].

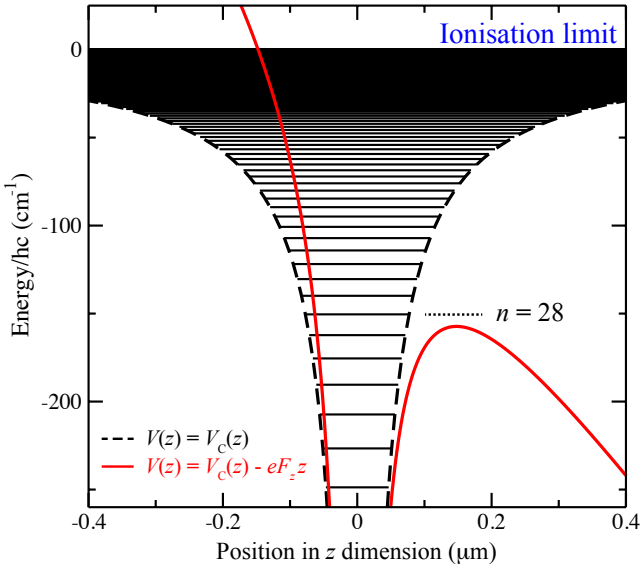

Figure 3.5: The Rydberg states of the hydrogen atom in a pure Coulomb potential, $V_C(z)$, (dashed black curve) beginning at n = 22. The potential resulting from the addition of a strong electric $\vec{F} = (0, 0, F_z)$ is indicated by the solid red curve. From Reference [37].

adiabatically by slowly switching off the electric field.

3.4 Atom detection by pulsed electric field ionisation

In a static electric field the Coulomb potential experienced by an electron in an atom is distorted and a saddle point is created on one side. This effect is shown in Figure 3.5 for hydrogen. This allows the electron to tunnel through the resulting barrier and ionise. Since electrons can only tunnel out in one direction, for atoms in Rydberg-Stark states the localisation of the excited electron with respect to the ion (as defined by the orientation of the electric field) leads to different ionisation rates for different states. This is because an electronic wavefunction localised on the opposite side of the ion to the saddle point must attain amplitude close to the

barrier in the distorted Coulomb potential before it ionises. States with negative Stark energy shifts (LFS states) have greater electron localisation on the side of the ion closest to the saddle point and therefore have higher tunnelling rates in any given field than states with positive Stark energy shifts (HFS states) where more of the electron density is on the opposite side of the ion. In practical terms, if an electric field is pulsed on for a duration of 10 ns to ionise an atom then an ionisation rate of $\sim 10^8$ s^{-1} is required for complete ionisation of a particular state. For each Rydberg-Stark state this ionisation rate is achieved at a different field strength with the outer HFS state requiring a field approximately twice as large as the outer LFS state requires [38]. The classical ionisation field of the outermost HFS state for each value of n, accounting for the stark shift is [39]

$$F_{\text{class}} = \frac{F_0}{9n^4}, \tag{3.1}$$

where $F_0 = 2hR_M/ea_0$ is the atomic unit of electric field. The energy shifts of the Stark states with $n = 10$ and $m = 0$ in hydrogen are displayed in Figure 3.6 as a function of electric field strength. For each state, the curves presented have been truncated at the field in which the ionisation rate exceeds 10^8 s^{-1}.

As can be seen in Figure 3.1, the detection region of the experimental setup used in the work described here consisted of two metal electrodes, E3 and E4, and an MCP detector. Upon application of a large potential to E3, with E4 grounded, Rydberg atoms located between these plates were ionised and the resulting ions or electrons (dependent on the polarity of the ionisation potential) were accelerated through the aperture in E3 to the MCP for collection. This setup has been used in the following experiments to realise two different detection schemes. When all atoms to be detected were in the same state and only the total population of Rydberg states at a particular time was of interest an ionisation pulse with a short rise time ($\sim$ 30 ns) was used to ionise all Rydberg atoms present at the same time. Using this scheme, if low ionisation fields were employed and He^+ ions were detected, the

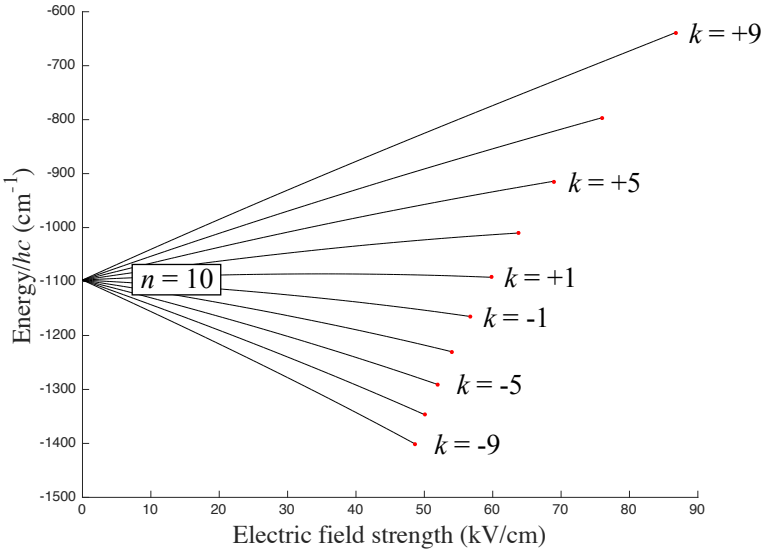

Figure 3.6: Electric-field-dependent energies of the $n = 10,\ m = 0$ Rydberg-Stark states for hydrogen truncated at a field for each state that results in an ionisation rate of 10^8 s^{-1}.

ion time-of-flight distributions measured at the MCP contained information on the spatial distribution of the atoms in the x-dimension at the time of ionisation which could be resolved (as in Chapter 4). Since different Rydberg states ionise in electric fields of different strengths, Rydberg-state-selective detection was also exploited in a second mode of operation by applying a slowly rising ionisation potential (rising to its maximum value over a time of ~ 1 μs). In this situation, individual Rydberg states were identified as the ionised electrons associated with each appeared at a different time in the MCP signal. More detail on the calibration and implementation of this quantum-state-selective detection scheme is provided in Chapter 5.

Chapter 4

A Rydberg-atom beam splitter

The scientific content of this chapter has been published in

- J. Palmer and S. D. Hogan, “Experimental demonstration of a Rydberg-atom beam splitter", *Phys. Rev. A* **95**, 053413 (2017).

However, the text drawn from this article has been adapted to fit within the context of this thesis.

4.1 Introduction

The methods of Rydberg-Stark deceleration described in Chapter 2 have been employed, e.g., to study effects of blackbody radiation on the evolution of Rydberg-Stark states on time scales up to several milliseconds [24, 40], to characterise effects of collision-induced m-changing arising from dipole-dipole interactions in ensembles of Rydberg atoms [41], to identify classes of long-lived molecular Rydberg states which are immune from fast pre-dissociation [42, 43], to study ion-molecule reactions at low collision energies in merged beams [44, 45], and to exert control over the translational motion of neutral beams of Ps atoms [15]. However, a range of new experiments are now under development [2] in which these Rydberg atom

optics elements will be exploited for studies of molecular collisions and decay processes [46], for transport and confinement in hybrid approaches to quantum information processing [47], and for investigations of the acceleration of particles composed of antimatter in the gravitational field of Earth using Ps [48] and antihydrogen [49] atoms. In several of these areas, methods for splitting beams of Rydberg atoms into spatially separated components promise to be of great value, (1) for the distribution of samples among spatially separated interaction regions, (2) for reference intensity measurements in collision experiments, and (3) if prepared at sufficiently low translational temperatures, for interferometry.

With applications of this kind in mind, the design and first experimental realisation of a chip-based Rydberg atom beam splitter is described here. The operation of this device relies upon the generation of tailored inhomogeneous electric field distributions above two-dimensional arrays of metallic electrodes to guide and then transversely split beams of Rydberg atoms in states with large electric dipole moments into pairs of components. This device complements recently developed chip-based electron beam splitters [31], and beam splitters for polar ground state molecules composed of two-dimensional chip-based [32], and three dimensional electrode structures [30] as discussed in Chapter 2. The chip-based design of this device is particularly flexible and can be readily integrated with Rydberg-Stark decelerators, traps and microwave circuits.

4.2 Beam splitter

A schematic diagram of the chip-based Rydberg atom beam splitter used in the experiments presented here is shown in Figure 4.1(a). The design of this device is based on the geometry of a coplanar microwave transmission line allowing it to be integrated with two-dimensional microwave circuits [8] and transmission-line guides [27], decelerators [28] and traps [29] for Rydberg atoms and molecules. The

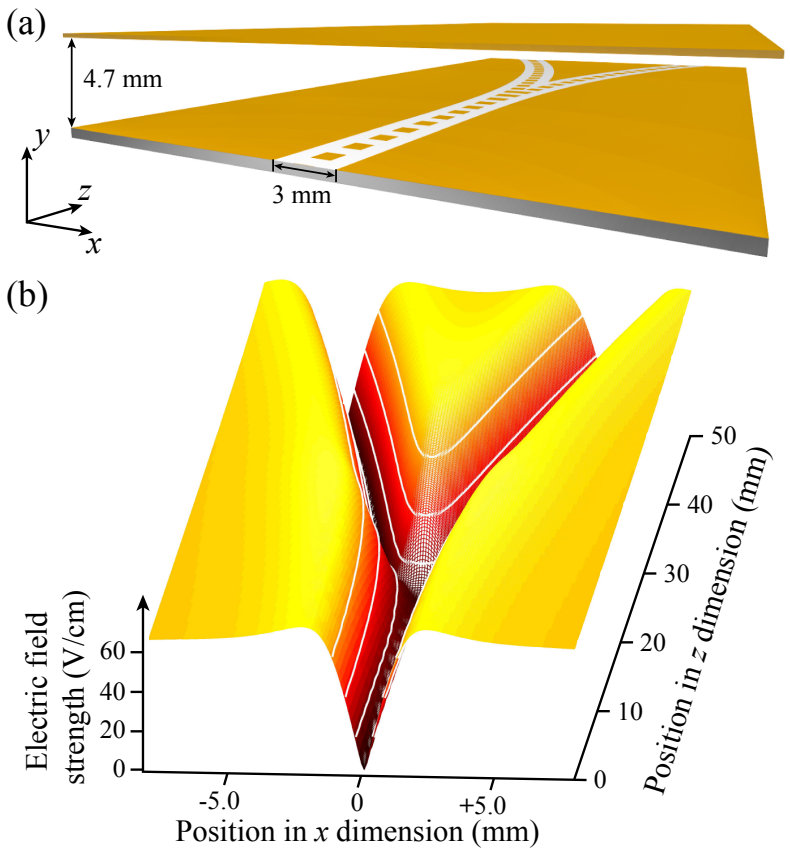

Figure 4.1: (a) Schematic diagram of a chip-based Rydberg atom beam splitter. (b) Electric field distribution in the xz plane of the beam splitter at y = 1.4 mm for V_g = 30 V (see text for details). The electric field strength indicated by the white contour lines is displayed in intervals of 20 V·cm^{-1}. These contour lines correspond to potential energies in intervals of 5.80×10^{-23} J ≡ 2.92 cm^{-1} for an atom with an electric dipole moment of 8700 D.

beam splitter consists of a 90-mm-long two-dimensional electrode array composed of a series of 1 mm × 1 mm square electrodes with a centre-to-centre separation of 2 mm. A 1-mm-gap on either side of these electrodes separates them from the adjacent ground planes. An upper plate electrode is positioned 4.7 mm above this array. The split section of the electrode array is formed by the intersection of the arcs of two circles with radii of curvature of 0.3 m. The device was fabricated by chemically etching a layer of copper from on top of an FR-4 laminate substrate.

In the experiments the beam splitter was operated in an electrostatic mode. For a potential V_g applied to each electrode of the segmented centre conductor of the transmission-line and the upper plate electrode, a two-dimensional quadrupole electric field distribution was generated in the xy plane above the individual arms of the device [see Figure 4.1(a) for a definition of the coordinate system]. This quadrupole field acted as a guide for atoms in LFS Rydberg-Stark states with positive Stark energy shifts. As can be seen in Figure 4.1(a), the guide gradually splits into two spatially separated components with increasing longitudinal position above the electrode array reflecting the change in structure of the centre conductor electrodes. The calculated electric field distribution at a height of y = 1.4 mm above the surface of the electrode array and in the region where the paths diverge for V_g = 30 V is displayed in Figure 4.1(b). This position in the y dimension represents the typical location of the electric field minimum above the electrode array in the initial straight section of the beam splitter. The minimum rises slightly, by ~300 μm, in the region where the centre-conductor electrodes widen before splitting. The spatial separation in the x dimension of the two arms of the beam splitter at the end of the device is 13 mm. For the Rydberg-Stark states prepared in the experiments with electric dipole moments of μ_{elec} = 8700 D, the depth of the guide when V_g = 30 V was $E = 2{\times}10^{-22}$ J ($E/k_B \simeq 15$ K).

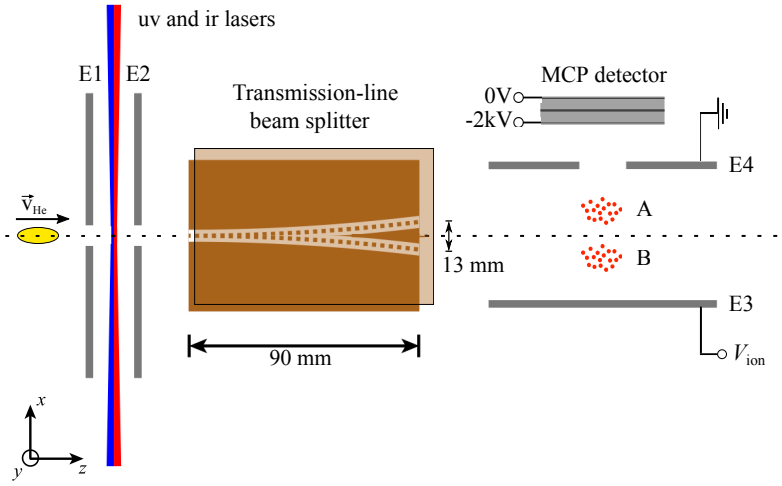

Figure 4.2: Schematic diagram of the experimental setup used in the realisation of a chip-based Rydberg-atom beam splitter (not to scale). Rydberg state photoexcitation occurred between electrodes E1 and E2. The excited Rydberg atoms were detected by pulsed electric field ionisation upon the application of a potential $V_{\rm ion}$ = +500 V to E3 with the resulting He^+ ions accelerated through an aperture in E4 to the MCP detector.

4.3 Experiment

The location of the beam splitter within the experimental apparatus can be seen in Figure 4.2. For this experiment the pulsed valve was cooled using liquid nitrogen resulting in a typical mean longitudinal velocity of the atomic beam of $\overline{v}_{\rm He} \simeq 1700$ m·s^{-1}. As described in Chapter 3, He atoms were photoexcited to Rydberg states with n=52. The excitation occurred in the presence of a homogeneous electric field of 0.47 V·cm^{-1} generated by applying potentials of +500 mV and -40 mV to E1 and E2 in Figure 4.2, respectively. This allowed the preparation of selected hydrogenic Rydberg-Stark states with $|m_\ell| = 2$. After excitation the atoms passed through an aperture in E2 and entered the beam splitter which was operated at a potential $V_{\rm g}$. After travelling the length of the device, the atoms

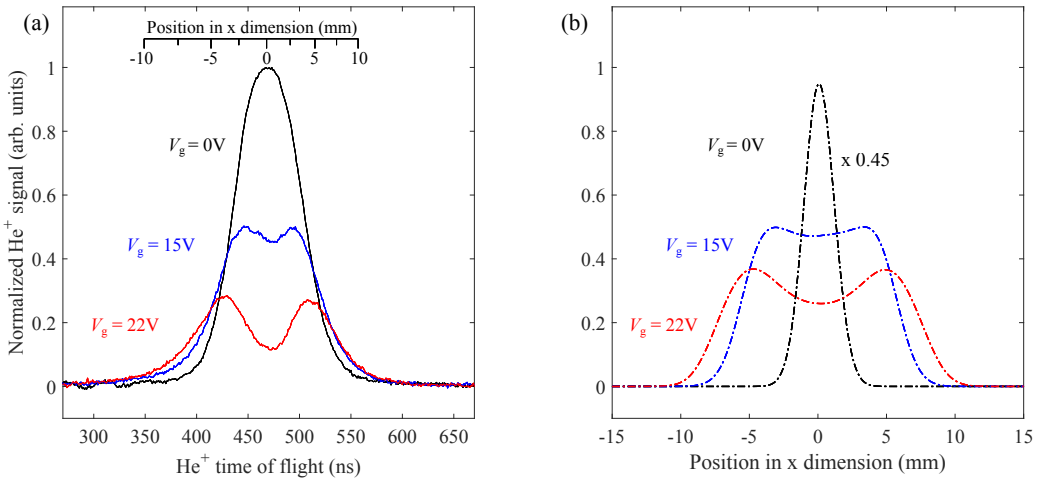

Figure 4.3: (a) He^+ time of flight distributions recorded following pulsed electric field ionisation in the detection region of the apparatus when V_g = 0 V (black curve), 15 V (blue curve) and 22 V (red curve) as indicated. The inset axis shows the calculated relative positions of the atoms in the x dimension at the time of ionisation. (b) Calculated spatial distributions of Rydberg atoms in the x dimension in the detection region at the time of ionisation. The data for V_g = 0 V (dashed black curve) have been scaled by a factor of 0.45 as indicated.

were detected by pulsed electric field ionization upon the application of a pulsed potential V_{ion} = +500 V to the metallic plate labelled E3 in Figure 4.2. The resulting He^+ ions were then accelerated toward an MCP detector. By measuring the time between the application of the ionisation potential and the arrival of the He^+ ions at the MCP, the distribution of atoms in the x dimension at the time of ionisation could be spatially resolved.

4.4 Results

With the beam splitter turned off, i.e., when V_g = 0 V, the trajectories of the atoms were unaffected as they travelled to the detection region along the axis of the

apparatus (dashed horizontal line in Figure 4.2). After ionisation the He^+ ions arrived at the MCP with a mean time of flight of ~475 ns. The corresponding He^+ time-of-flight distribution is displayed in Figure 4.3(a) (black curve). When the beam splitter was activated the inhomogeneous electric field distribution split the beam of atoms into two separated components labelled A and B in Figure 4.2. Upon ionisation the He^+ ions associated with component A had a reduced time of flight to the MCP while those associated with component B had an increased time of flight compared to the undisturbed beam. For the Rydberg-Stark states prepared in the experiments these two spatially separated components of the beam caused a broadening of the He^+ time-of-flight distribution for potentials of $V_g \gtrsim 10$ V. This can also be seen in the data in Figure 4.3(a). When operated at $V_g = 22$ V almost complete separation of the two split components of the beam is seen with peaks in the He^+ time-of-flight distribution at ~425 ns and ~525 ns.

The spatial separation of the split components of the Rydberg atom beam in Figure 4.3(a) was determined by comparing the relative flight times of the corresponding He^+ ions to the MCP detector with numerical calculations of the dependence of the He^+ time of flight on the position of ionisation of the Rydberg atoms. This comparison resulted in the position scale included in the top part of Figure 4.3(a) which indicates a separation of 8.5 mm between the two split components of the beam when $V_g = 22$ V. Under these conditions, the atoms remain displaced from the axis of each arm of the beam splitter when they reach the end of the device. The atoms also have some velocity in the x dimension, meaning that the measured separation at the detection region does not directly reflect their separation at the exit of the beam splitter.

4.5 Particle trajectory calculations

To obtain further insight into the Rydberg atom trajectories from their time of photoexcitation to the time of electric field ionisation at the end of the beam splitter, numerical simulations of particle trajectories through the complete apparatus were performed.

In these calculations, atoms were individually initialised at the valve location with a normal distribution of temperatures in the x, y and z dimensions, i.e., $\sigma_{v_x} = \sqrt{2kT_x/\mathrm{m}}$, with a mean speed of 1700 m·s^{-1} in the z direction, and their flight simulated over the 155 mm distance of travel to the excitation region (mean flight time $\sim$ 91 μs). The atoms were then assessed to determine if they were within the required spatial distribution, defined by the parameters of the photoexcitation laser beams to be 0.4 and 0.1 mm full-width-at-half-maximum in the x and y dimensions, respectively, with a length of 6 mm in the z dimension. This process was repeated until an ensemble of 100,000 excited atoms had been generated. The corresponding relative translational temperatures of the atoms after excitation were 1.7, 0.7 and 78 mK in the x, y and z dimensions, respectively.

A set of three dimensional arrays that contained the x, y and z components of the normalised electric field vector with 1 V applied to each electrode and all of the others set to 0 V were generated using SIMION. For each point in the arrays between the excitation and detection regions (labelled with the indices i, j and k) the total electric field was given at any time by

$$\vec{F}_{i,j,k}(t) = \left(\sum_I V_I(t) F_{ijkx}, \sum_I V_I(t) F_{ijky}, \sum_I V_I(t) F_{ijkz} \right), \tag{4.1}$$

where I is the electrode index, $V_I(t)$ is the potential applied to that electrode at that time and F_{ijkx}, F_{ijky} and F_{ijkz} are the x, y and z components of the normalised field vector at that point associated with electrode, I, respectively. This allowed for the effects of time-dependent fields on the trajectories of the atoms to be simulated.

These were then calculated in time steps of 1 ns. At each time step the electric field gradient at the location of each atom was calculated by interpolating between the three nearest points in each of the x, y and z dimensions of the electric field array. The force on each atom was calculated according to

$$\vec{f} = \nabla(\vec{\mu}_{\text{elec}} \cdot \vec{F}) \tag{4.2}$$

and Newton's equations of motion were integrated using the leap frog method to determine the new velocity of that atom. This was repeated until the atoms reached the detection region where their x, y and z positions were recorded. These were used to obtain the distributions in Figure 4.3(b).

The results of these simulations for V_g = 0, 15 and 22 V are displayed in Figure 4.3(b). For ease of comparison with the data in Figure 4.3(a) the calculated spatial distribution for V_g = 0 V in Figure 4.3(b) has been scaled by 0.45. The calculated spatial distributions of Rydberg atoms in the detection region of the apparatus show a similar dependence on V_g to the experimental data with a clear separation between the two split components of the beam when $V_g \gtrsim 15$ V. From the results of these simulations, the reduction in signal with increasing values of V_g observed in the experimental data in Figure 4.3(a) was identified to originate from vertical deflection of the beam of atoms into the y dimension. The differences in the relative amplitudes of the experimentally measured He^+ time-of-flight distributions and calculated data are attributed to the effects of state-changing collisions with background gas emanating from the beam-splitter substrate [29]. These collisions do not strongly affect the signal amplitude when the beam splitter is inactive but contribute to the loss of atoms when $V_g > 0$ V. The difference in the relative widths of the experimental and calculated data, particularly when V_g = 0 V, are the result of saturation of the MCP response under these conditions.

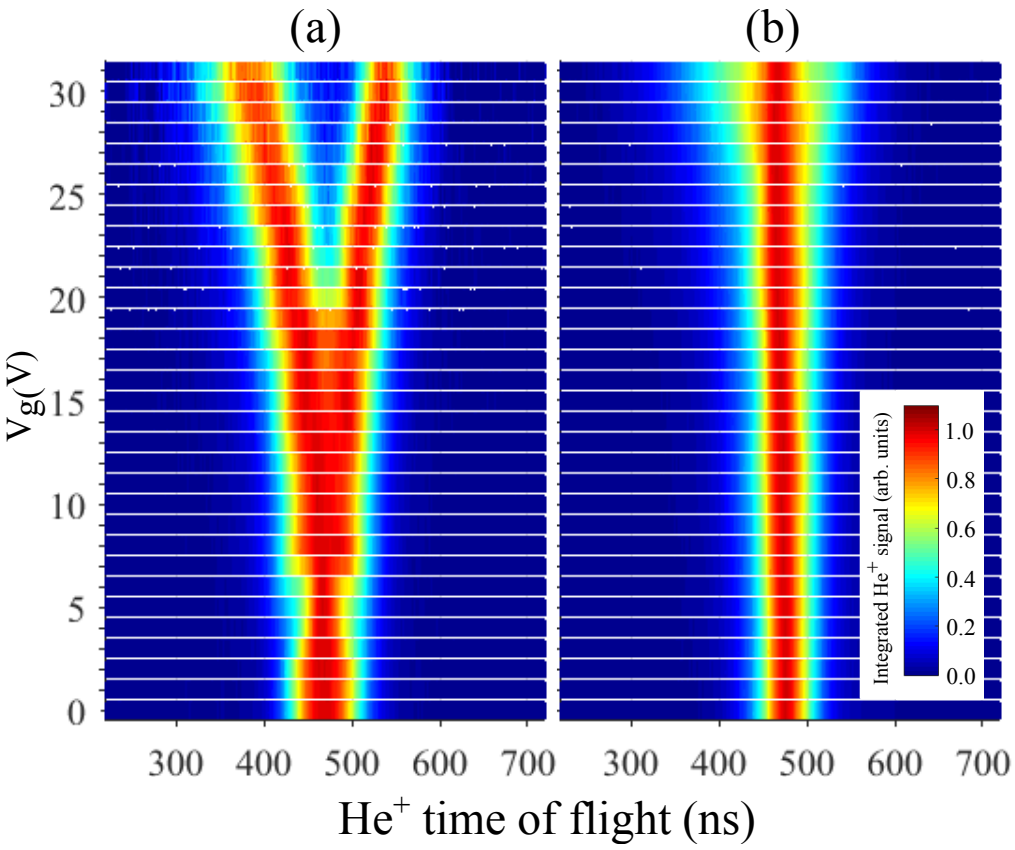

Figure 4.4: Normalised He^+ time of flight distributions for a range of beam-splitter operating potentials, V_g, for (a) an LFS Rydberg-Stark state with μ_{elec} = 8700 D, and (b) a centre Stark state with $\mu_{elec} \simeq 0$ D. The colour scale in (b) is common to both panels.

4.6 Beam splitter characterisation

To fully characterise the operation of the beam splitter, further measurements were made for a range of operating potentials, V_g. The results of these are shown in Figure 4.4(a) with the intensity maximum in each data set normalised to unity. For low potentials, i.e., when 0 V $\leq V_g \leq$ 7 V, the He^+ time-of-flight distributions are seen to gradually narrow as V_g increases. This indicates that under these conditions the initial straight section of the guide acts as a quadrupole lens that transversely

focuses the atoms to the detection region. For higher potentials, i.e., $V_g > 8$ V, the time-of-flight distributions broaden and begin to split into two components. A clear spatially resolved splitting is seen when $V_g > 20$ V. For the largest potential applied, $V_g = 31$ V, the splitting in the time-of-flight distribution corresponds to a spatial separation of the two components of the beam in the x direction at the time of ionisation of 15.6 mm. The slight asymmetry of the split components of the beam arises because the ion flight times are not directly proportional to the position of the atoms in the x dimension at the time of ionisation (see axis inset in Figure 4.3).

To demonstrate that the beam splitter only operates to split beams of atoms in LFS Rydberg-Stark states the measurements were repeated following photoexcitation of states in the centre of the Stark manifold with n=52 and electric dipole moments of $\mu_{\text{elec}} \simeq 0$ D. The resulting data are displayed in Figure 4.4(b). It can be seen from these measurements that the atoms in these states are generally unaffected by the electric fields of the beam splitter. However, when operated at high potentials, e.g., $V_g > 20$ V, a small amount of broadening in the He^+ time-of-flight distributions is observed. This broadening is attributed to deflection of atoms pumped into Stark states with non-zero static electric dipole moments by blackbody radiation during their ~45 μs flight through the device.

4.7 Particle losses

The sensitivity of the beam splitter to changes in the electric dipole moments of the atoms during their trajectories through the device, as seen in Figure 4.4(b), can be further exploited to identify processes that contribute to state-changing in this and other Rydberg atom optics elements. In particular this sensitivity can be used to investigate the effects of modulation of the electric fields of the beam splitter by periodic driving or laboratory noise on the evolution of the trapped or guided atoms. To observe these effects the atoms were prepared in the outer

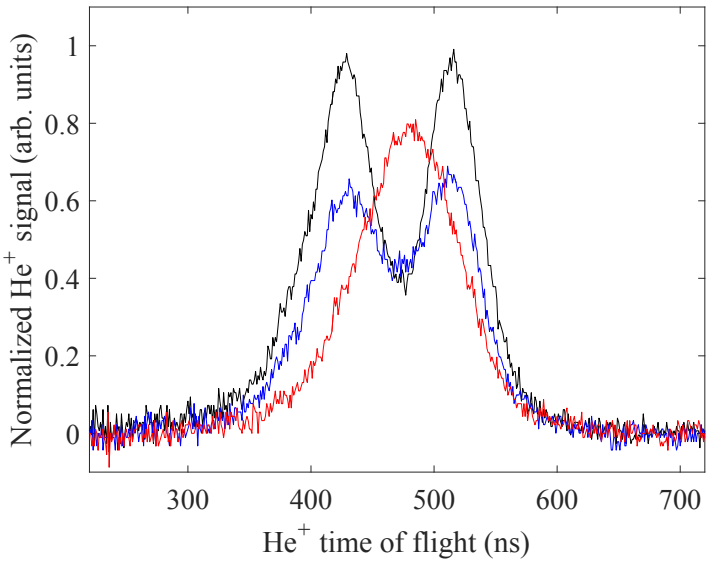

Figure 4.5: He^+ time of flight distributions for V_g = 20 V with no amplitude modulation (black curve) and with modulations of V_{mod}^{pp} = 56 and 280 mV (blue and red curves, respectively) at 100 MHz .

LFS Rydberg-Stark state and the beam splitter was operated at a potential of V_g = 20 V. A small amplitude modulation was applied to this potential at a frequency of 100 MHz. The effect of this modulation with peak-to-peak amplitudes in the range from V_{mod}^{pp} = 0 - 280 mV on the He^+ time-of-flight distributions can be seen in Figure 4.5. For these measurements $\overline{v}_{He}$ = 2000 m·s^{-1} and the centre black set of data was recorded with V_{mod}^{pp} = 0 V as indicated. When V_{mod}^{pp} was increased to 56 mV (blue data set), the amplitude of the signal from the split components of the beam reduced. This observation suggests that the modulation of the depth of the guide leads to heating of the atoms or state-changing into Stark states with lower electric dipole moments that are less affected by the inhomogeneous electric field. This effect becomes more exaggerated when V_{mod}^{pp} is increased to 280 mV. The introduction of similar modulations to the electric potentials in the particle trajectory simulations, to account for their effect on the Rydberg atom dynamics but not state-changing, indicated no change in the efficiency of the beam splitter. This suggests that the dominant loss mechanism associated with modulating the beam-splitter potentials is state-changing collisions, which transfer population into Stark states with dipole moments that are less favourable for guiding. In the absence of this imposed modulation of V_g, electrical laboratory noise [50, 51] can also have a similar detrimental effect on the efficiency with which this and other Rydberg atom optics elements are operated. Such noise must also be considered in accounting for contributions to m-changing which is of importance on longer time scales in these experiments [41]. To see if heating of the atoms was also occurring, an experiment could be performed to image the atom cloud as a function of time after exiting the beam splitter to determine its temperature. This could be combined with an experiment of the type described in Chapter 5 to gain a more complete description of the loss mechanisms.

4.8 Quantisation of motional states

For many applications of Rydberg-atom beam splitters, particularly in interferometry with atoms or molecules, it will be necessary to ensure that the atoms are confined in the lowest motional states of the devices. For the present configuration of electric fields with $V_g = 30$ V and He atoms in states with electric dipole moments of $\mu_{elec} = 8700$ D, within an harmonic approximation the lowest motional states of the guide are separated in energy by $\Delta E_{mot} \simeq 2.18{\times}10^{-28}$ J ($\Delta E_{mot}/k_B \simeq 15$ μK, $\Delta E_{mot}/h \simeq 330$ kHz). This trap frequency can be increased by increasing the electric field gradients in the device by reducing the dimensions of the electrodes, or by applying larger electrical potentials. For an operating potential of $V_g = 5$ kV and the presented electrode configuration the energy separation between the lowest motional states would become $\Delta E_{mot}/k_B \simeq 0.2$ mK ($\Delta E_{mot}/h \simeq 4.3$ MHz). Under these conditions atoms in the lowest motional states (i.e., with motional quantum number less than 10) would experience electric fields of ~ 2 V·cm^{-1}. They therefore would not be affected by electric field ionisation. The transverse temperatures of the Rydberg atoms in the beam used in the experiments reported here was < 1 mK. This would suggest that with larger fields and careful matching of the phase-space properties of the atomic beam to the beam splitter, only the lowest transverse motional states could be populated, offering intriguing new opportunities for Rydberg atom interferometry which could also be exploited in experiments with Ps atoms.

4.9 Conclusion

The beam splitter described here, as well as having applications in hybrid cavity QED experiments with Rydberg atoms and microwave circuits, to distribute atoms among arrays of spatially separated coplanar superconducting microwave resonators, and in allowing reference intensity measurements for low-energy col-

lision studies, represents one route to performing Rydberg-atom interferometry. However, as with other methods of atom interferometry, the requirements to access the necessary quantised motional states are challenging to meet. For this reason an approach to Rydberg-atom interferometry using inhomogeneous electric field pulses in free space has also been pursued as discussed in Chapters 6 and 7.

Chapter 5

Radio-frequency depolarisation of Rydberg-Stark states

5.1 Introduction

In Rydberg-Stark deceleration and trapping experiments, the application of rapidly-switching or continuously time-varying electric fields allows for efficient manipulation of the translational motion of atoms and molecules [2], but can also lead to non-adiabatic evolution of their quantum states [52]. As seen in the Rydberg-atom beam splitter experiment described in Chapter 4, amplitude modulation of the electric fields in the device led to losses of atoms. Similar losses can also occur because of effects of electric field noise. This process of state changing in time-varying fields can occur in the presence of static offset fields and, more significantly, in fields near zero.

To carry out a quantitative investigation of the mechanisms that give rise to the particle losses in these settings, experiments were performed to study the depolarisation of selected hydrogenic $n = 52$ Rydberg-Stark states in He when atoms in these states were subjected to amplitude-modulated electric fields with magnitudes

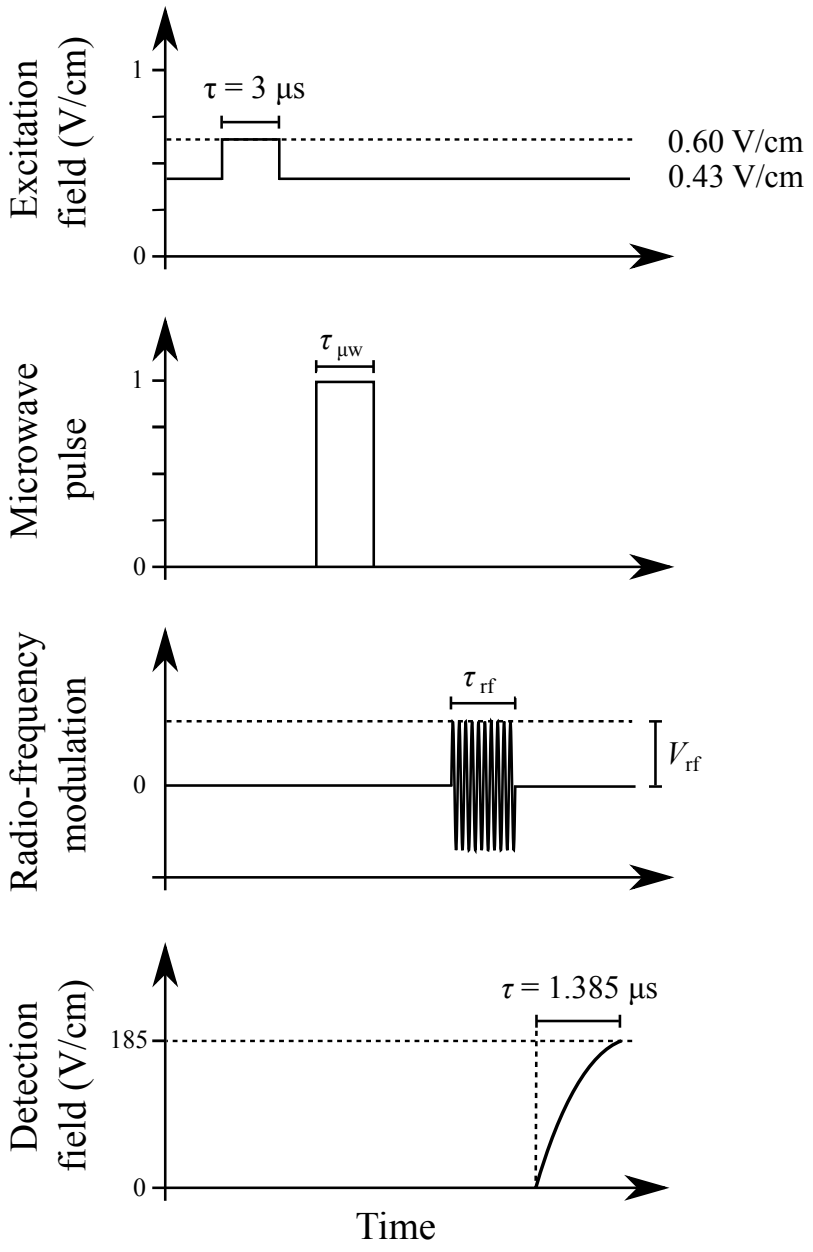

Figure 5.1: Diagram showing the relative timings and amplitudes of the photoexcitation, microwave, rf modulation and detection electric field ionisation pulses used in these experiments. The time axis is not to scale.

of ~10 mV·cm^{-1}, and frequencies of up to 120 MHz. The depolarisation of the initially prepared states in these experiments was monitored as a function of both modulation amplitude and frequency, and was seen to lead to population transfer to a wide range nearby states.

The initial states were prepared using a three-photon optical-optical-microwave triple-resonance method that allowed for the excitation of individual Rydberg-Stark states. This was combined with a state-selective detection scheme using a slowly rising ionisation electric field that allowed for high quantum state resolution of the final state populations. Using the atoms as microscopic antennae, the microwave spectra of transitions between Rydberg states was used to calibrate the frequency dependent attenuation of the radio frequency (rf) modulation field amplitudes, caused by imperfect impedance matching.

5.2 Experiment

To prepare selected Rydberg-Stark states in these experiments, the atoms were first excited to the $|53s'\rangle$ level as described in Chapter 3. As shown in Figure 5.1, this excitation was initiated by switching a homogenous electric field from a background value of 0.43 V·cm^{-1} to 0.60 V·cm^{-1} for $\tau_{ex} = 3$ μs. This field was generated by applying appropriate potentials to two parallel copper plates separated by 1.34 cm. A microwave pulse was then applied with a frequency ranging between 30-34 GHz and pulse lengths of $\tau_{\mu w} = 1 - 3$ μs to prepare selected Rydberg-Stark states with n=52. These transitions occurred in the 0.43 V·cm^{-1} homogeneous electric field. This electric field was then disrupted by introducing amplitude modulations at frequencies, ν_{rf}, between 0 and 120 MHz and amplitudes, V_{rf}, between 0 and 0.5 V to one of the copper electrodes for times of up to $\tau_{rf} = 5$ μs. The resulting rf electric fields in the apparatus were determined to have amplitudes of ~10 mV·cm^{-1} by performing microwave spectroscopy using the Rydberg atoms as microscopic

antennae (see Section 5.3). The atoms were ionised by applying a slowly rising potential up to a final value of 580 V (rise time 1.385 μs) to one of the electrodes, generating fields of up to 420 V·cm^{-1}, with the resulting electrons being accelerated through an aperture to an MCP detector. Figure 5.1 shows the relative timings of the photoexcitation, microwave, rf modulation and detection pulses. Three orthogonal pairs of coils, through which currents were run, were used to cancel the Earth's, and stray, magnetic fields.

Figure 5.2 shows the Stark structure of the triplet Rydberg states in He around n=52 for m=0. The dashed vertical line indicates the background electric field of 0.43 V·cm^{-1} used in the measurements performed here. The initial state for the microwave transition is labelled A.

5.3 RF field calibration

The radio frequency electric fields applied to the excited atoms in the experiments were attenuated by different amounts in transmission from the generator to the interaction region. To calibrate this frequency-dependent field amplitude, the atoms were employed as microscopic antennae. In this process the atoms were prepared in the 55s state in a field of 0.58 V·cm^{-1} by direct laser photoexcitation before the field was switched to 2.99 V·cm^{-1} to induce a large static electric dipole moment of $\sim$ 10000 D. Amplitude modulations were then superimposed on this offset field with a range of frequencies. Microwave spectra of the single photon $|55s'\rangle \rightarrow |56s'\rangle$ transition at 38.351 GHz were then recorded to probe the rf-field-induced sidebands on the modulation-free spectral line. The applied modulation of the electric field results in a set of sidebands on the transition at positive and negative detunings equal to multiples of the modulation frequency. The intensity, I_q, of any sideband,

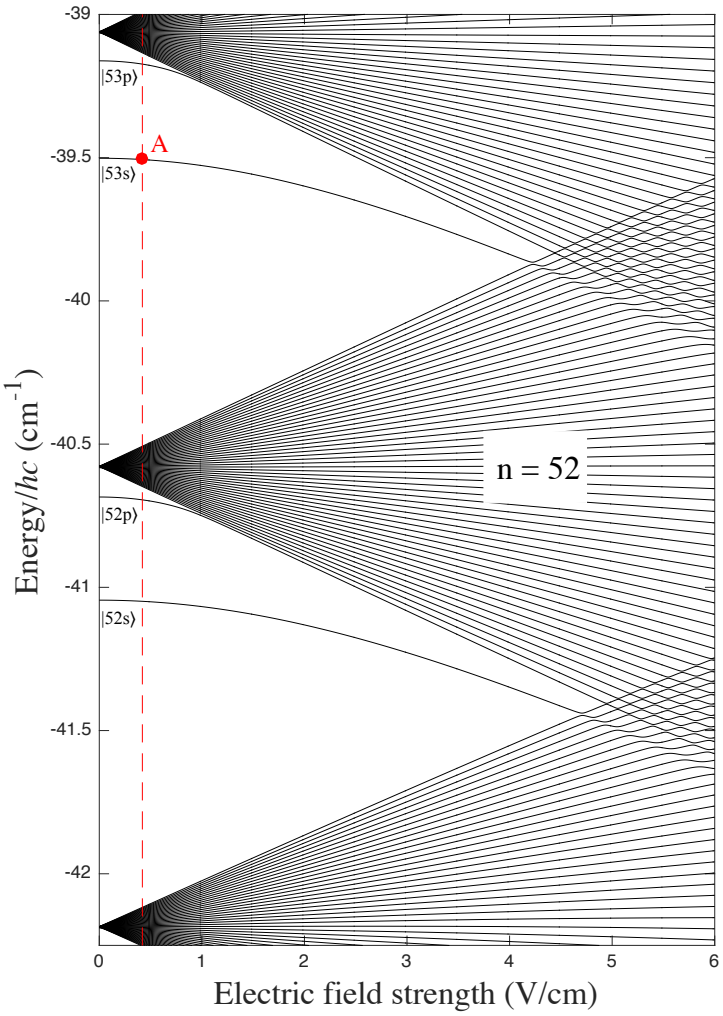

Figure 5.2: Energy level structure of the triplet $n = 52$ Rydberg states in He with $m = 0$ in fields up to 6 V·cm^{-1}. The dashed red vertical line corresponds to the background electric field maintained throughout the experiments while the initial state prepared directly by laser photoexcitation is labelled A.

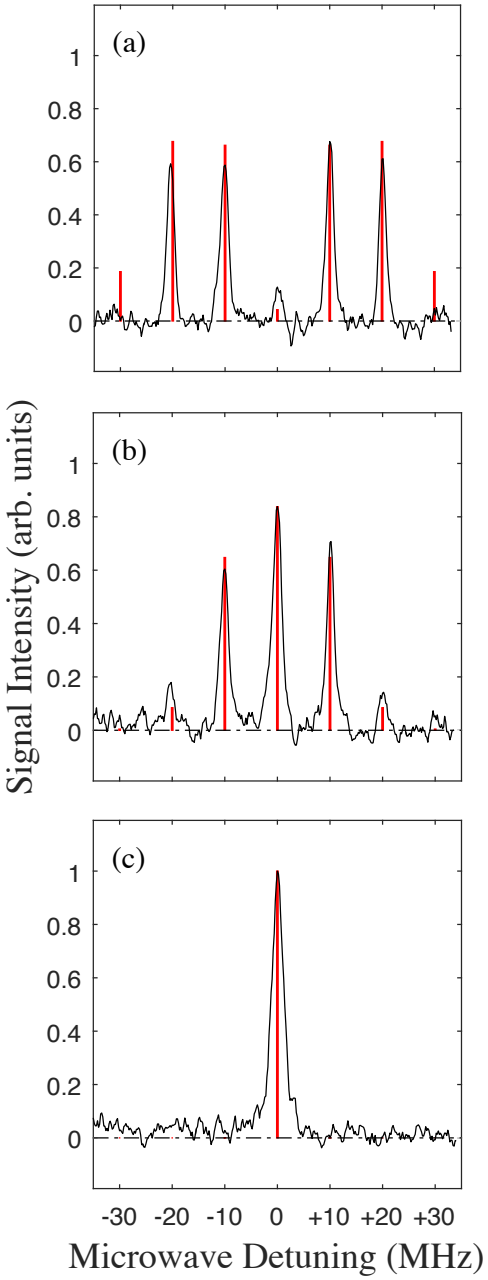

Figure 5.3: Microwave spectra (black curves) of the $|55s'\rangle \rightarrow |56s'\rangle$ transition in an electric field of 2.99 V·cm^{-1} modulated at a frequency of 10 MHz, with modulation amplitudes at the rf source of (a) 101, (b) 56 and (c) 1 mV. The red lines are stick spectra obtained from Eq. 5.1 with electric field amplitudes determined by fitting to the experimental data. The detunings shown are from the resonant transition frequency of 38.351 GHz.

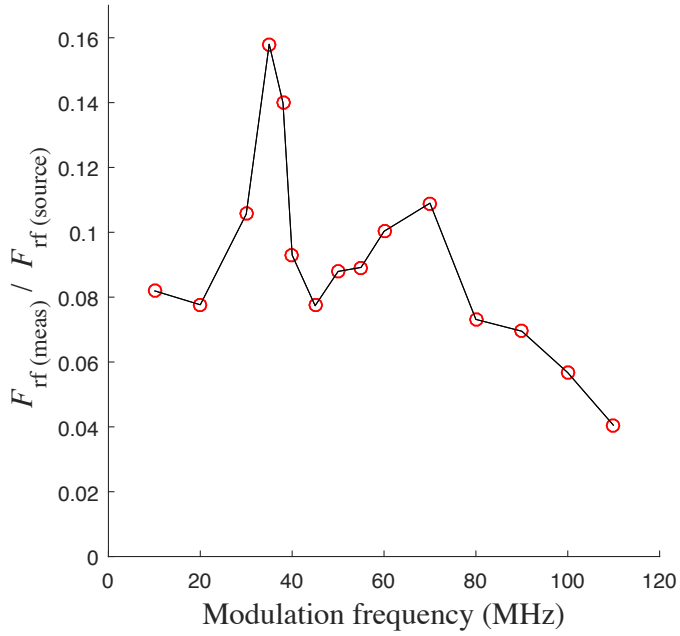

Figure 5.4: The frequency dependence of the ratio between the measured rf electric field strength and that expected for the voltage at the output of the rf source for frequencies between 10 and 110 MHz.

number q, is given by [39]

$$I_q \cong \left| J_q \left(\frac{\mu_{\text{elec}} F_{\text{rf}}}{\hbar \omega_{\text{rf}}} \right) \right|^2 \tag{5.1}$$

where J_q is the Bessel-Function, μ_{elec} is the mean induced electric dipole moment of the two states, and F_{rf} is the amplitude of the electric field modulation with angular frequency ω_{rf}.

Figure 5.3 shows microwave spectra (black lines) recorded for three different modulation amplitudes of V_{rf} = 101, 56 and 1 mV for ν_{rf} = 10 MHz [Figure 5.3(a), (b) and (c), respectively]. The measured relative intensities of these sidebands were fit to Eq. 5.1 (red bars) to determine the field strength, $F_{\text{rf(meas)}}$, which was then compared to the expected unattenuated field strength, $F_{\text{rf(source)}}$, to obtain the attenuation at this frequency. This process was repeated for a range modulation

frequencies between 20 and 110 MHz, with the results presented in Figure 5.4. It can be seen from the data in this figure that for frequencies close to 35 and 70 MHz the attenuation was minimal. As the frequency was increased above 80 MHz, so did the attenuation.

5.4 State-selective detection

In these experiments, slowly rising pulsed electric fields were used to ionise and detect the Rydberg atoms. The time at which the electrons were detected on the MCP was directly correlated with the electric field at the time of ionisation. Consequently, the states populated before ionisation could be identified in the ionisation process. Figure 5.5(a) demonstrates how this state-selective detection scheme was calibrated. Each hydrogenic n=52 Rydberg-Stark state, with Stark indices k=-49,-47...47,49, was individually prepared using the optical-optical-microwave triple-resonance method described in Section 5.2 and ionised using the same slowly rising ionisation electric field. The resulting electron signal recorded for each state can be seen in the figure. For states up to $k \simeq +37$, a clear ionisation signal can be identified. Because of the reduced signal measured for states with $k > 0$, states with $k < 0$ were selected for the main studies described here. The red curve overlaid on the experimental data in Figure 5.5(a) represents the calculated ionisation field for the corresponding hydrogen-like Rydberg-Stark states in He in which the ionisation rate of each state = 10^8 s^{-1}. The tunnel ionisation rates, $\Gamma_{nn_1n_2m}$, of these states can be determined using the semi-empirical expression evaluated by Damburg and Kolosov [38]:

$$\begin{aligned}\Gamma_{nn_1n_2m} =& \frac{E_{\rm h}}{\hbar}\frac{(4C)^{2n_2+m+1}}{n^3 n_2!(n_2+m)!}\exp\left[-\frac{2}{3}C-\frac{1}{4}n^3\frac{ea_0F}{E_{\rm h}}\right.\\ &\left.\times\left(34n_2^2+34n_2m+46n_2+7m^2+23m+\frac{53}{3}\right)\right],\end{aligned} \tag{5.2}$$

where

$$C = \frac{1}{ea_0\sqrt{E_{\rm h}}}\frac{(-2E_{nn_1n_2m})^{3/2}}{F}, \tag{5.3}$$

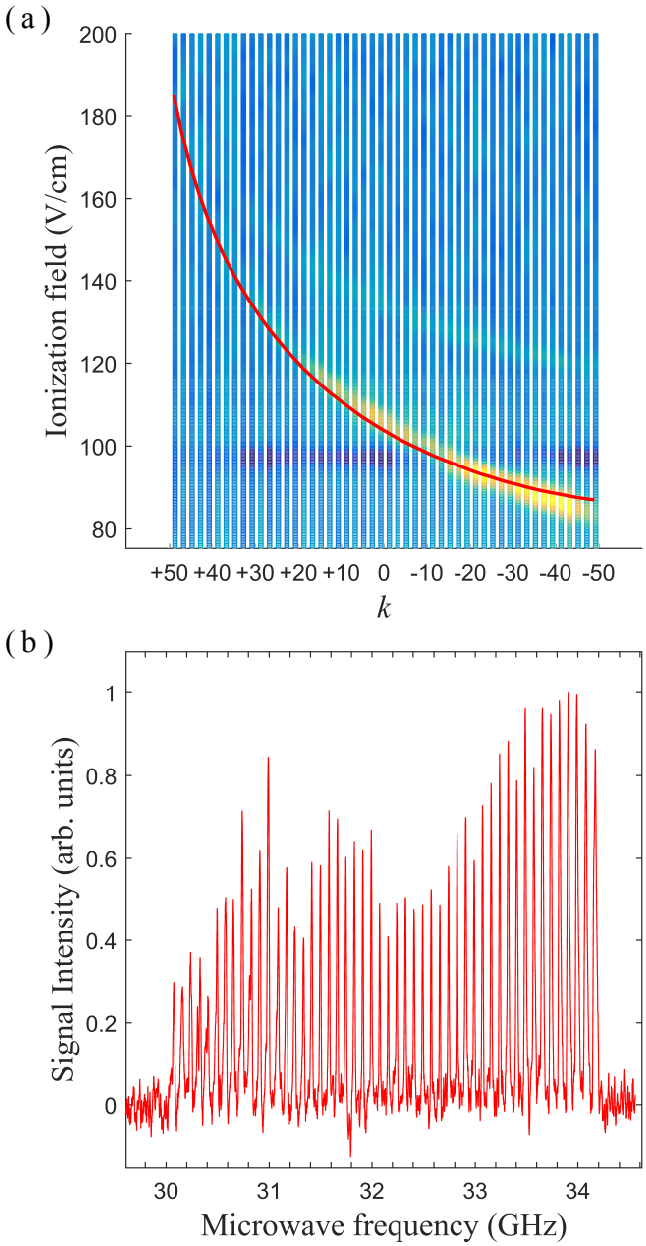

Figure 5.5: (a) Rydberg-Stark-state-selective detection by pulsed electric field ionisation. The colour map shows the measured ionisation signal for each Stark state. The red curve represents the calculated ionisation field for which the ionisation rate for each state is 10^8 s^{-1}. (b) Microwave spectrum of transitions from the $|53s'\rangle$ state to all Stark states with $n = 52$ indicating all of the transition frequencies used in the preparation of the states when recording the data in (a).

$E_{\mathrm{h}} = 2hcR_M$ is the Hartree energy and $E_{nn_1n_2m}$ is the energy of the state, with respect to the field-free ionisation limit, in the presence of the electric field.

In addition to the primary Stark state dependent ionisation signal, that closely follows the calculated curve, two further features can be seen in this data. The 'echo' that appears at fields 10 - 40 V·cm^{-1} higher than the primary ionisation peak for each state is caused by secondary electrons generated following the acceleration of the He^+ ions into the electrode to which the negative ionisation potential was applied for field ionisation. These secondary electrons were accelerated to the MCP by the ionisation field, arriving after the field-ionised electrons. The feature at $\sim$ 95 V·cm^{-1} in all of the traces in Figure 5.5(a) has a similar origin. However, in this case, secondary electrons are generated following the ionisation of the $|53s\rangle$ state. These electrons are present in the background trace that was subtracted from all data sets. A corresponding microwave spectrum recorded by integrating the electron signal for the $|53s\rangle$ state is shown in Figure 5.5(b). This demonstrates the excellent quantum state resolution that allowed for precise initial state preparation in the experiment.

5.5 Results

To investigate the frequency dependent depolarisation of the Rydberg-Stark states, a selected initial Stark state, k_0, was prepared before applying the rf modulation as a fixed amplitude modulation of the applied electric potential of 32 mV over a range of frequencies between 10 and 110 MHz for a duration of 5 μs. Figure 5.6 shows the results of these tests for $k_0 = -45$ in which the remaining population in the initially prepared state after the modulation pulse had been applied was monitored. The data in this figure have been corrected to account for the variations in the rf field strength determined from Figure 5.4. It can be seen in Figure 5.6 that for certain modulation frequencies, population loss from the initial state occurs.

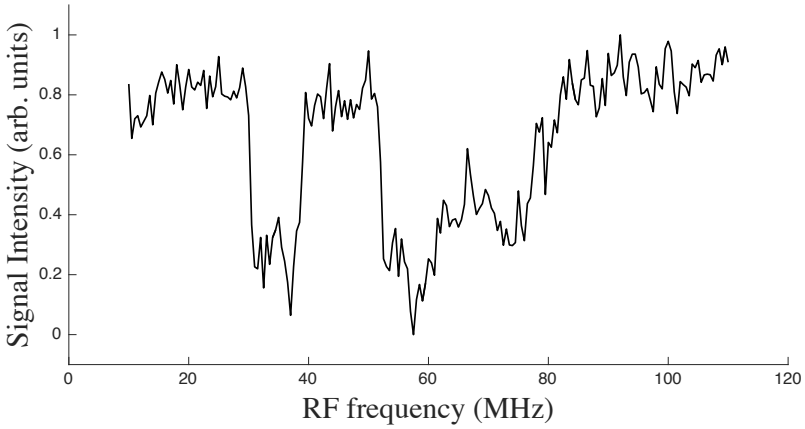

Figure 5.6: RF spectrum showing frequency dependent depolarisation of the $k_0 = -45$ Rydberg-Stark states. The most efficient depolarisation occurs at frequencies of around 30, 60 and 70 MHz.

To determine the range of Stark states over which the population was distributed in the depolarisation process identified in the data in Figure 5.6, a second measurement was made for the same time duration, but with $\nu_{\mathrm{rf}} = 70$ MHz. In this study the populations of a range of Stark states were monitored as the amplitude of the rf modulation was adjusted. Figure 5.7 shows the normalised populations of states for which $\Delta k = 0, +10, +20, +30$ and $+40$ when these experiment were performed with $k_0 = -45$. The small recorded initial populations in states other than the k_0 state at $0\ \mathrm{mV{\cdot}cm^{-1}}$ ($\Delta k = +10, +20$) are a result of the limited resolution of the state-selective detection process. These data are normalised to the maximum signal measured in the initial state. The rise in population observed in the initially prepared state for low amplitude modulations, without any corresponding change in population of other states, suggests that some of the atoms prepared initially were in states which ionise in a way that was not monitored in the detection process, i.e., by adiabatic electric field ionisation. These states require larger electric fields to ionise than those applied in the detection scheme. The low field strength modulation therefore

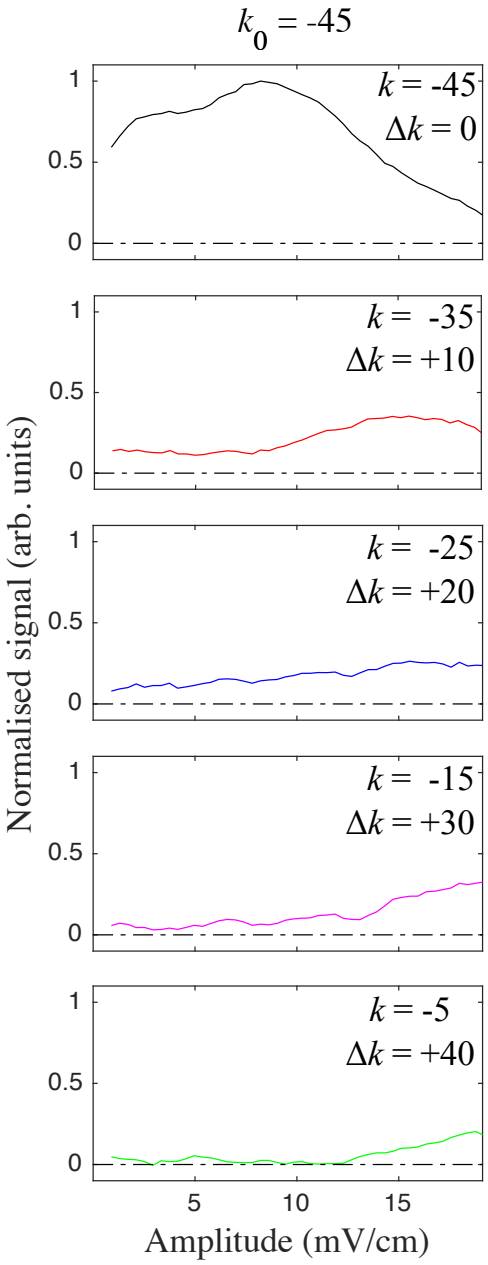

Figure 5.7: Rydberg-Stark state population transfer resulting from rf modulation at $\nu_{\mathrm{rf}} = 70$ MHz for an initial state $k_0 = -45$. The individual panels indicate the population in states for which $\Delta k = 0, +10, +20, +30$ and $+40$. The modulation amplitude has been corrected for the measured frequency dependent attenuation in the apparatus.

caused more atoms to ionise in a way that could be observed, i.e., diabatically. After this initial increase in the signal observed the k_0 state population decreases with higher rf amplitudes and the population of the other states increases. The states closer to the initial state become populated at lower rf modulation amplitudes than those further away. For example, the state for which $\Delta k = +10$ attains population for modulation amplitudes of $\sim$8 mV·cm^{-1} whereas it requires $\sim$12 mV·cm^{-1} before the state for which $\Delta k = +40$ state becomes populated. The data in Figure 5.7 demonstrate that the depolarisation of the initially prepared state is caused by transitions 'spreading population out' through neighbouring states. Monte Carlo simulations performed that accounted for $\Delta k = \pm 2$ transitions, i.e., from one Stark state to a neighbouring one with the same value of $|m_\ell|$, exhibited the same general trends, however, they did not provide a good quantitative fit and suggest that more complex population transfer dynamics occurred in the experiments. This can be explained fully by Floquet analysis which allows for a more complete treatment of the perturbation of the atom by the oscillating field. The analysis transforms the time-dependent problem with periodic driving into a time-independent problem in a basis containing the field free atomic energy levels and the photon number states at the frequency of the driving field [50].

The rf modulation frequency of ν_{rf}=70 MHz was chosen for the measurements in Figure 5.7 because the rf attenuation is low, while still being close to resonant with the calculated energy separation between the Stark states. The depolarisation of the Rydberg-Stark states seen in Figure 5.7 is therefore referred to as 'near-resonant' depolarisation. Further data were recorded to investigate broadband depolarisation such as that which may be induced by electric field noise. The corresponding measurement procedure was similar to that used to study 'near-resonant' depolarisation, but instead of the frequency of the noise being set to 70 MHz, broadband white noise covering a range of frequencies from 0 to 120 MHz

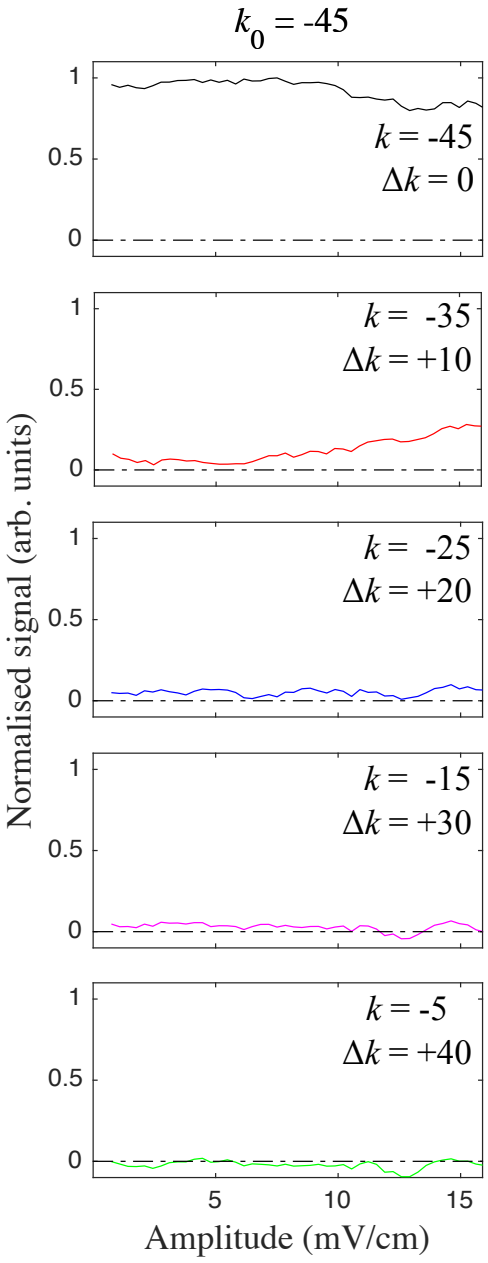

Figure 5.8: Rydberg-Stark state population transfer resulting from broadband bandwidth rf modulation at frequencies ranging from 0 to 120 MHz for the initially populated state $k_0 = -45$. The individual panels indicate the population in states for which $\Delta k = 0, +10, +20, +30$ and $+40$. The modulation amplitude has been corrected for the average measured frequency dependent attenuation in the apparatus.

was generated. The results of these measurements for $k_0 = -45$ are shown in Figure 5.8. Again these data are normalised to the maximum signal intensity of the initially prepared state, and the rf modulation amplitude corrected to account for the average attenuation over the frequency range from 0 to 120 MHz arising from the imperfect impedance matching. These results lack the rise in population of the initially prepared state at low powers exhibited in the resonant case, indicating that the contribution from m_ℓ-changing is not as significant. At high powers population is still transferred away from the initially prepared state, however, it occurs less efficiently than in the resonant case with a smaller drop in population of the initially prepared state and only the $|\Delta k| = 10$ transitions occurring at $\sim$15 mV·cm^{-1} whereas, in the resonant cases, the state changes for which $|\Delta k| = 40$ had occurred at this modulation amplitude.

5.6 Conclusion

The experiments presented here demonstrate that both narrow bandwidth near-resonant and broadband electric field modulation can lead to significant depolarisation of Rydberg-Stark states. In the broadband case, which mimics effects of electric field noise in Rydberg-Stark deceleration and trapping experiments, modulation amplitudes on the order of 10 mV·cm^{-1} were sufficient to cause depolarisation on a timescale of 5 μs in a field of 0.43 V·cm^{-1}, in which the intervals between Stark-states with the same value of m_ℓ were $\sim$ 70 MHz. This observation highlights the importance of minimising electric field noise in Rydberg-Stark deceleration experiments. Near-resonant depolarisation of the Rydberg-Stark states showed an enhancement when the modulation frequency corresponded to the energy of an allowed transition between Stark states. This suggests that care must be taken not to introduce modulations at such frequencies into experiments, e.g., in the form of oscillating trapping potentials, which are typically in the rf-frequency range [53, 54]. In ad-

dition to particle losses in Rydberg-Stark deceleration and trapping experiments, experiments that rely on state-selective detection could produce misleading results if the states depolarise because of effects of rf noise before detection.

Chapter 6

Matter-wave interferometry

The scientific content of Section 6.4 in this chapter has been published in

- Palmer, J. E., & Hogan, S. D., “Electric Rydberg-Atom Interferometry", *Phys. Rev. Lett.* **122**, 250404 (2019).
- Palmer, J. E., & Hogan, S. D., “Matter-wave interferometry with atoms in high Rydberg states", *Mol. Phys.* **117**, 3108-3119 (2019).

However, the parts of the text drawn from these articles has been adapted to fit within the context of this thesis.

6.1 Methods

At present, the most widely used techniques for matter-wave (or de Broglie wave) interferometry exploit either photon recoil in atomic transitions, or solid-state or optical diffraction gratings. In 1991, four seminal interferometry experiments were performed in which two of these methods were demonstrated for the first time.

In an experiment analogous to Young’s double slit experiment, Carnal and Mlynek [55] formed a beam of metastable He atoms in the 1s2s $^3S_1$ level with a long

transverse coherence length by passing the atoms through a 2-μm-wide slit in a gold film before directing it towards a grating structure formed of two 1-μm-wide slits separated by 8 μm. The spatial distributions of the atoms resulting from the matter-wave interference between the two components of the beam transmitted through this pair of slits were measured using both a single slit, identical to the source slit, and a grating with a period coincident with the period of the interference pattern.

At the same time another experiment, performed by Keith et al. [56], used three identical 0.4-μm-period gratings in a setup where atoms transmitted through two gratings formed an interference pattern at the position of the third. This third grating then acted as a mask to sample the interference pattern. These experiments were carried out with ground-state sodium atoms and resulted in an interferometry scheme in which the interfering trajectories were not only separated in position but also in momentum.

In the third experiment also performed at this time, Riehle et al. [57] utilised a light-pulse interferometry scheme proposed earlier by Bordé [58] to observe the Sagnac effect, a phase shift of a matter-wave ,or electromagnetic-wave, induced by rotation. This scheme relied on the use of two counter-propagating lasers to induce four separate Ramsey transitions to coherently split and recombine matter-wave components generated by photon recoil upon absorption. The refinement of this method has lead to extremely precise measurements of, e.g., gravity gradients.

Finally in the same year, another light-pulse atom interferometer was also demonstrated. In this work, Kasevich and Chu [59] coherently split and recombined sodium atom matter-waves using a two-photon Raman transition between two hyperfine ground states. The full interferometry scheme consisted of a $\pi/2 - \pi - \pi/2$ sequence of Raman pulses and relied on the atomic recoil that occurred during each of these manipulations. Starting with a wavepacket of momentum p and an internal state $|1\rangle$, the first $\pi/2$ pulse yielded a superposition of the states $\left|1, p\right\rangle$ and $\left|2, p + 2\hbar k\right\rangle$,

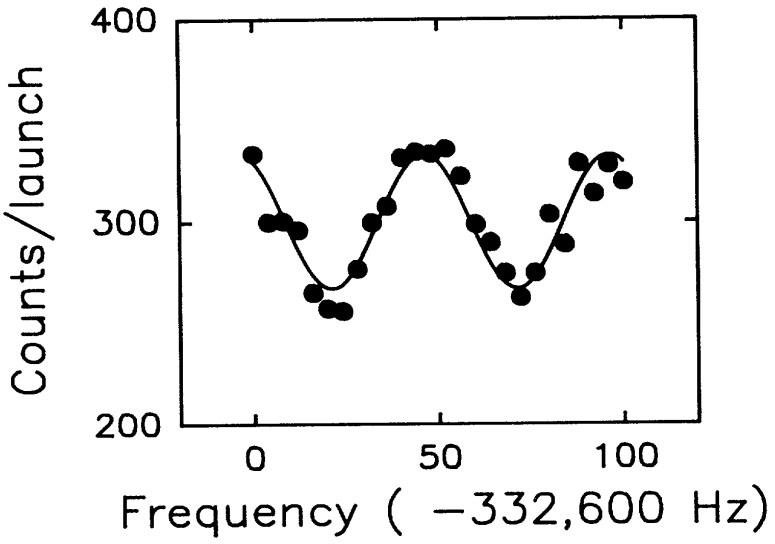

Figure 6.1: Interference fringes observed following the implementation of a stimulated Raman transition light-pulse interferometry scheme. From Reference [59].

where $2\hbar k$ is the momentum imparted to the atom by the absorbed photons. After a time Δt, the wavepackets were spatially separated by $2\hbar k\Delta t/M$, where M is the mass of the atom. The π pulse then induced the transitions $|1,p\rangle \rightarrow |2,p+2\hbar k\rangle$ and $|2,p+2\hbar k\rangle \rightarrow |1,p\rangle$ and after another time interval Δt, the wavepackets recombined. The final $\pi/2$ Raman pulse projected the superposition of internal atomic energy levels at the end of the sequence onto the basis states, $|1\rangle$ and $|2\rangle$. By adjusting the phase of this pulse, atoms could be transferred into either state. An interference pattern obtained by varying the frequency of the Raman pulses in the experiment can be seen in Figure 6.1. Ultimately in this work, a measurement of g was performed to a precision of $3 \times 10^{-6} g$.

In 2003, a refined version of the atom interferometry technique of Kasevich and Chu allowed Peters et al. [60] to perform the most precise measurements of gravity to date. When an atom interacts with the Raman beams used to perform

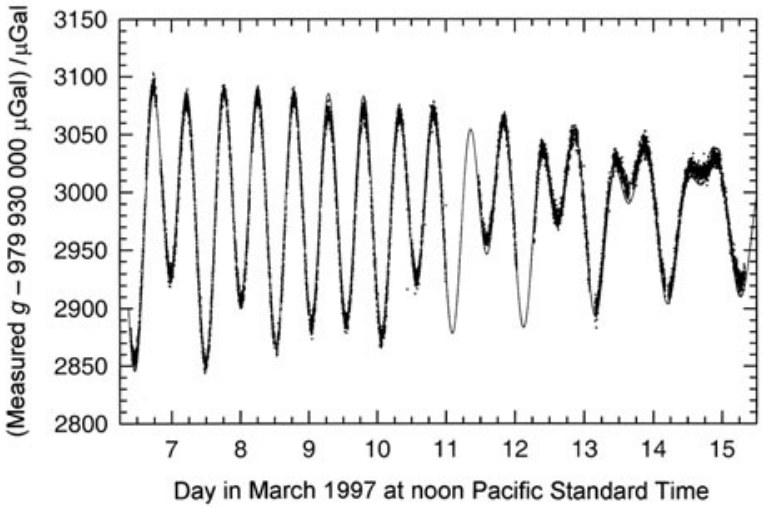

Figure 6.2: Variations in local gravity, mainly caused by tidal effects, over the course of 9 days as measured by a refined version of the Kasevich-Chu interferometry scheme. From Reference [60].

the interferometry it acquires a phase shift. In the absence of gravity the trajectories of the resulting atomic wavepackets are all straight lines and the symmetry of the interferometer paths results a phase difference $\Delta\phi = 0$. A gravitational field breaks this symmetry as any individual atom will fall three times as far during transit in the second half of the interferometer than in the first half. This leads to a phase shift in the observed interference pattern that is proportional to gravitational acceleration, i.e., $\Delta\phi = k_{\text{eff}} g T^2$, where k_{eff} is the effective wavenumber of the two counter-propagating Raman beams. Further analysis of the interferometer, to account for gravity gradients, allowed a measurement of g with a precision of $\Delta g/g = 1 \times 10^{-10}$ after a one day integration time. Figure 6.2 shows the variation in local gravity over the course of 9 days measured using this method.

The first demonstration of matter-wave interferometry using an optical diffraction grating was reported in in 1995. In this experiment, performed by Rasel et al. [61], a similar setup to the three-grating scheme described above was employed,

however, the material gratings were replaced by standing light waves with a wavelength of 811 nm. This experiment represents a hybrid of the material-grating and light-pulse interferometers developed previously. In a scenario where the standing light waves are formed of two counter-propagating waves, each atomic wavepacket is coherently split by absorbing a photon from one of these waves and emitting it into the other, acquiring the same $\Delta 2\hbar k$ momentum difference that the Kasevich-Chu–Raman-transition interferometry scheme described above relies upon. However, in this approach to atom interferometry the laser radiation does not have to be resonant with an atomic transition for this to occur and therefore, as with solid-state grating interferometers, its operation is not dependent on specific internal atomic states.

6.2 Transmission of Rydberg atoms through a diffraction grating

When considering the possibility of implementing matter-wave interferometers for atoms in high Rydberg states, i.e., a Rydberg-atom interferometer, the possibility of using diffraction gratings has been considered. The transmission of Rydberg atoms through a material grating was studied by Fabre et al. [62] in 1983 in the context of measuring atomic dimensions. In the experiment, the transmission of sodium atoms photoexcited to Rydberg states, with values of n up to ~ 65, through a grating with a slit width of 2 μm was tested. It was found that the fraction of the excited atoms that passed through the grating scaled with n^2. This is consistent with a model in which the Rydberg atoms are viewed as spheres of diameter $3/2(a_o n^2)$ which are destroyed when they come into contact with the metal edge of a slit. This can be seen in Figure 6.3 for an atomic beam that is at normal incidence to the grating plane (crosses) and at an angle of 20° (circles). The rotation of 20° effectively

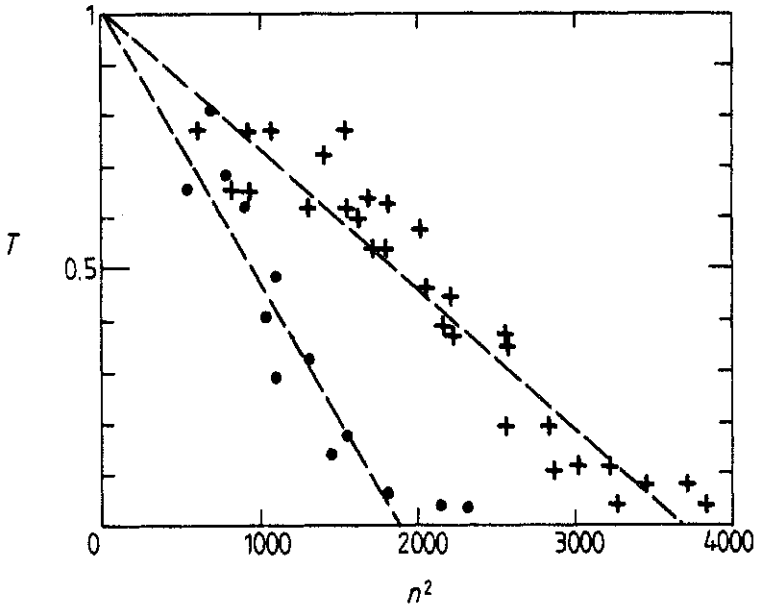

Figure 6.3: Transmission of Rydberg states through a grating with 2-μm-wide slits as a function of n^2 for an incident atom beam that is normal to the grating plane (crosses), and at an angle of 20° (circles). From Reference [62].

halves the slit width, as can be seen in the doubling of the slope, dT/dn^2, of the transmission function. Although the grating used in this experiment is unsuited for performing atom-interferometry, because of its large dimension and thickness, these experiments revealed important effects that limit the feasibility of using diffraction gratings for Rydberg-atom interferometry.

6.3 Matter-wave interferometry using inhomogeneous fields

Matter-wave interferometry [64, 65] in which the forces exerted by inhomogeneous electric or magnetic fields on atoms or molecules in coherent superpositions of internal states with different dipole moments was first considered from a theoretical perspective in the early 1950s [66, 67, 68]. This led to the realisation of an early electric atom interferometer [69, 70], and later the magnetic longitudinal Stern-Gerlach atom interferometer [71, 72, 63] – both demonstrated with hydrogen atoms in metastable $n = 2$ levels. In the latter, the experimental setup for which can be seen in Figure 6.4(a), atoms in coherent superpositions of Zeeman sublevels, prepared by a state mixer labelled M, travelled through a static inhomogeneous magnetic field, $\vec{B}$. As they entered this field, acceleration and deceleration of the three components of the initial internal state superposition resulted in the generation of a superposition of momentum states each with a different de Broglie wavelength, λ_{dB}. When the atoms exited the field the subsequent deceleration and acceleration of the three matter-wave components returned their momenta to the initial value. However, because of their different flight times through the magnetic field a spatial separation between the centres of mass of the matter wave packets remained. This process is depicted schematically in Figure 6.4(b) where a single initial de Broglie wavepacket is split into three spatially separated wavepackets after passing through an inhomogeneous magnetic field region. If this spatial separation was equal to λ_{dB} ($\lambda_{\mathrm{dB}}/2$) it led to constructive (destructive) matter-wave interference which was monitored

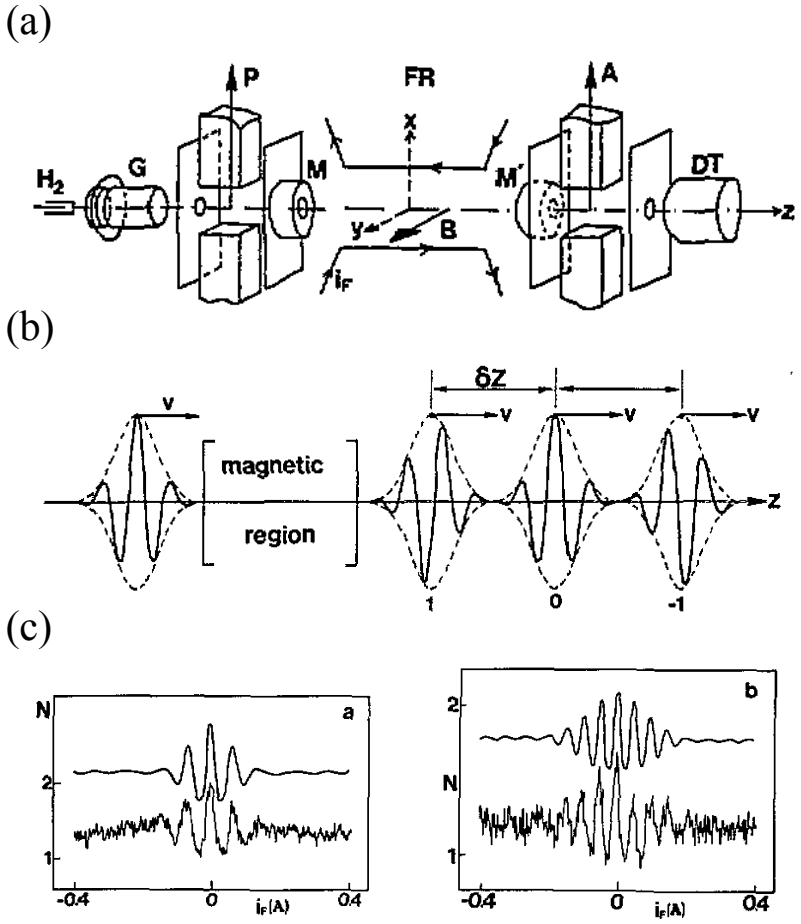

Figure 6.4: Longitudinal Stern-Gerlach interferometry. (a) Experimental setup. (b) Action of the inhomogeneous magnetic field on the external motional states of each of the components of the internal state superposition demonstrating equal momenta and spatial separation. (c) Measured interference patterns for beam velocity spreads of 6 - 8.6 k (left panel) and 4 - 5 $km \cdot s^{-1}$ (right panel). Adapted from Reference [63].

by projecting the final superposition of Zeeman sublevels onto the stationary basis states in the second mixer, M'. The interference fringes shown Figure 6.4(c) were observed by monitoring the internal quantum states of the detected atoms as the strength of the magnetic field was adjusted for two different beam velocity distributions.

Recently, in a similar vein, coherent momentum splitting of laser-cooled rubidium atoms, prepared in chip-based magnetic traps, was demonstrated using pulsed inhomogeneous magnetic fields and a sequence of rf pulses to prepare, and coherently manipulate, ground-state Zeeman sublevels [73]. In these experiments a $\pi/2$ pulse of rf radiation was first applied to prepare a coherent superposition of sublevels with magnetic dipole moments of equal magnitude but opposite orientation, in a homogeneous background magnetic field. The atoms were then subjected to a pulsed inhomogeneous magnetic field. The forces exerted by this field gradient on each component of the internal-state superposition resulted in the generation of a superposition of momentum states. Spatial interferences between the resulting pairs of matter waves were then observed by state-selective imaging of the atoms by laser-induced fluorescence. This approach has also now been extended to the implementation of a closed loop interferometer [74].

6.4 Electric Rydberg-atom interferometry

An approach to matter-wave interferometry for atoms in Rydberg states has been developed in the context of this thesis that has analogies with the methods of Stern-Gerlach magnetic interferometry discussed above.

This electric Rydberg-atom interferometry scheme relies on the initial preparation of a coherent superposition of two Rydberg states $|1\rangle$ and $|2\rangle$ with different electric dipole moments, $\vec{\mu}_{\mathrm{elec},i}$, where $i = 1, 2$. To implement this scheme, beginning with an atom in the $\left|1, \vec{p}_0\right\rangle$ state, where $\vec{p}_0 = M\vec{v}_0$ is the initial momentum of the

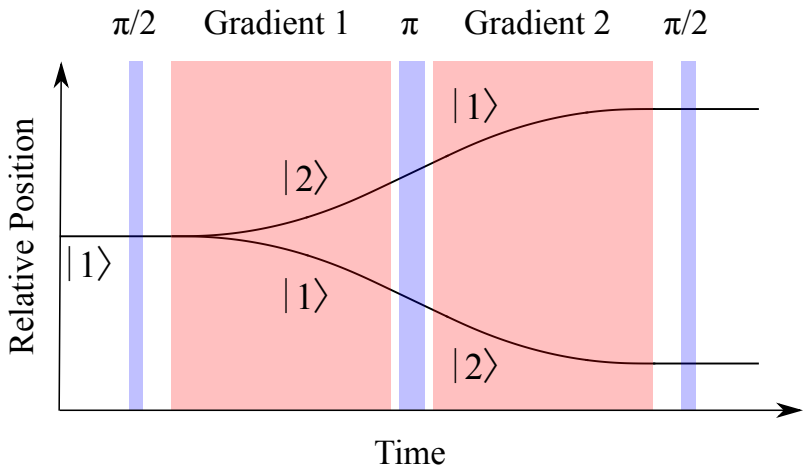

Figure 6.5: Schematic diagram showing the effect of the interferometry scheme on the relative positions of Rydberg-atom matter waves associated with two internal states with different electric dipole moments for fixed electric field gradient pulse parameters.

atom with velocity $\vec{v}_0$ and mass M, a pulse of microwave radiation resonant with the $|1\rangle \rightarrow |2\rangle$ transition is applied for a duration such as to cause a coherent $\pi/2$ rotation of the Rydberg-state population on the Bloch sphere. This operation results in the generation of an equal coherent superposition of the $\left|1, \vec{p}_0\right\rangle$ and $\left|2, \vec{p}_0\right\rangle$ states.

Atoms in this internal-state superposition are then subjected to a pulsed electric field gradient, $\nabla\vec{F}$. In this field gradient, each component of the superposition experiences a force proportional to its electric dipole moment and hence accelerates. This state-dependent acceleration is $\vec{a}_i = \vec{\mu}_{\text{elec},i} \cdot \nabla\vec{F}/m$. Since the two internal states have different electric dipole moments they each accelerate by a different amount, and when the gradient pulse is switched off, two matter-wave components with different momenta are generated. Over time, this momentum difference results in the accumulation of a displacement between these components. At the end of this stage of the interferometry procedure the quantum state of the system may therefore be described as an equal coherent superposition of the $\left|1, \vec{p}_0 + \mathrm{d}\vec{p}_1\right\rangle$ and $\left|2, \vec{p}_0 + \mathrm{d}\vec{p}_2\right\rangle$

states, where $d\vec{p}_i$ is the state-dependent change in momentum.

In the next step in the procedure, a second microwave pulse is applied to induce a π rotation on the Bloch sphere. This inverts the internal state population, i.e., $|1, \vec{p}_0 + d\vec{p}_1\rangle \rightarrow |2, \vec{p}_0 + d\vec{p}_1\rangle$ and $|2, \vec{p}_0 + d\vec{p}_2\rangle \rightarrow |1, \vec{p}_0 + d\vec{p}_2\rangle$. The atoms are then subjected to a second pulsed electric field gradient identical to the first. This combination of π and gradient pulses has the effect of transforming the momenta of the two components of the superposition state to be equal since the component that was accelerated more (less) by the first electric field gradient is accelerated less (more) by the second. The resulting quantum state of the system then becomes an equal superposition of the $|2, \vec{p}_0 + d\vec{p}_1 + d\vec{p}_2\rangle = |2, \vec{p}_3\rangle$ and $|1, \vec{p}_0 + d\vec{p}_2 + d\vec{p}_1\rangle = |1, \vec{p}_3\rangle$ states, where $\vec{p}_3 = \vec{p}_0 + d\vec{p}_1 + d\vec{p}_2$. At this stage in the sequence of pulses the displacement of the centres of mass of the two matter-wave components is fixed since they have equal momenta. They also have equal de Broglie wavelengths which allows for the observation of high contrast interference.

To complete the interferometry scheme a final $\pi/2$ microwave pulse is applied to project the final internal-state superposition onto the basis states $|1\rangle$ and $|2\rangle$. Since the internal Rydberg states of the atoms are entangled with the external motional states at the end of this interferometry procedure, selective detection of the populations of these two Rydberg states allows the effects of matter-wave interference to be observed. The phase accumulated by the momentum components of the superposition states leads to a corresponding phase accumulation in the internal state components. Aside from the difference in dipole moments between the two states, the final spatial separation of the two matter-wave components is governed by the magnitude and duration of the electric field gradient pulses, and the free-evolution time between them. Figure 6.5 shows how this interferometry scheme causes a relative displacement between the matter wave components associated with two states with different dipole moments for fixed gradient parameters. Rydberg-atom

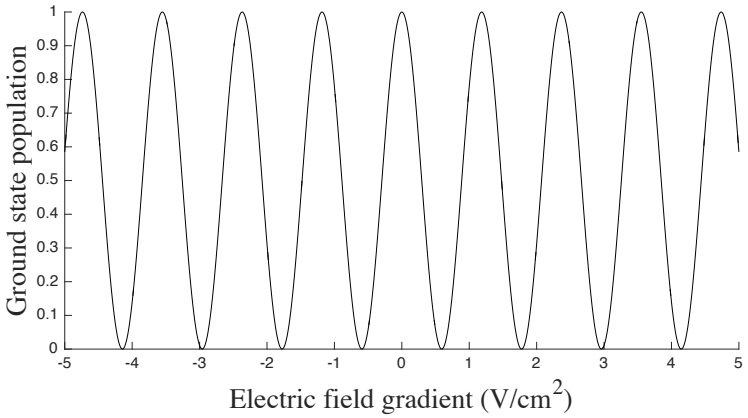

Figure 6.6: Calculated interference pattern obtained for the electric Rydberg atom interferometry scheme presented here, and implemented using Rydberg states in He with an initial speed of 2000 m·s^{-1} a difference in static electric dipole moments of $\sim$ 750 D.

interference fringes can therefore be seen by adjusting these parameters, for example, the magnitude or duration of the gradient pulses, or the free-evolution time between them.

Figure 6.6 shows a calculated Rydberg-atom matter-wave interference pattern obtained upon implementing this scheme with Rydberg states in He with a difference in electric dipole moments of $\sim$ 750 D using semiclassical methods. In the calculations, the classical trajectories of the atomic components along each path was calculated numerically. From the spatial separation between the end points of these trajectories the amplitude of the interference pattern associated with two de Broglie waves with this displacement was then determined. The initial speed of the atoms in the direction that the forces were applied was 2000 m·s^{-1}. Hence, the de Broglie wavelength of the atoms was $\sim$ 50 pm. The interference fringes seen arise when the magnitude of electric field gradient used to split the momentum components was varied. For these simulations the gradient pulse durations were 1 μs and they were

separated from each other in time by 100 ns.

Chapter 7

Implementation of an electric Rydberg-atom interferometer

The scientific content of this chapter has been published in

- Palmer, J. E., & Hogan, S. D., “Electric Rydberg-Atom Interferometry", *Phys. Rev. Lett.* **122**, 250404 (2019).
- Palmer, J. E., & Hogan, S. D., “Matter-wave interferometry with atoms in high Rydberg states", *Mol. Phys.* **117**, 3108-3119 (2019).

However, the text drawn from these articles has been adapted to fit within the context of this thesis.

7.1 Introduction

In all Rydberg-Stark deceleration experiments up to now, e.g., those discussed in Chapter 2, the atoms or molecules were prepared in selected Rydberg states by laser photoexcitation, and under the conditions in which the experiments were performed, quantisation of the motional states of the samples could be neglected.

Consequently, this set of methodologies can be classified as incoherent Rydberg-atom or molecule optics. In this chapter, the results of Rydberg-Stark deceleration experiments are presented that were performed with atoms prepared in coherent superpositions of Rydberg states with different electric dipole moments. In the presence of inhomogeneous electric fields the different forces on these internal-state components allowed the generation of superpositions of momentum states which have been exploited for Rydberg-atom interferometry. Experiments of the kind reported here may therefore be classified as coherent Rydberg-atom optics. The results presented open new opportunities in the exploration of the boundary between quantum and classical mechanics, the study of spatial decoherence in large quantum systems [75], investigations of quantum phases associated with the motion of particles with large static electric dipole moments in magnetic fields [76, 77, 78], and measurements of the acceleration of neutral particles composed of anti matter, e.g., Rydberg Ps or antihydrogen, in the gravitational field of the Earth [79, 49, 16, 48].

7.2 Specific scheme implementation

Circular Rydberg states were chosen for the first experimental implementation of the electric Rydberg-atom interferometry scheme presented in Chapter 6 because the large electric dipole moments for transitions between them allowed fast state preparation and manipulation with pulsed microwave fields. These states also have low sensitivities to weak stray electric fields and electric field noise resulting in minimal decoherence under these conditions. In addition, since blackbody transitions from these states are significantly restricted by the electric dipole selection rules, changes in their population between the end of the interferometry pulse sequence and the time of detection by pulsed electric field ionisation was minimal.

In the experiments described here, the $n = 55$ and $n = 56$ circular Rydberg states in He, denoted $|55c\rangle$, and $|56c\rangle$, were used. The effect of the interferometry scheme

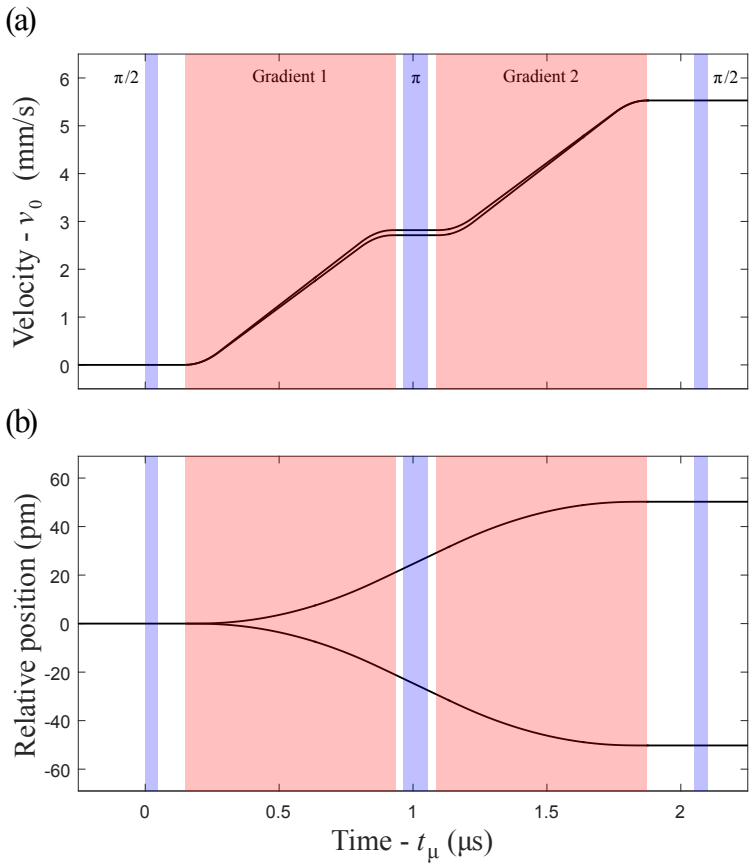

Figure 7.1: Calculated classical phase-space trajectories of He atoms in the Rydberg-atom interferometer. (a) The velocity, and (b) the relative position in the y dimension of the trajectories demonstrating equal momenta and a fixed spatial separation at the end of the interferometry procedure. For these calculations $v_0 = 2000$ m·s^{-1}, $V_{\text{grad}} = 1.3$ V, $T_{\text{grad}} = 525$ ns and $\tau_{\text{grad}} = 130$ ns (see text for details).

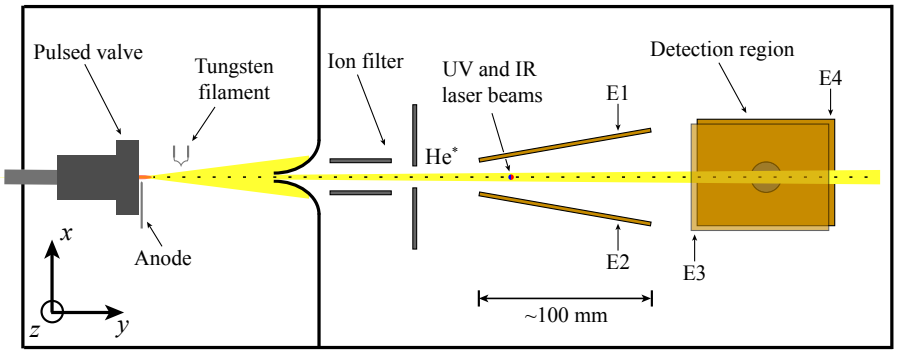

Figure 7.2: Schematic diagram of the experimental apparatus. Rydberg-atom photoexcitation and interferometry were performed within the wedge structure formed by electrodes E1 and E2. State-selective detection by pulsed electric field ionisation occurred between electrodes E3 (partially transparent in the figure) and E4. The MCP detector, to which the ionised electrons were accelerated, was located behind E4.

described in Chapter 6 on the classical phase-space trajectories of atoms in these two states is shown Figure 7.1. It can be seen from these plots how the scheme results in two matter-wave components with equal momenta and a fixed spatial separation. The electric field gradients generated by applying pulsed potentials on the order of ~1 V to an appropriately designed wedge-shaped electrode configuration are expected to give rise to matter-wave displacements of ~100 pm at the time of detection at the end of a 2-μs-duration interferometry sequence. For atoms initially travelling at 2000 m·s^{-1} with a de Broglie wavelength of ~50 pm this is considered sufficient to observe several interference fringes.

7.3 Experiment

Figure 7.2 shows a schematic diagram of the experimental setup. A beam of metastable He atoms was generated as described in Chapter 3. For the experi-

ments here a wedge-shaped pair of 105×70 mm copper electrodes, labelled E1 and E2 in Figure 7.2, were used to implement the interferometry scheme and also served as the excitation and circular state preparation region in the apparatus. These electrodes were separated by 11.5 mm (35.8 mm) in the x dimension at the end nearest to the ion filter (detection region). Hence, for a potential difference of V_{grad} between them, the electric field gradient on the axis along which the atomic beam propagated was, to the first order, $\nabla\vec{F} \simeq V_{\mathrm{grad}}$ (0,0.056,0) V·cm^{-2}. At the position between these electrodes where their separation in the x dimension was 19 mm, the atoms were prepared in the $|n = 55, \ell = 54, m_\ell = +54\rangle \equiv |55\mathrm{c}\rangle$ circular Rydberg state using the crossed fields method described in Chapter 3 [80, 36]. To implement this, laser photoexcitation was carried out in the presence of perpendicular pulsed electric and static magnetic fields of (3.15,0,0) V·cm^{-1} and (0,0,15.915) G, respectively to populate the outer $n = 55$ Rydberg-Stark state. The wavelengths of the ultraviolet and infrared lasers used for this were $\lambda_{\mathrm{uv}} = 388.975$ nm ($\equiv 25708.6$ cm^{-1}) and $\lambda_{\mathrm{ir}} = 786.752$ nm ($\equiv 12710.5$ cm^{-1}), respectively [81]. After photoexcitation the electric field was switched off adiabatically to transfer the atomic population into the $|55\mathrm{c}\rangle$ state as indicated in Figure 7.3(a).

When circular state preparation was completed, the sequence of microwave and electric field gradient pulses used to implement the Rydberg-atom interferometry scheme was applied. This sequence was initiated at time $t_\mu = t_0 + 2.575$ μs [see Figure 7.3(b)]. At the end of this sequence, which lasted 2.1 μs, the atoms travelled for ~60 μs [see Figure 7.3(d)] to the detection region of the apparatus, ~ 130 mm downstream from the position of laser photoexcitation, where they were ionised by applying a slowly-rising potential that rose to a maximum value of -530 V to E3, generating fields of up to ~115 V·cm^{-1} directed parallel to the background magnetic field. The resulting electrons were accelerated through an aperture in E4 to an MCP detector. Since the $|56\mathrm{c}\rangle$ state ionises in a lower field than the $|55\mathrm{c}\rangle$ state, electrons

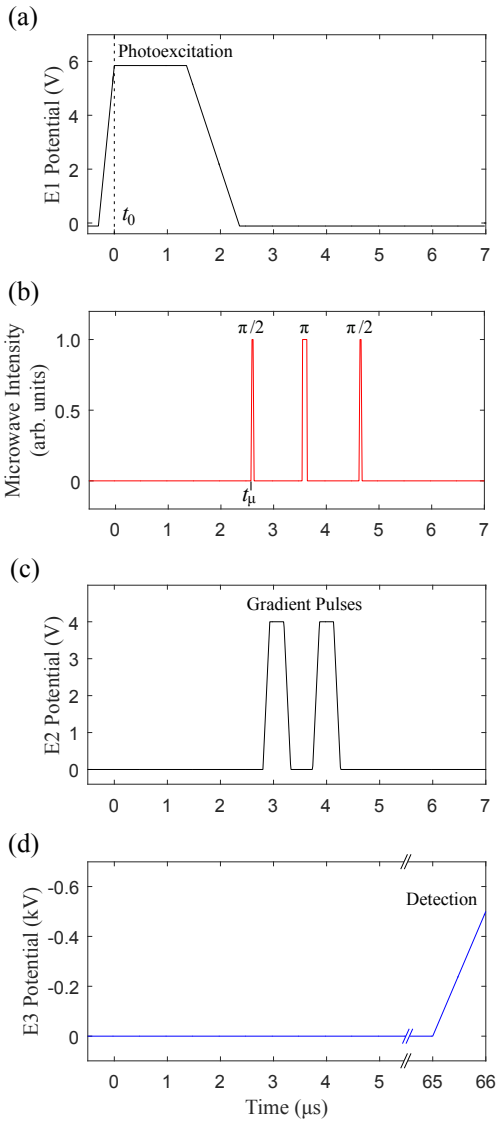

Figure 7.3: Sequence of pulsed electric potentials and microwave fields employed for Rydberg-atom interferometry. (a) Pulsed potential applied to electrode E1 for Rydberg-state photoexcitation and circular state preparation. (b) Set of three pulses of microwave radiation resonant with the $|55c\rangle \rightarrow |56c\rangle$ transition employed for coherent internal state preparation and manipulation. (c) Pair of pulsed potentials applied to electrode E2 to generate the electric field gradients required for interferometry. (d) Slowly-rising pulsed potential applied to electrode E3 for detection by state-selective electric field ionisation.

from atoms in this state appeared earlier in the time-of-flight distributions measured at the MCP. By selecting appropriate windows in the time-of-flight distributions, the populations of these two circular states of interest could be determined.

7.4 Microwave spectroscopy

High-resolution microwave spectroscopic studies of the $|55c\rangle \rightarrow |56c\rangle$ transition were carried out to calibrate and optimise the parameters required to implement the Rydberg-atom interferometry scheme described in Chapter 6. For the circular Rydberg states used in the experiments the Stark energy shifts in an electric field $\vec{F} = (F_x, 0, 0)$ acting in the direction perpendicular to the background magnetic field $\vec{B} = (0, 0, B_z)$ can be expressed as [80, 82]

$$E_{nc} = m_\ell \sqrt{\left(\mu_B B_z\right)^2 + \left(\frac{3}{2} nea F_x\right)^2}, \tag{7.1}$$

where m_ℓ is defined with respect to the magnetic field quantisation axis, and μ_B, e and a are Bohr magneton, electron charge and Bohr radius corrected for the reduced mass, respectively. In weak electric fields, i.e., when the electric field term in Eq. 7.1 is smaller than the magnetic field term, this expression results in quadratic Stark shifts of the circular Rydberg states. As the field strength is increased, the electric field term begins to dominate that associated with the magnetic field and the Stark energy shifts become increasingly linear.

To compensate the $(32, 0, 0)$ mV·cm^{-1} motional Stark effect [83] and weak stray electric fields in the apparatus, microwave spectra of the $|55c\rangle \rightarrow |56c\rangle$ transition were recorded for a range of offset potentials, V_{off}, applied to E1. In recording these spectra, microwave pulses of 2 μs duration were applied at time t_μ [see Figure 7.3(b)]. The resulting data are presented in Figure 7.4(a) where the vertical offset of each spectrum corresponds to the value of V_{off}. From the resonance frequencies in each

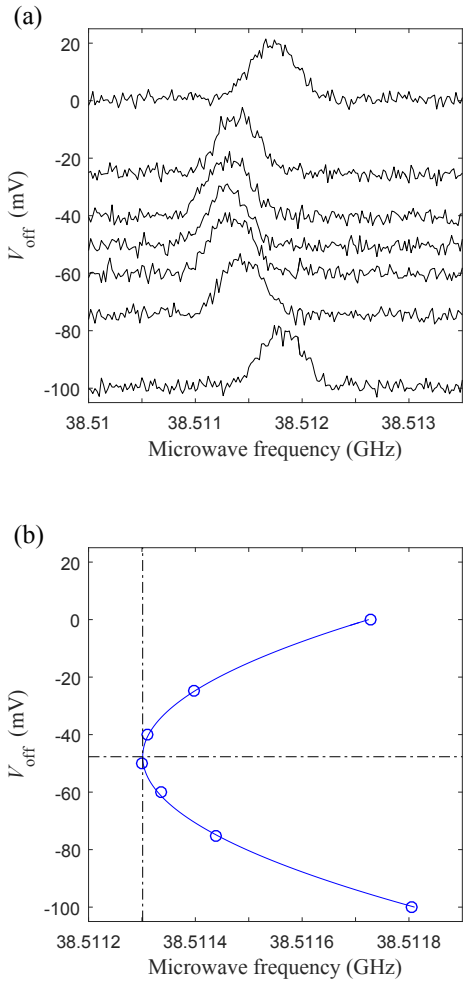

Figure 7.4: (a) Microwave spectra of the $|55c\rangle \rightarrow |56c\rangle$ transition showing the Stark shifts for offset potentials, V_{off}, applied to E2. In this panel the vertical offset of each spectrum indicates the value of V_{off} for which it was measured. (b) The quadratic function (continuous curve) fit to the measured transition frequencies obtained from the data in panel (a). The zero-electric-field transition frequency of ν_μ = 38.511313 GHz for an offset potential of V_{off} = -48 mV is indicated by the dashed lines in panel (b).

of these spectra, determined by fitting Gaussian functions to each dataset, and the corresponding value of V_{off}, the optimal compensation potential was determined by fitting a function that depended quadratically on V_{off}. The results of this procedure are displayed in Figure 7.4(b) and yielded a minimum, i.e., a zero-electric-field, transition frequency of $\nu_\mu = 38.511\,313$ GHz for $V_{\text{off}} = -48$ mV. From this transition frequency, the strength of the magnetic field at the position of the atoms in the apparatus was determined, using the Rydberg formula and the expression in Eq. 7.1, to be $B_z = 15.915$ G.

The accuracy of the hydrogenic expression in Eq. 7.1 for describing the Stark shifts of $|55c\rangle$ and $|56c\rangle$ states of He in weak perpendicular fields was tested by comparing experimentally recorded spectra with the calculated transition frequencies over a wider range of electric fields. The results of these measurements are displayed in Figure 7.5. In recording these spectra the microwave intensity was set to ensure that $< 10\%$ population transfer from the $|55c\rangle$ state to the $|56c\rangle$ state occurred. The spectral width of the transition in the measurement made in the electric field closest to zero (see left axis), for which V_{off} = -48 mV, is 590 kHz and corresponds approximately to the Fourier Transform limit of the 2-μs-duration microwave pulse. For the larger electric fields in which these spectra were recorded the spectral features are broader. This is because in these fields the atoms are polarised and therefore more sensitive to the inhomogeneity in the electric field and electric field noise [50, 51]. The dashed curve and red points overlaid on the experimental spectra in this figure represent the calculated and measured transition frequencies, respectively, and exhibit excellent quantitative agreement. From Eq. 7.1 the maximal induced electric dipole moments of the $|55c\rangle$ and $|56c\rangle$ states were determined to be 11 320 D and 11 740 D, respectively. The difference in these dipole moments converges to its maximal value of 420 D in fields above ~ 0.6 V·cm^{-1}.

To determine the appropriate length of time to apply microwave pulses to

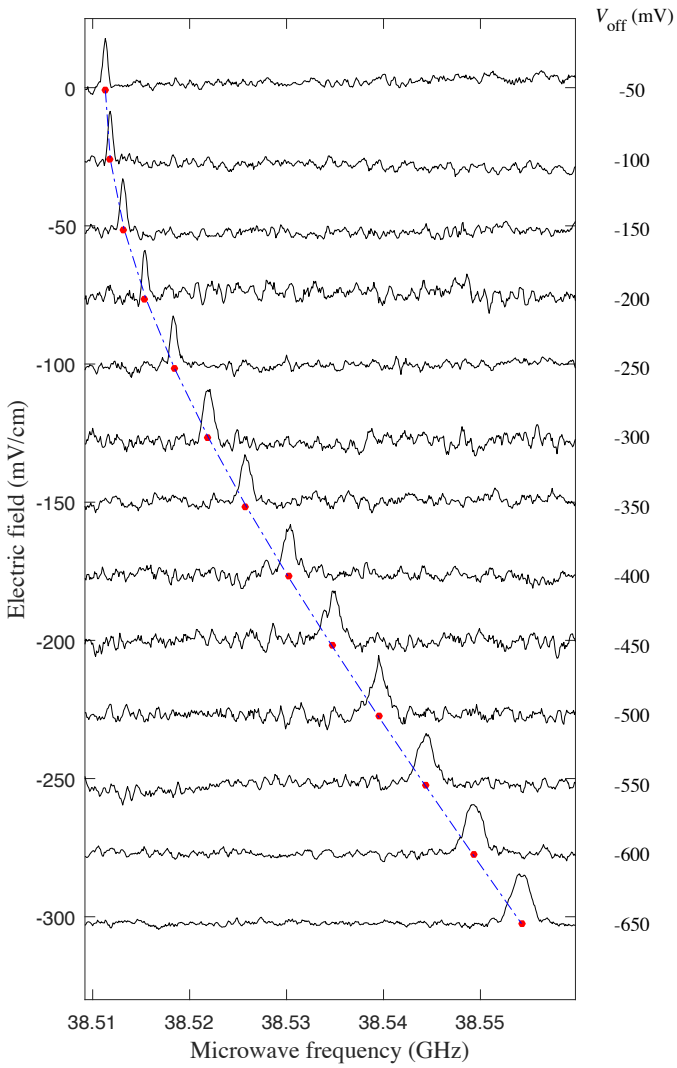

Figure 7.5: Microwave spectra of the $|55c\rangle \rightarrow |56c\rangle$ transition in a magnetic field B_z = 15.915 G and perpendicular electric fields as indicated on the left vertical axis. The corresponding values of the offset potential, V_{off}, applied to E1 are indicated on the right. The dashed curve represents the transition frequencies calculated using Eq. 7.1. The red points correspond to the experimentally determined transition frequencies.

realise the three coherent rotations on the Bloch sphere required to implement the interferometry scheme, i.e., a $\pi/2$ pulse to create an internal-state superposition, a π pulse to invert the states, and a final $\pi/2$ pulse to project back onto the basis states, the $|55c\rangle$ state was prepared as above and pulses of microwave radiation at the resonant frequency $\nu_\mu = 38.511\,313$ GHz were applied at a range of times, and with a range of durations. The results of these measurements can be seen in Figure 7.6 as Rabi oscillations in the population of the $|56c\rangle$ state. The time delays of t_μ, $t_\mu + 965$ ns and $t_\mu + 2050$ ns indicated in this figure correspond to the timings of the three microwave pulses in the interferometry measurements. From these results it was determined that the pulse durations required were $\tau_{\pi/2} = 48$ ns for the first $\pi/2$ pulse, $\tau_\pi = 88$ ns for the π pulse, and $\tau_{\pi/2} = 52$ ns for the second $\pi/2$ pulse. The inconsistency in the durations of these pulses, particularly the two $\pi/2$ pulses, is a consequence of the mode structure of the microwave field within the wedge configuration between E1 and E2. The periodicity and decoherence rates of these oscillations vary for the different time delays because of the inhomogeneity of the stray electric fields in the electrode structure. At each time delay the atoms are in a different location (~4 mm difference between t_μ and $t_\mu + 2050$ ns) and therefore experience slightly different electric fields and microwave field strengths.

The coherence of the circular state superpositions prepared in the experiments was characterised by Ramsey interferometry and spectroscopy. For these measurements, the results of which are displayed in Figure 7.7, only the 48- and 52-ns-duration $\pi/2$ pulses were applied. In the Ramsey interferometry measurement seen in Figure 7.7(a) the time interval between these pulses was adjusted as the population of the $|56c\rangle$ state was monitored. A first measurement performed on resonance, i.e., for $\Delta\nu_\mu = 0$ MHz, yielded an approximately constant population of this state for all time intervals between the $\pi/2$ pulses up to ~ 1.5 μs. After this the population reduced because of effects of decoherence and dephasing. In this set of data no

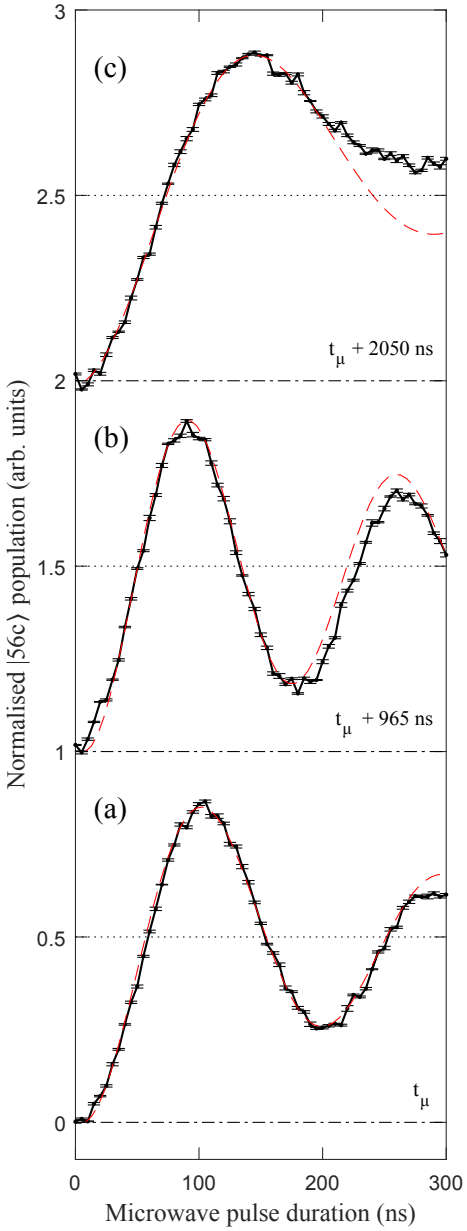

Figure 7.6: Rabi oscillations in the population of the |56c⟩ state upon resonant driving of the |55c⟩ → |56c⟩ transition for a fixed output power from the microwave source. Measurements were performed at the time delays of (a) t_μ, (b) t_μ+965 ns and (c) t_μ + 2050 ns at which each of the three microwave pulses required to implement the Rydberg-atom interferometry scheme was applied (see Fig 7.3).

oscillations in the |56c⟩ state population are observed because of the continuous evolution of the phase of the gated microwave field in the time between the two pulses. On the other hand, for a detuning of $\Delta\nu_\mu$ = +4 MHz periodic oscillations in the population of the |56c⟩ state are seen. These occur, as expected, at the frequency of 4 MHz associated with the detuning, and reduce in amplitude in a similar way to the data recorded on resonance. From these data the decoherence times of these states were determined to be ~ 5 μs, limited by the motion of the atoms. Because of the onset of more significant decoherence for times beyond 2.05 μs [dashed line in Fig 7.7(a)] this time interval was chosen as the maximal length for the sequence of pulses used in the interferometry experiments.

A Ramsey spectrum of the |55c⟩ → |56c⟩ transition recorded in the frequency domain with the same pair of $\pi/2$ microwave pulses separated by a free-evolution time of 2002 ns, corresponding to the application of the second $\pi/2$ at time t_μ + 2050 ns, is displayed in Figure 7.7(b). This spectrum further demonstrates the coherence of the atom–microwave-field coupling over the time scales of interest in the experiments. It also indicates an ~80% fidelity of this Ramsey sequence close to resonance and the accurate identification of the zero-electric-field resonance frequency for the transition.

7.5 Results

Having characterised each of the elements of the sequence of microwave and electric field gradient pulses required for Rydberg-atom interferometry, a series of experiments were performed to study the operation of the interferometer. In these experiments, the relative populations of the Rydberg states at the end of the interferometry procedure reflected the spatial overlap of the de Broglie waves associated with the two components of the superposition of momentum states at the time the second $\pi/2$ microwave pulse was applied (see Figure 7.3). This spatial separation

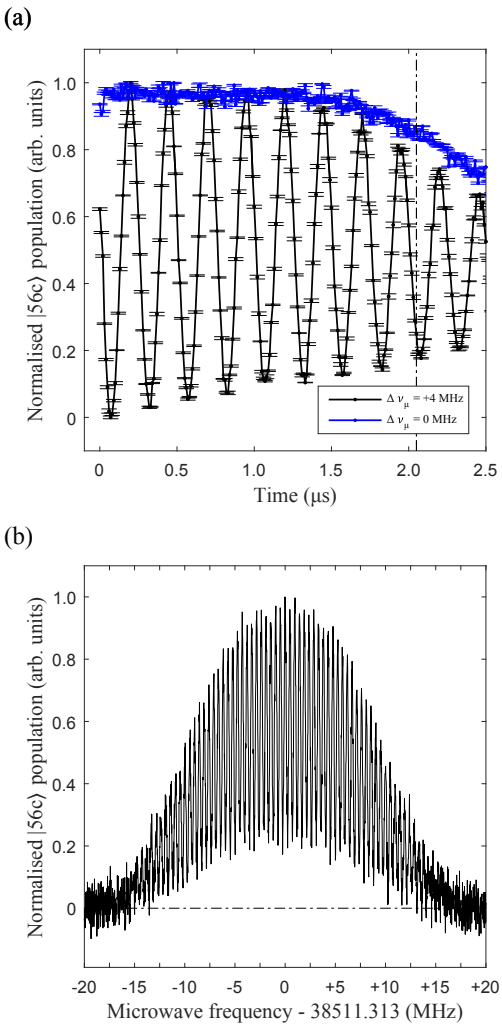

Figure 7.7: (a) Ramsey interferograms, and (b) Ramsey spectrum of the $|55c\rangle \rightarrow |56c\rangle$ transition in He. In (a) measurements performed for detunings of the microwave field from resonance of $\Delta\nu_\mu = 0$ MHz and $\Delta\nu_\mu = +4$ MHz are indicated by the blue and black data sets, respectively. The time interval of 2050 ns between the application of the two $\pi/2$ microwave pulses used ultimately for the Rydberg-atom interferometry experiments is indicated by the dashed vertical line. The spectrum in (b) was recorded for microwave pulses of the same duration as those used in (a) but for a fixed free-evolution time of 2002 ns.

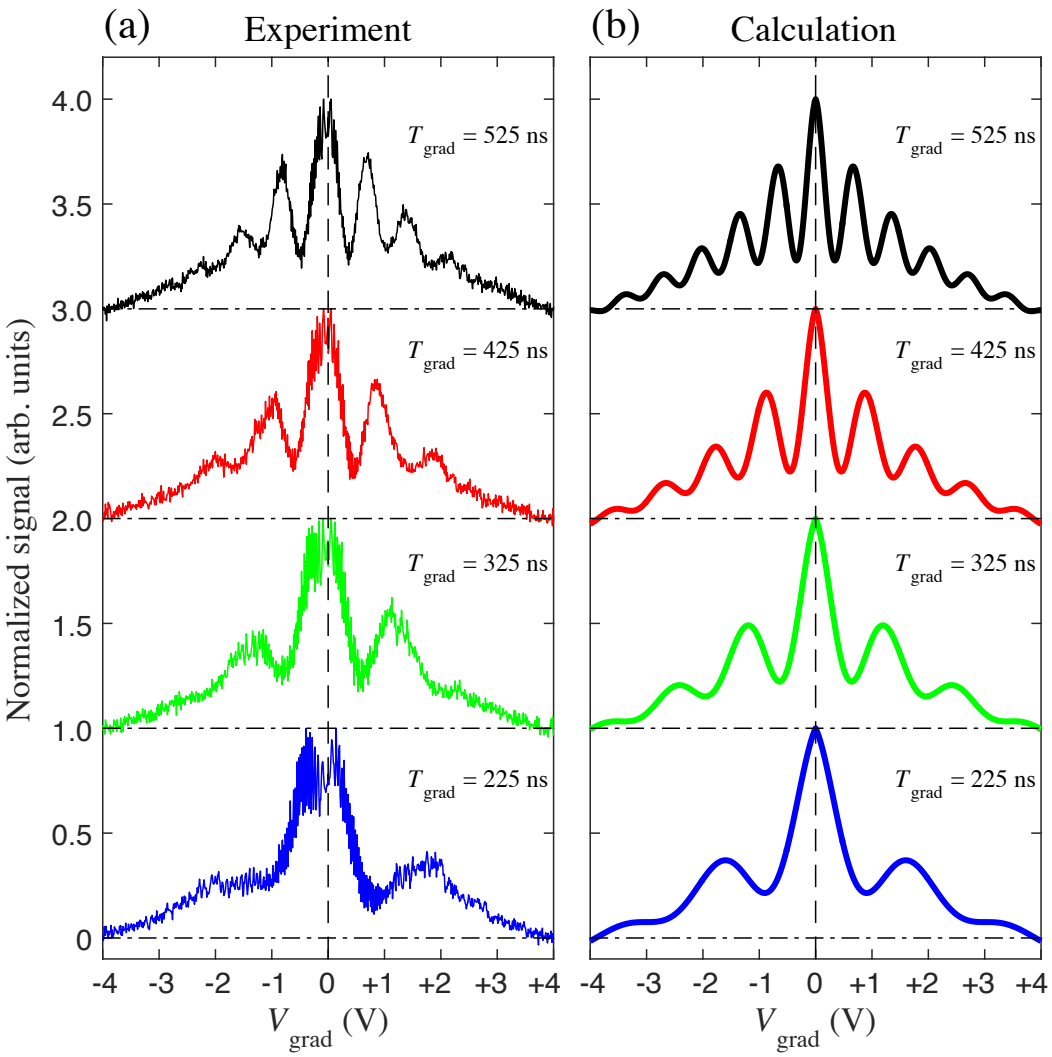

Figure 7.8: (a) Measured, and (b) calculated Rydberg-atom interference patterns obtained for pairs of electric field gradient pulses with durations T_{grad} = 225, 325, 425 and 525 ns. The amplitude of the electric potential, V_{grad}, applied to electrode E2 to generate the field gradients is indicated on the horizontal axis. In all cases, τ_{grad} = 130 ns.

was dependent on both the amplitude and duration of the electric field gradient pulses. Figure 7.8(a) shows interference patterns measured by adjusting the amplitudes of the pulsed electric potentials applied to generate the gradient pulses for four different gradient pulse durations, T_{grad} = 225, 325, 425 and 525 ns. These durations are the length of time for which the potentials applied to generate the gradients were at their maximum value, V_{grad}. In these cases each gradient pulse had rise and fall times of τ_{grad} = 130 ns. For each of these measurements the ratio of the |55c⟩-electron signal to that from the |56c⟩ state is displayed and normalised to one for the maximum measured signal in each data set. The signal maximum for values of $|V_{\mathrm{grad}}|$ close to zero indicates that the Rydberg-state population at the end of the interferometry sequence resided predominantly in the |55c⟩ state if no forces were exerted on the atoms. For the short gradient pulse of 225 ns, matter-wave interference begins to become observable for values of $|V_{\mathrm{grad}}| \gtrsim 0.2$. The first interference minimum, when the centres-of-mass of the two de Broglie wavepackets associated with the two Rydberg-atom momentum components are displaced by $\lambda_{\mathrm{dB}}/2$ at the time when the last $\pi/2$ microwave pulse was applied, is then observed for $|V_{\mathrm{grad}}| \simeq 0.9$. When the amplitude of the pulsed gradients are further increased the larger forces exerted on the atoms further displace the momentum components from each other. The relative displacement of the corresponding de Broglie waves is equal to λ_{dB} when $|V_{\mathrm{grad}}| \simeq 1.6$. The non-linear dependence of the values of $|V_{\mathrm{grad}}|$ at which these interference features occur is a result of the quadratic Stark shifts of the circular Rydberg states in weak electric fields (see Eq. 7.1 and Figure 7.5). For higher values of $|V_{\mathrm{grad}}|$ the contrast of the measured interference pattern reduces. A similar general behaviour is seen in the other interference patterns recorded. For these longer pulse durations, since the forces applied to generate the coherent superposition of momentum components are greater, larger matter-wave separations are achieved for each value of V_{grad}. In the case of the longest pulse duration,

$T_{\mathrm{grad}} = 525$ ns, the first interference minimum is observed for $|V_{\mathrm{grad}}| \simeq 0.4$ V while the following interference maximum occurs for $|V_{\mathrm{grad}}| \simeq 0.7$ V. It can be seen from the data that a greater number of interference fringes are seen as the pulse duration is increased. However, the dependence of the contrast of the observed fringes on the value of $|V_{\mathrm{grad}}|$ remains similar. This suggests that the loss of contrast is not a consequence of the displacement of the matter waves but is instead correlated with the amplitude of the pulsed inhomogeneous electric fields applied.

7.6 Calculations

To aid in the interpretation of the experimental data in Figure 7.8, numerical calculations of the matter-wave interference patterns were performed. In these calculations the classical equations of motion of atoms in the $|55\mathrm{c}\rangle$ and $|56\mathrm{c}\rangle$ states were solved in the magnetic and time-dependent inhomogeneous electric fields used in the experiments. These calculations were initiated after circular state preparation. From this time until the time at which the π pulse was applied, the forces exerted on each atom in the initial Rydberg state in which it was prepared were determined. At the time of the π pulse, the states for which the atomic trajectories were calculated were inverted. The calculations then continued until the end of the microwave pulse sequence. At this time, the spatial separation between the end points of the two atomic trajectories was determined (see, e.g., Figure 7.1). The interference between two plane waves with this separation and for which $\lambda_{\mathrm{dB}} = h/p_0 = 50$ pm, where $p_0 = |\vec{p_0}|$, was then obtained. The resulting Rydberg-atom interference patterns in Figure 7.8(b), which were calculated for the values of T_{grad} in Figure 7.8(a), exhibit interference fringes with the same periodicity as those in the experimental data. However, to achieve the good quantitative agreement with the results of the experiments seen in this figure it was necessary to incorporate into the calculations contributions from decoherence and population loss from the circular states. Both

of these effects were assumed to depended exponentially on the value of $|V_{\text{grad}}|$ resulting in interference patterns with intensity

$$I(V_{\text{grad}}) = A\left[I_0(V_{\text{grad}}) - 0.5\right]\exp\left[-\frac{|V_{\text{grad}}|}{C_{\text{decoh.}}}\right] + \exp\left[-\frac{|V_{\text{grad}}|}{C_{\text{loss}}}\right] + B, \qquad (7.2)$$

where $I_0(V_{\text{grad}})$ is the normalised intensity of the interference pattern dependent on the value of $|V_{\text{grad}}|$, excluding effects of dephasing, decoherence or circular state depopulation, and $A = 0.8$ and $B = -0.4$ are constants that were determined empirically. The decay constant, $C_{\text{decoh.}}$, associated with decoherence of the superposition states, which caused the reduction in the contrast of the interference fringes, was found to be 1.2 V. The decay constant, C_{loss}, associated with the loss in the total detected signal from the circular Rydberg states, which caused the reduction in the normalised signals in Figure 7.8(a), was found to be 4.2 V. The decoherence inferred from the results of these calculations is attributed to a combination of the finite longitudinal coherence length of the momentum distribution in the atomic beam, effects of electric field noise on the Rydberg states that increase when they are more strongly polarised, and imperfections in the relative amplitudes of the pairs of electric field gradient pulses. The elucidation of the mechanism that caused the loss in the total signal detected as the value of $|V_{\text{grad}}|$ was increased required the performance of additional experiments. However, from the results of the calculations in Figure 7.8(b) it was determined that, e.g., when $|V_{\text{grad}}| = 1.3$ V for $T_{\text{grad}} = 525$ ns and the second interference maximum is observed, the difference in the forces exerted on the two matter-wave components in the pulsed field gradients was 1.4×10^{-24} N. This corresponds to a difference in acceleration of 220 $\text{m} \cdot \text{s}^{-2}$ and a displacement of the centres-of-mass of the matter-waves at the time of the second $\pi/2$ pulse of 100 pm (see also Figure 7.1).

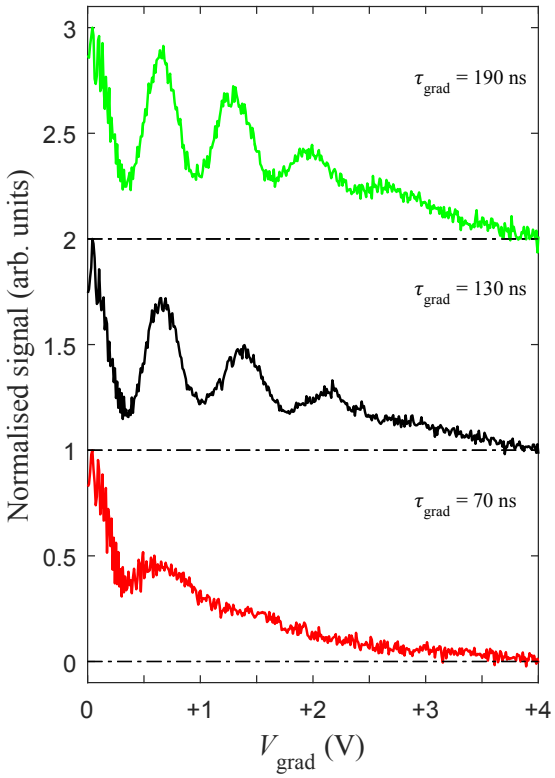

Figure 7.9: Rydberg-atom interference patterns recorded for $T_{\text{grad}} = 525$ ns and values of τ_{grad} of 70, 130 and 190 ns, as indicated. For clarity only the parts of each interference pattern for which $V_{\text{grad}} \geq 0$ are displayed. The data recorded for $\tau_{\text{grad}} = 130$ ns correspond to that in Figure 7.8(a) for $T_{\text{grad}} = 525$ ns. Note the upper datasets in this figure are vertically offset for clarity.

7.7 Further experimental tests

To identify the origin of the loss of signal at high values of $|V_{\text{grad}}|$ in Figure 7.8, further measurements were performed for $T_{\text{grad}} = 525$ ns and a range of values of τ_{grad}. Data recorded for $\tau_{\text{grad}} = 70$, 130 and 190 ns are displayed in Figure 7.9. For clarity, only results for $V_{\text{grad}} \geq 0$ are included in this figure. From these measurements it can be seen that the greatest contrast in the interference patterns, and the greatest number of interference fringes, are observed for the slowest rise and fall times of the electric field gradient pulses, i.e., for $\tau_{\text{grad}} = 190$ ns. The data recorded for $\tau_{\text{grad}} = 130$ ns, which corresponds to that in Figure 7.8(a) for $T_{\text{grad}} = 525$ ns, exhibits very similar characteristics with only slightly more significant decoherence and loss in total signal at larger values of V_{grad}. However, for the shortest rise time of $\tau_{\text{grad}} = 70$ ns the situation is quite different. Not only is decoherence more apparent, but the total population also decays faster than it does in the measurements performed with slower rise times. Because of this more significant loss in total population from the two circular states for short rise and fall times, it is concluded that this contribution to the measurements arises from the non-adiabatic evolution of the Rydberg states under these conditions. These non-adiabatic dynamics transfer population out of the $|55c\rangle$ and $|56c\rangle$ states and into neighbouring lower m_ℓ states as the pulsed fields are more rapidly switched from and to zero.

To confirm the attribution of the oscillations in the data in Figure 7.8 to effects of matter-wave interference, and that they are not a consequence of resonances or fluctuations introduced by the pulsed electric fields, several further tests were performed. The results of these are displayed in Figure 7.10. For all of the measurements in this figure $T_{\text{grad}} = 525$ ns and $\tau_{\text{grad}} = 130$ ns. The data in Figure 7.10(a) represent a reference measurement which corresponds to that in Figure 7.8(a) for $T_{\text{grad}} = 525$ ns. To check that the oscillations in the ratio of the circular state populations upon application of the complete interferometry sequence of microwave

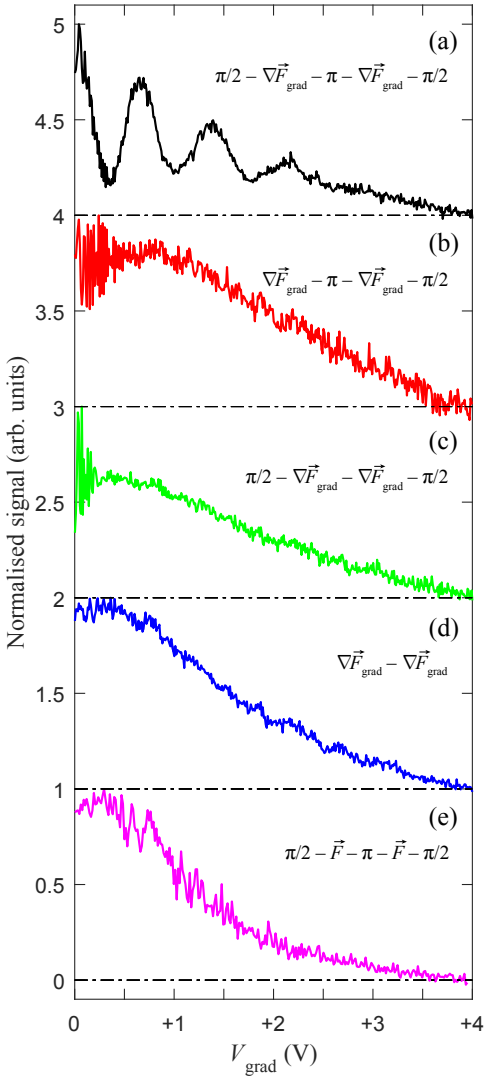

Figure 7.10: Measurements performed to validate the interpretation of the Rydberg-atom interference patterns. (a) Reference measurement performed with the complete Rydberg-atom interferometry pulse sequence, $T_{\mathrm{grad}} = 525$ and $\tau_{\mathrm{grad}} = 130$ ns, as in Figure 7.8(a) for $T_{\mathrm{grad}} = 525$ ns. Interferometry sequences with (b) the first $\pi/2$ microwave pulse, (c) the π pulse, and (d) all microwave pulses omitted. (e) Measurement performed with electrodes E1 and E2 oriented parallel to each other. The electric potentials on the horizontal axis in (e) have been scaled by 1.46 so that the corresponding electric fields are approximately comparable to those at the position of the atoms in datasets (a) to (d) (see text for details).

and electric field gradient pulses relied on the preparation and coherent manipulation of the superpositions of Rydberg states, the data in Figure 7.10(b), (c) and (d) were recorded with the first $\pi/2$, the π and all three microwave pulses omitted, respectively. No oscillations are seen with the periodicity of those observed in Figure 7.10(a) in any of these data sets. The data in Figure 7.10(d), in which no microwave pulses were applied and the normalised signal gradually reduces as $|V_{\mathrm{grad}}|$ is increased, confirms that the loss in the circular state populations for larger values of $|V_{\mathrm{grad}}|$ is a result of non-adiabatic internal Rydberg-state dynamics and is not caused by decoherence of the superposition of momentum states.

As a final test, Figure 7.10(e) shows the result of a measurement carried out with an identical sequence of microwave and electric potential pulses to that in Figure 7.10(a) but with the configuration of electrodes E1 and E2 adjusted so that they were parallel to each other with a separation in the x dimension of 13 mm. To account for the different electric fields which the atoms experience in this electrode configuration for each value of $|V_{\mathrm{grad}}|$, when compared to that in the wedge configuration, and to allow for a more direct comparison with the data in panels (a) to (d), the potentials on the horizontal axis in Figure 7.10(e) have been scaled by 1.46. In this situation the applied pulsed electric potentials did not give rise to significant electric field gradients at the position of the atoms and therefore no forces were exerted on the atoms by these fields. No oscillations are observed in this data, further confirming that the oscillations in the data recorded when the complete interferometry pulse sequence was applied arise from matter-wave interference of spatially separated Rydberg-atom de Broglie waves.

7.8 Conclusion

In this chapter, a scheme for matter-wave interferometry with atoms or molecules in high Rydberg states has been realised experimentally. For the pairs of Rydberg

states employed in the experiments, with induced electric dipole moments of up to 11 320 D and 11 740 D, and hence differences in their electric dipole moments of up to 420 D, the difference in the forces exerted on the matter-wave components by the electric field gradients to which they were subjected were on the order of 10^{-24} N. The corresponding relative accelerations were $\sim$ 100 m·s^{-2}. The typical displacements observed between the pairs of matter-wave components at the end of the interferometry sequences were up to 150 pm while the size of the atoms, given by $2\langle r \rangle$, where $\langle r \rangle$ is the expectation value the radial position operator acting on the Rydberg electron wavefunction, was 320 nm. From the range of experimental tests reported it is concluded that the maximal number of Rydberg-atom interference fringes observed was limited by the requirements for the adiabatic evolution of the Rydberg states in the combined electric and magnetic fields in which the experiments were performed. A larger number of interference fringes are expected to be seen if, for low values of V_{grad}, a longer period of free flight is included between the pairs of electric field gradient pulses, or if lower-ℓ Rydberg states, for which the criteria for adiabatic evolution in the pulsed electric fields can be less restrictive, are employed. Indeed, follow-up experiments performed using superpositions of 56s and 57s Rydberg states have allowed up to 14 fringes, and hence matter-wave displacements of up to 0.7 nm to be observed [84]. In these experiments the number of observable fringes is now limited by the longitudinal velocity spread of the bunches of excited Rydberg atoms prepared. This velocity spread could be improved by using a shorter electric field excitation pulse or by allowing for a longer flight time before excitation to increase velocity dispersion.

The Rydberg-atom interferometry scheme presented here relies on the generation of an inhomogeneous electric field with a constant gradient in the direction of propagation of the atomic beam. If this gradient is accurately known, from the precise geometry of the electrode configuration, this type of interferometer represents

a tool for measuring matter-wave de Broglie wavelengths, and hence momenta. From this perspective, if forces are exerted on the atoms in the direction perpendicular to the surface of the Earth, it is expected that Rydberg-atom interferometry of the kind described here may be used to measure changes in de Broglie wavelength caused by the acceleration of samples in Rydberg states in the gravitational field of the Earth. Such measurements are of interest at present for systems composed of antimatter, e.g., antihydrogen – which is synthesised in high Rydberg states – or Ps – which in its ground state is too short lived (142 ns) to permit such measurements but when excited to Rydberg states exhibits significantly longer lifetimes (> 10 μs) limited by spontaneous emission to the ground state.

In addition to measurements of antimatter gravity, the large size (320 nm) of the Rydberg atoms used in the experiments reported here makes the methodology and results presented of interest for studies of effects of matter-wave interference in macroscopic quantum systems. In this context, future experiments directed towards investigations of the decoherence of the superpositions of Rydberg-atom momentum states with large spatial separations are of interest.

Chapter 8

Conclusion and outlook

In this thesis two different methods of using inhomogeneous electric fields to split beams of He atoms in high Rydberg states have been presented. The first used a two-dimensional chip-based electrode structure to incoherently split an atomic beam into two macroscopically-separated components with separations on the order of 1 cm. These experiments motivated further studies of the mechanisms of Rydberg-state depolarisation caused by radio-frequency electric fields. The second approach to splitting Rydberg-atom beams used a series of microwave and electric field pulses to coherently separate samples of atoms in superpositions of circular Rydberg states. This work resulted in the first demonstration of electric matter-wave interferometry for atoms in Rydberg states.

In these experiments, Rydberg states with values of n between 52 and 56 were prepared using a two-colour, two-photon laser photoexcitation scheme. In the rf-depolarisation experiments, an additional microwave transition was included to maximise the spectral resolution for the final state preparation. In the interferometry experiments, the crossed fields method, with a static background magnetic field and time-varying perpendicular electric fields, was used to prepare circular Rydberg states. Microwave spectroscopy of transitions between Rydberg states was

performed to utilise the atoms as microscopic antennae to calibrate both a.c. and d.c. electric field strengths. Two different detection schemes were employed, both based on pulsed electric field ionisation of the excited Rydberg atoms. This allowed either position-sensitive or state-selective detection of the atoms.

The beam splitter described in Chapter 4 was designed to be integrated with the types of Rydberg-atom trap and microwave circuit architectures used in hybrid circuit QED. In this context, it is foreseen to use this type of beam splitter to distribute samples of cold atoms in Rydberg states to spatially-separated interaction regions. In experiments with cold Rydberg molecules it could be utilised for low-energy collision studies to allow reference intensity measurements in each experiment cycle. This type of chip-based beam splitter also represents a valuable addition to the tools for performing Rydberg-atom optics experiments. In general, in experiments of this type, which use electric fields to control the motion of samples of atoms or molecules in Rydberg states, the work presented in Chapter 5 has highlighted the necessity of minimising electric field noise and carefully controlling any resonant frequency modulations of the applied electric fields to maintain maximum quantum-state purity and minimise depolarisation and population losses.

The extremely small de Broglie wavelengths of massive particles, such as He atoms, make them particularly sensitive to small forces exerted on them from their surrounding environment. Combined with an interferometry scheme of the type presented in Chapters 6 and 7, this feature could be exploited to develop high-sensitivity sensors based on Rydberg-atom interferometry. With the appropriate choice of superposition states this could allow the realisation of new types of atomic electrometers. Sensors based on matter-wave interference may also be of use in tests of antimatter gravity and the weak equivalence principle. Current candidates for experiments of these types are antihydrogen and Ps atoms, although the application of existing techniques for precise gravimetry with these species suffer from several

limitations. Currently, the number of antihydrogen atoms produced in typical experiments and the inability to laser-cool them quickly and efficiently prohibit the use of traditional free-fall and interferometry measurement techniques. In the case of Ps, the short ground-state annihilation lifetime of 140 ns imposes stringent limitations on its use in interferometry experiments. However, the lifetimes of Ps atoms can be greatly enhanced by exciting them to Rydberg states. In these states annihilation is suppressed and the atoms decay by spontaneous emission before annihilation occurs. The florescence lifetime of Rydberg states with $n = 20$ in Ps, for example, has been measured to be 40 μs [15]. In addition, the methods of Rydberg-Stark deceleration have recently been applied to guide and velocity select Ps atoms in Rydberg states. These developments suggest that Ps is an ideal candidate for tests of antimatter gravity using the Rydberg-atom interferometry scheme presented in this thesis.

A gravity measurement with Ps using the Rydberg-atom interferometry scheme described here would rely on the fact that this scheme can act as a way to measure the de Broglie wavelength, and therefore momenta, of the atoms in the direction that the forces are applied. If these forces are oriented in the direction of the gravitational field of Earth, accelerations caused by this field could be measured in a free-fall type of experiment but over a much smaller free-fall distance than a classical measurement. The advantage of an experiment of this type over other free-fall experiments is the increased sensitivity that it offers. An imaging MCP has an approximate resolution of 10 μm. It would require 1.4 ms under free fall for Ps to be displaced by that amount by a force equal to g, however, during this time the Ps atoms, travelling at 10^5 m$\cdot$s^{-1}, would cover a distance of 140 m. The scale of such an experiment makes it unfeasible, especially considering that the atoms would be extremely sensitive to stray electric fields during their flight. Using the interferometry scheme presented here it is expected that a measurement of g for Ps

to a precision of 10% would be possible with measurement times of < 100 μs and for matter-wave displacements of < 100 nm.

By combining improvements in the production of slow Ps beams with refinements in the Rydberg-atom interferometry techniques it is foreseen that measurements with this precision could be carried out within flight distances of $\lessapprox 1$ m. The route to carrying out such an experiment is likely to require modifications to the current scheme to circumvent losses arising from non-adiabatic internal state dynamics. The scheme will then need to be extended to realise a closed loop 'Mach-Zehnder' type interferometer. Current progress in the laboratory suggests that these steps are achievable with the current approach to the experiment.

Bibliography

[1] J. R. Rydberg. Über den Bau der Linienspektren der chemischen Grundstoffe. *Zeitschrift für Phys. Chemie*, 5U:227–232, 1890.

[2] S. D. Hogan. Rydberg-Stark deceleration of atoms and molecules. *EPJ Tech. Instrum.*, 3:2, 2016.

[3] E. Urban, T. A. Johnson, T. Henage, L. Isenhower, D. D. Yavuz, T. G. Walker, and M. Saffman. Observation of Rydberg blockade between two atoms. *Nat. Phys.*, 5:110–114, 2009.

[4] A. Gaëtan, Y. Miroshnychenko, T. Wilk, A. Chotia, M. Viteau, D. Comparat, P. Pillet, A. Browaeys, and P. Grangier. Observation of collective excitation of two individual atoms in the Rydberg blockade regime. *Nat. Phys.*, 5:115–118, 2009.

[5] H. Bernien, S. Schwartz, A. Keesling, H. Levine, A. Omran, H. Pichler, S. Choi, A. S. Zibrov, M. Endres, M. Greiner, V. Vuletić, and M. D. Lukin. Probing many-body dynamics on a 51-atom quantum simulator. *Nature*, 551:579–584, 2017.

[6] S. Gleyzes, S. Kuhr, C. Guerlin, J. Bernu, S. Deléglise, B. Hoff, H. Ulrich, M. Brune, J. Raimond, and S. Haroche. Quantum jumps of light recording the birth and death of a photon in a cavity. *Nature*, 446:297–300, 2007.

[7] P. Rabl, D. DeMille, J. M. Doyle, M. D. Lukin, R. J. Schoelkopf, and P. Zoller. Hybrid quantum processors: molecular ensembles as quantum memory for solid state circuits. *Phys. Rev. Lett.*, 97:033003, 2006.

[8] S. D. Hogan, J. A. Agner, F. Merkt, T. Thiele, S. Filipp, and A. Wallraff. Driving Rydberg-Rydberg transitions from a coplanar microwave waveguide. *Phys. Rev. Lett.*, 108:063004, 2012.

[9] A. Osterwalder and F. Merkt. Using high Rydberg states as electric field sensors. *Phys. Rev. Lett.*, 82:1831–1834, 1999.

[10] D. A. Anderson, S. A. Miller, G. Raithel, J. A. Gordon, M. L. Butler, and C. L. Holloway. Optical measurements of strong microwave fields with Rydberg atoms in a vapor cell. *Phys. Rev. Appl.*, 5:034003, 2016.

[11] E. K. Dietsche, A. Larrouy, S. Haroche, J. M. Raimond, M. Brune, and S. Gleyzes. High-sensitivity magnetometry with a single atom in a superposition of two circular Rydberg states. *Nat. Phys.*, 15:326–329, 2019.

[12] T. Chalopin, C. Bouazza, A. Evrard, V. Makhalov, D. Dreon, J. Dalibard, L. A. Sidorenkov, and S. Nascimbene. Quantum-enhanced sensing using non-classical spin states of a highly magnetic atom. *Nat. Commun.*, 9:4955, 2018.

[13] J. Liu, E. J. Salumbides, U. Hollenstein, J. C. J. Koelemeij, K. S. E. Eikema, W. Ubachs, and F. Merkt. Determination of the ionization and dissociation energies of the hydrogen molecule. *J. Chem. Phys.*, 130:174306, 2009.

[14] R. Pohl, A. Antognini, F. Nez, F. D. Amaro, F. Biraben, J. M. R. Cardoso, D. S. Covita, A. Dax, S. Dhawan, L. M. P. Fernandes, A. Giesen, T. Graf, T. W. Hänsch, P. Indelicato, L. Julien, C. Kao, P. Knowles, E. Le Bigot, Y. Liu, J. A. M. Lopes, L. Ludhova, C. M. B. Monteiro, F. Mulhauser, T. Nebel, P. Rabinowitz, J. M. F.

dos Santos, L. A. Schaller, K. Schuhmann, C Schwob, D. Taqqu, J. F. C. A. Veloso, and F. Kottmann. The size of the proton. *Nature*, 466:213–216, 2010.

[15] A. Deller, A. M. Alonso, B. S. Cooper, S. D. Hogan, and D. B. Cassidy. Measurement of Rydberg positronium fluorescence lifetimes. *Phys. Rev. A*, 93:062513, 2016.

[16] A. E. Charman. Description and first application of a new technique to measure the gravitational mass of antihydrogen. *Nat. Commun.*, 4:1785, 2013.

[17] D. Townsend, A. L. Goodgame, S. R. Procter, S. R. Mackenzie, and T. P. Softley. Deflection of krypton Rydberg atoms in the field of an electric dipole. *J. Phys. B At. Mol. Opt. Phys.*, 34:439–450, 2001.

[18] W. Gerlach and O. Stern. Der experimentelle Nachweis des magnetischen Moments des Silberatoms. *Zeitschrift für Phys.*, 8:110–111, 1922.

[19] S. R. Procter, Y. Yamakita, F. Merkt, and T. P. Softley. Controlling the motion of hydrogen molecules. *Chem. Phys. Lett.*, 2003.

[20] Y. Yamakita, S. R. Procter, A. L. Goodgame, T. P. Softley, and F. Merkt. Deflection and deceleration of hydrogen Rydberg molecules in inhomogeneous electric fields. *J. Chem. Phys.*, 121:1419–1431, 2004.

[21] E. Vliegen, P. A. Limacher, and F. Merkt. Measurement of the three-dimensional velocity distribution of Stark-decelerated Rydberg atoms. *Eur. Phys. J. D*, 40:73–80, 2006.

[22] E. Vliegen and F. Merkt. Normal-incidence electrostatic Rydberg atom mirror. *Phys. Rev. Lett.*, 97:033002, 2006.

[23] S. D. Hogan and F. Merkt. Demonstration of three-dimensional electrostatic trapping of state-selected Rydberg atoms. *Phys. Rev. Lett.*, 100:043001, 2008.

[24] Ch. Seiler, S. D. Hogan, H. Schmutz, J. A. Agner, and F. Merkt. Collisional and radiative processes in adiabatic deceleration, deflection, and off-axis trapping of a Rydberg atom beam. *Phys. Rev. Lett.*, 106:073003, 2011.

[25] S. A. Meek, H. Conrad, and G. Meijer. A Stark decelerator on a chip. *New J. Phys.*, 11:055024, 2009.

[26] P. Allmendinger, J. Deiglmayr, J. A. Agner, H. Schmutz, and F. Merkt. Surface-electrode decelerator and deflector for Rydberg atoms and molecules. *Phys. Rev. A*, 90:043403, 2014.

[27] P. Lancuba and S. D. Hogan. Guiding Rydberg atoms above surface-based transmission lines. *Phys. Rev. A*, 88:043427, 2013.

[28] P. Lancuba and S. D. Hogan. Transmission-line decelerators for atoms in high Rydberg states. *Phys. Rev. A*, 90:053420, 2014.

[29] P. Lancuba and S. D. Hogan. Electrostatic trapping and in situ detection of Rydberg atoms above chip-based transmission lines. *J. Phys. B At. Mol. Opt. Phys.*, 49:074006, 2016.

[30] S. D. S. Gordon and A. Osterwalder. 3D-printed beam splitter for polar neutral molecules. *Phys. Rev. Appl.*, 7:044022, 2017.

[31] J. Hammer, S. Thomas, P. Weber, and P. Hommelhoff. Microwave chip-based beam splitter for low-energy guided electrons. *Phys. Rev. Lett.*, 114:254801, 2015.

[32] L. Deng, Y. Liang, Z. Gu, S. Hou, S. Li, Y. Xia, and J. Yin. Experimental demonstration of a controllable electrostatic molecular beam Splitter. *Phys. Rev. Lett.*, 106:140401, 2011.

[33] P. Lancuba. Rydberg-Stark deceleration and trapping of helium atoms above electrical transmission-lines. *PhD Thesis, UCL (University College London)*, 2016.

[34] S. S. Hodgman, R. G. Dall, L. J. Byron, K. G. H. Baldwin, S. J. Buckman, and A. G. Truscott. Metastable helium: a new determination of the longest atomic excited-state Lifetime. *Phys. Rev. Lett.*, 103:053002, 2009.

[35] R. G. Hulet and D. Kleppner. Rydberg atoms in "circular" states. *Phys. Rev. Lett.*, 51:1430–1433, 1983.

[36] V. Zhelyazkova and S. D. Hogan. Preparation of circular Rydberg states in helium using the crossed-fields method. *Phys. Rev. A*, 94:023415, 2016.

[37] S. D. Hogan. Cold atoms and molecules by Zeeman deceleration and Rydberg-Stark deceleration. *Habilitation Thesis, ETH Zurich*, 2012.

[38] R. J. Damburg and V. V. Kolosov. *Theoretical studies of hydrogen Rydberg atoms in electric fields*. 1983.

[39] T. F. Gallagher. *Rydberg Atoms*. Cambridge University Press, Cambridge, 1994.

[40] Ch. Seiler, S. D. Hogan, and F. Merkt. Dynamical processes in Rydberg-Stark deceleration and trapping of atoms and molecules. *Chimia*, 66:208–211, 2012.

[41] Ch. Seiler, J. A. Agner, P. Pillet, and F. Merkt. Radiative and collisional processes in translationally cold samples of hydrogen Rydberg atoms studied in an electrostatic trap. *J. Phys. B At. Mol. Opt. Phys.*, 49:094006, 2016.

[42] S. D. Hogan, Ch. Seiler, and F. Merkt. Rydberg-state-enabled deceleration and trapping of cold molecules. *Phys. Rev. Lett.*, 103:123001, 2009.

[43] Ch. Seiler, S. D. Hogan, and F. Merkt. Trapping cold molecular hydrogen. *Phys. Chem. Chem. Phys.*, 13:19000, 2011.

[44] P. Allmendinger, J. Deiglmayr, K. Höveler, O. Schullian, and F. Merkt. Observation of enhanced rate coefficients in the $H_2^+ + H_2 \rightarrow H_3^+ + H$ reaction at low collision energies. *J. Chem. Phys.*, 145:244316, 2016.

[45] P. Allmendinger, J. Deiglmayr, O. Schullian, K. Höveler, J. A. Agner, H. Schmutz, and F. Merkt. New method to study ion-molecule reactions at low temperatures and application to the $H_2^+ + H_2 \rightarrow H_3^+ + H$ reaction. *ChemPhysChem*, 17:3596–3608, 2016.

[46] K. Gawlas and S.D. Hogan. Rydberg-state-resolved resonant energy transfer in cold electric-field-controlled intrabeam collisions of NH_3 with Rydberg He atoms. *J. Phys. Chem. Lett.*, 11:83–87, 2020.

[47] S. D. Hogan, P. Allmendinger, H. Saßmannshausen, H. Schmutz, and F. Merkt. Surface-electrode Rydberg-Stark decelerator. *Phys. Rev. Lett.*, 108:063008, 2012.

[48] D. B. Cassidy and S. D. Hogan. Atom control and gravity measurements using Rydberg positronium. *Int. J. Mod. Phys. Conf. Ser.*, 30, 2014.

[49] A. Kellerbauer, M. Amoretti, A. S. Belov, G. Bonomi, I. Boscolo, R. S. Brusa, M. Büchner, V. M. Byakov, L. Cabaret, C. Canali, C. Carraro, F. Castelli, S. Cialdi, M. de Combarieu, D. Comparat, G. Consolati, N. Djourelov, M. Doser, G. Drobychev, A. Dupasquier, G. Ferrari, P. Forget, L. Formaro, A. Gervasini, M. G. Giammarchi, S. N. Gninenko, G. Gribakin, S. D. Hogan, M. Jacquey, V. Lagomarsino, G. Manuzio, S. Mariazzi, V. A. Matveev, J. O. Meier, F. Merkt, P. Nedelec, M. K. Oberthaler, P. Pari, M. Prevedelli, F. Quasso, A. Rotondi, D. Sillou, S. V. Stepanov, H. H. Stroke, G. Testera, G. M. Tino, G. Trénec, A. Vairo, J. Vigué, H. Walters, U. Warring, S. Zavatarelli, and D. S. Zvezhinskij. Proposed antimatter gravity measurement with an antihydrogen beam. *Nucl. Instruments Methods Phys. Res. Sect. B Beam Interact. with Mater. Atoms*, 266:351–356, 2008.

[50] V. Zhelyazkova and S. D. Hogan. Rydberg-Stark states in oscillating electric fields. *Mol. Phys.*, 113:3979–3991, 2015.

[51] V. Zhelyazkova and S. D. Hogan. Probing interactions between Rydberg atoms with large electric dipole moments in amplitude-modulated electric fields. *Phys. Rev. A*, 92:011402, 2015.

[52] J. Palmer and S. D. Hogan. Experimental demonstration of a Rydberg-atom beam splitter. *Phys. Rev. A*, 95:053413, 2017.

[53] G. Higgins, W. Li, F. Pokorny, C. Zhang, F. Kress, C. Maier, J. Haag, Q. Bodart, I. Lesanovsky, and M. Hennrich. Single strontium Rydberg ion confined in a Paul trap. *Phys. Rev. X*, 7:021038, 2017.

[54] A. Deller and S. D. Hogan. Confinement of high- and low-field-seeking Rydberg atoms using time-varying inhomogeneous electric fields. *Phys. Rev. Lett.*, 122:053203, 2019.

[55] O. Carnal and J. Mlynek. Young's double-slit experiment with atoms: A simple atom interferometer. *Phys. Rev. Lett.*, 66:2689–2692, 1991.

[56] D. W. Keith, C. R. Ekstrom, Q. A. Turchette, and D. E. Pritchard. An interferometer for atoms. *Phys. Rev. Lett.*, 66:2693–2696, 1991.

[57] F. Riehle, T. Kisters, A. Witte, J. Helmcke, and Ch. J. Bordé. Optical Ramsey spectroscopy in a rotating frame: Sagnac effect in a matter-wave interferometer. *Phys. Rev. Lett.*, 67:177–180, 1991.

[58] Ch. J. Bordé. Atomic interferometry with internal state labelling. *Phys. Lett. A*, 140:10–12, 1989.

[59] M. Kasevich and S. Chu. Atomic interferometry using stimulated Raman transitions. *Phys. Rev. Lett.*, 67:181–184, 1991.

[60] A. Peters, K. Y. Chung, and S. Chu. High-precision gravity measurements using atom interferometry. *Metrologia*, 38:25–61, 2001.

[61] E. M. Rasel, M. K. Oberthaler, H. Batelaan, J. Schmiedmayer, and A. Zeilinger. Atom wave interferometry with diffraction gratings of light. *Phys. Rev. Lett.*, 75:2633–2637, 1995.

[62] C. Fabre, M. Gross, J. M. Raimond, and S. Haroche. Measuring atomic dimensions by transmission of Rydberg atoms through micrometre size slits. *J. Phys. B At. Mol. Phys.*, 16:L671–L677, 1983.

[63] S. Nic Chormaic, V. Wiedemann, Ch. Miniatura, J. Robert, S. Le. Boiteux, V. Lorent, O. Gorceix, S. Feron, J. Reinhardt, and J. Baudon. Longitudinal Stern-Gerlach atomic interferometry using velocity selected atomic beams. *J. Phys. D. Appl. Phys.*, 26:1271–1279, 1993.

[64] A. D. Cronin, J. Schmiedmayer, and D. E. Pritchard. Optics and interferometry with atoms and molecules. *Rev. Mod. Phys.*, 81:1051–1129, 2009.

[65] K. Hornberger, S. Gerlich, P. Haslinger, S. Nimmrichter, and M. Arndt. Colloquium : Quantum interference of clusters and molecules. *Rev. Mod. Phys.*, 84:157–173, 2012.

[66] D. Bohm. *Quantum Theory*. Prentice-Hall, New York, 1951.

[67] E. P. Wigner. The problem of measurement. *Am. J. Phys.*, 31:6–15, 1963.

[68] J. Schwinger, M. O. Scully, and B. G. Englert. Is spin coherence like Humpty-Dumpty? *Zeitschrift für Phys. D Atoms, Mol. Clust.*, 10:135–144, 1988.

[69] Y. L. Sokolov. Influence of Lamb shift on the interference of excited states of hydrogen atoms. *JETP Lett.*, 11, 1970.

[70] Y. L. Sokolov. Interference of the $2p_{1/2}$ state of the hydrogen atom. *Sov. Phys. JETP*, 36, 1973.

[71] Ch. Miniatura, F. Perales, G. Vassilev, J. Reinhardt, J. Robert, and J. Baudon. A longitudinal Stern-Gerlach interferometer : the "beaded" atom. *J. Phys. II*, 1:425–436, 1991.

[72] Ch. Miniatura, J. Robert, O. Gorceix, V. Lorent, S. Le Boiteux, J. Reinhardt, and J. Baudon. Atomic interferences and the topological phase. *Phys. Rev. Lett.*, 69:261–264, 1992.

[73] S. Machluf, Y. Japha, and R. Folman. Coherent Stern-Gerlach momentum splitting on an atom chip. *Nat. Commun.*, 4:2424, 2013.

[74] O. Amit, Y. Margalit, O. Dobkowski, Z. Zhou, Y. Japha, M. Zimmermann, M. A. Efremov, F. A. Narducci, E. M. Rasel, W. P. Schleich, and R. Folman. T^3 Stern-Gerlach matter-wave interferometer. *Phys. Rev. Lett.*, 123:083601, 2019.

[75] A. Bassi, K. Lochan, S. Satin, T. P. Singh, and H. Ulbricht. Models of wave-function collapse, underlying theories, and experimental tests. *Rev. Mod. Phys.*, 85:471–527, 2013.

[76] X. He and B. H. J. McKellar. Topological phase due to electric dipole moment and magnetic monopole interaction. *Phys. Rev. A*, 47:3424–3425, 1993.

[77] M. Wilkens. Quantum phase of a moving dipole. *Phys. Rev. Lett.*, 72:5–8, 1994.

[78] J. P. Dowling, C. P. Williams, and J. D. Franson. Maxwell duality, Lorentz invariance, and topological phase. *Phys. Rev. Lett.*, 83:2486–2489, 1999.

[79] A. P. Mills and M. Leventhal. Can we measure the gravitational free fall of cold Rydberg state positronium? *Nucl. Instruments Methods Phys. Res. Sect. B Beam Interact. with Mater. Atoms*, 192:102–106, 2002.

[80] D. Delande and J. C. Gay. A new method for producing circular Rydberg states. *Europhys. Lett.*, 5:303–308, 1988.

[81] S. D. Hogan, Y. Houston, and B. Wei. Laser photoexcitation of Rydberg states in helium with n > 400. *J. Phys. B At. Mol. Opt. Phys.*, 51:145002, 2018.

[82] W. Pauli. Über das Wasserstoffspektrum vom Standpunkt der neuen Quantenmechanik. *Zeitschrift für Phys.*, 36:336–363, 1926.

[83] R. J. Elliott, G. Droungas, and J. P. Connerade. Active cancellation of the motional Stark effect in the diamagnetic spectrum of Ba. *J. Phys. B At. Mol. Opt. Phys.*, 28:L537–L542, 1995.

[84] J. D. R. Tommey and S. D. Hogan. *Private communication*, 2019.